Department of Mathematics, University of Bergen

Simulation of injection-induced deformation for a stimulation experiment at the Grimsel underground laboratory

Master of Science Thesis in Applied and Computational Mathematics

Haakon Ludvig Langeland Ervik

October, 2020

Acknowledgements

This thesis concludes my year as a master's student. It has been a year with many ups and downs and staying motivated as we had to relocate home for some time this spring has been tough. Through it all, my two supervisors Inga Berre and Ivar Stefansson have continuously supported and encouraged me. My main supervisor, Inga Berre, has been an excellent source for guidance and inspiration. I would especially like to thank her for motivating me to embark on the journey of writing a thesis in the first place and for supporting my academic journey ever since. Also, her support for me as I have planned for my future academic career has been indispensable. I am also thankful to my co-supervisor Ivar Stefansson. His door has always been open for short or long discussions. His attention to detail has been invaluable when I have struggled to track down the bugs in my code or have tried to understand a difficult topic.

I would also like to thank Eirik Keilegavlen whose input and reflections have been greatly valued. I am also grateful to the remainder of the porous media group at the University of Bergen for their continued support and source for new ideas.

I am especially grateful to all my friends in the master student office. They have made my past year an unforgettable experience.

Finally, I would like to thank my family for their support and understanding when I have not come home for dinner on time. They have always cheered for me as I have juggled between working on the thesis and applying for graduate school.

Haakon Ludvig Langeland Ervik

Bergen, October 2020

Abstract

Numerical models have increasingly become important tools to complement planning, testing, and implementation of technologies and strategies for geothermal reservoir projects in basement and crystalline igneous rock. Access to cost-effective and high-capacity computational resources can give valuable insight into governing mechanisms of stimulation experiments in fractured porous rock, which are often prohibitively expensive or otherwise infeasible to perform repeatedly in-situ in sufficiently comparable initial conditions. These experiments aim to reactivate existing faults or fractures by shear dilation, increasing the fluid circulation. Shear dilation refers to the process of volumetric expansion of a fracture as its rough surfaces try to dislocate relative to each other as shear stresses act on the fracture. The reactivation process is characterized by coupled interactions between high-pressure injection and flow through the fracture network, and rock deformation due to hydromechanical stress transfer. Uncovering these connections can be challenging, even for mesoscale subsurface experiments with access to the rock volume through tunnels and boreholes. Physics-based modeling constrained by in-situ data has the potential to complement the analysis of experimental results.

This thesis investigates modeling of a mesoscale hydraulic shearing experiment at the Grimsel Test Site, Switzerland. The stimulation experiment targets one of five intersecting ductile or brittle-ductile shear zones in a low-permeable crystalline rock with a high-pressure injection scheme. We present the first simulations, constrained by in-situ data, that fully couple isothermal fluid flow and poroelastic rock deformation in the crystalline rock, with flow, deformation, and slip-induced dilation in the shear zones. A mixed-dimensional discrete fracture matrix model explicitly represents shear zones and shear zone intersections as lower-dimensional subdomains in the intact rock. Frictional contact mechanics is a non-linear process that governs slip on the shear zone surfaces. This results in a non-linear system of equations that cannot be solved with traditional Newton methods. Instead, a semi-smooth Newton method is applied to iteratively converge towards a solution.

The simulations captured transmissivity enhancement within one order of magnitude of observations. Additionally, slip-induced poroelastic effects were revealed. We also investigated the effects of intact rock permeability and shear zone size. A higher intact rock permeability led to greater leakage from the target shear zone into the intact rock compared to the case with a lower intact rock permeability, reducing the extent of the pressure front within the shear zone. In simulations with larger shear zones, there was a faster pressure decline in the target shear zone after shut-in due to more volume for fluid storage and a larger area for leakage into the intact rock, while smaller shear zones preserved a higher pressure for considerably longer time. The results show the applicability of numerical models to complement in-situ stimulation experiments. Finally, we comment on extensions related to two-phase flow, gravitational effects, and anisotropic elastic parameters.

Contents

List of figures

List of tables

1 Background

The need for 24-hour energy generation is ever more pronounced as much of the world's societies evolve to enjoy the needs associated with heating, transport, communication, and lighting. This demand for energy has historically been met with extensive use of fossil fuels (Ritchie, 2014). The energy supply sector is comprised of extraction, conversion, storage, transmission, and distribution of energy, and was responsible for approximately 35% of total anthropogenic greenhouse gas (GHG) emissions in 2010. The sector's share of annual GHG emissions has accelerated since the 1990's due to the energy demand associated with rapid economic growth, with coal being a prominent source of energy (Bruckner et al., 2015).

The emissions of GHG have wide-ranging implications for earth, society, and the economy. Some of these adverse effects include sea-level rise, ocean acidification, more intense weather extremes such as droughts, worse air quality, and increased frequency and severity of allergic illness (Lall et al., 2018; Nolte et al., 2018). The severity of these events depends on the atmospheric response to heating effects associated with the GHG emissions. Commonly, the surface air global-mean temperature is used as a single-parameter indicator to the response of the cumulative GHG emissions. To limit the global mean warming relative to pre-industrial levels to less than $2\ ^\circ\mathrm{C}$ by the year 2100 with a probability of more than 70%, yearly $\mathrm{CO_2}$ emissions must be halved relative to 1990 emissions by 2050 (Meinshausen et al., 2009).

Geothermal energy has emerged as a potential pathway for a reliable baseload supply of electricity throughout the world and would substantially reduce the GHG emissions from the energy supply sector (Goldstein et al., 2011). However, much of the world's potential resources within $10\ \mathrm{km}$ of the Earth's surface is situated in hard, compact rock. Little, if any fluid can flow or filtrate through the rock. Instead, the fluid flows in fractures and faults that are formed over long timescales due to tectonic movement of the crust. Faults are fractures or zones of fractures that separate adjacent blocks of rock and allow fluid transmission due to irregularities and roughness in the void space between the blocks. Shearing along the fracture surfaces can increase the volume between the surfaces through the shear dilation mechanism. Shear dilation occurs as the adjacent fracture surfaces attempt to dislocate relative to each other under the action of shear stresses within the formation (Gao et al., 2019). If the rock is tough enough to withstand crushing and granulation of the asperities, the surface separation increases to relieve the applied shear stresses during dislocation of the surfaces. High pressure fluid injection into faults relieves the effective confining stresses and can result in shearing if the in-situ stress regime is sufficiently anisotropic.

Enhanced geothermal systems (EGS) exploit these processes to stimulate rock masses that have sufficient temperature gradients to extract geothermal energy, but insufficient initial flow conditions to allow for fluid circulation between injection and production boreholes. We typically quantify the transmission properties with the transmissivity, which is a measure of the rate at which a fluid can flow through a fault of a given thickness. Enhanced fluid transmission allows for sustained production of geothermal energy as the fluid circulates through larger regions of the hot rock mass. Numerous demonstrations of hydraulic shearing and EGS exist around the world (e.g. Ayling and Moore (2013); Cladouhos et al. (2016); Garcia et al. (2016); Gérard et al. (2006); Lu (2018); Teza et al. (2011)).

Hydraulic shearing is coupled with other physical processes including thermal (T), hydraulic (H), mechanical (M), seismic (S), and chemical (C) processes which together with the fractured structure of the rock mass, influence the stimulation process (Amann et al., 2018; Wang et al., 2018). A thorough understanding of the interplay between the processes is necessary to develop safe and efficient enhanced geothermal systems. Studies of subsets of these processes are useful to develop models for leading order coupled behavior. Thermo-hydro-mechanical (THM) models have been widely used to analyze and understand observed reservoir behavior (e.g. Blanco et al. (2014); Rutqvist and Oldenburg (2008); Urpi et al. (2017); Vallier et al. (2020)). However, the models are reliant on detailed field data to support their conclusions. Since this is often lacking, especially in reservoir-scale stimulation experiments where the rock mass is accessed through boreholes from the surface, interpretation may be limited. In contrast, laboratory-scale experiments have made important contributions to parameterizing numerical models (e.g. Bandis et al. (1983)), but by virtue of their scale, lack important information of, for example, fault-related dynamics. Underground research laboratories on the decameter scale has the potential to bridge this gap. Here, tunnels are excavated into unaltered fault zones, which allows for experiments to be conducted under relatively well-constrained conditions (Y. G. Guglielmi et al., 2015; Pfister & Nold, 1984).

The Grimsel Test Site (GTS) is an underground research laboratory supporting a wide range of research projects, including those related to geothermal research (Figure 1.1). The site is located in the Aar Massif in Switzerland and has multiple tunnels that were excavated in 1983. The tunnel system is situated 450 meters below the surface, hosted in relatively homogenous crystalline rock.

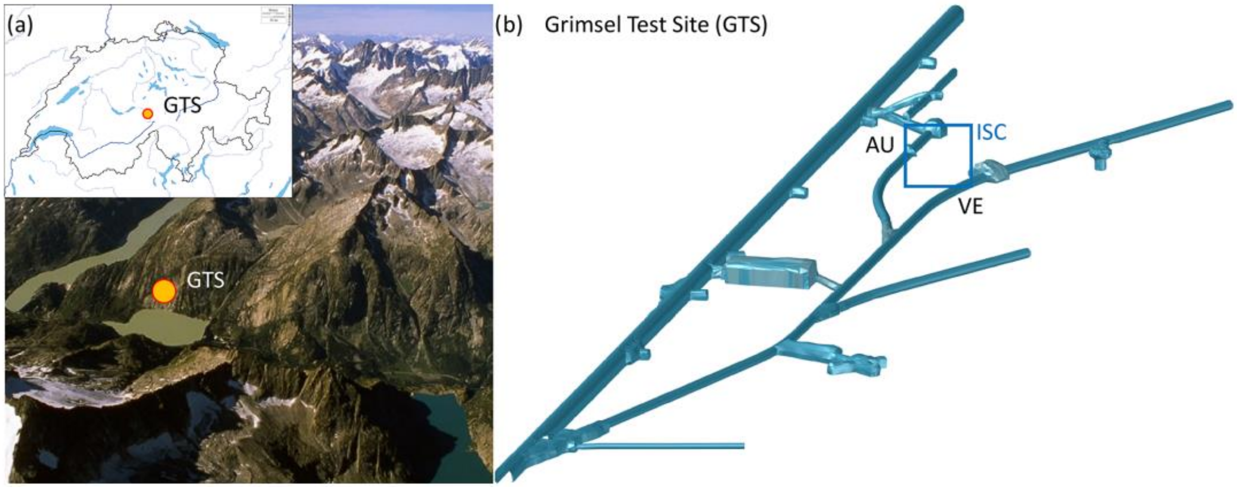

*Figure 1.1 **(a)** GTS is located in the Aar Massif in Switzerland. **(b)** The ISC experiment was conducted in crystalline rock, enclosed by AU and VE tunnels, in the southern part of the underground laboratory. Figure from Amann et al. (2018).*

The in-situ stimulation and circulation (ISC) experiment is a decameter scale experiment conducted in southern end of the Grimsel Test Site. The experiment is aimed at improving our understanding of both transmissivity enhancement due to hydraulic stimulation and the induced seismicity, as well as determining whether the stimulated region is a suitable analog to a heat exchanger. Two tunnels with diameters of 3.5 meters provide access to the volume, into which 15 boreholes have been drilled with instruments that allow characterization and monitoring of the rock volume before, during, and after the fluid injection experiments. The monitoring equipment enables detailed measurements of strain, temperature, seismicity, and fluid pressure (Amann et al., 2018; Krietsch et al., 2018a).

The rock volume contains localized regions of intense strain, denoted shear zones. The shear zones are grouped into two sets based on age and rock properties. Numerous brittle or gouge-filled fractures are present within the shear zones. As part of the ISC experiment, six hydraulic shearing experiments targeting the shear zones were conducted. One of these experiments targeted a ductile shear zone in the northern part of the domain. As a result of the stimulation of this shear zone, transmissivity near the injection interval increased by more than three orders of magnitude, hypothesized to be a result of $0.7 - 0.81\ \mathrm{mm}$ irreversible slip dislocation in the shear zone. Elevated pressure was observed mostly within the shear zone. The deformation response was characterized by a combination of fracture opening and slip within $15 - 20$ meters of the injection point and poroelastic effects due to the injected fluid further out from the injection point (Krietsch et al., 2020).

The characteristic poromechanical response of the rock mass following fluid injection makes it suitable for numerical modeling. We simulated the main stimulation cycle of a hydraulic shearing experiment and evaluated our model by comparing the simulated rock mass response to the observed response. To this end, we developed a geometric model of the shear zones and the surrounding rock mass. We modeled the intact rock as a poroelastic medium where fluid diffusion is fully coupled to mechanical deformation according to the Biot equations (Biot, 1941). The shear zones were modeled as planar fractures that can open, close, and slide as a result of the relative sizes of the hydromechanical stress in the intact rock and the fluid pressure in the fractures. A Coulomb type friction law was employed to model shear dislocation. Changes in fracture transmissivity were modeled with the cubic law, where slip is assumed to cause dilation, which increases transmissivity. The model is implemented in the PorePy framework using finite volume methods on two-dimensional and three-dimensional unstructured grids, where fractures are modeled as 2D planes in the 3D volume, and fracture intersections are represented by 1D lines (Keilegavlen et al., 2020).

The main contributions of this thesis are the numerical modeling of a hydraulic stimulation experiment at the Grimsel Test Site, including identification and setup of parameters, development and adjustments of the geometric model, integration to the PorePy framework, and evaluation and interpretation of the simulation results compared to the observations from the stimulation experiment. We studied the effects of perturbing model parameters that were expected to have a significant impact on the pressure distribution of the solution. The simulation code and run scripts for this thesis is available on https://github.com/haakon-e/mastersproject. Contributions to PorePy are outlined in Appendix 8.3.

The thesis is structured as follows:

We begin by describing the subsurface and some of its characteristic features in Chapter 2. Faults, shear zones, and fractures are fundamental structures for fluid conduction and slip in compact rock. We survey models that characterize their hydraulic structure. Then, we describe the hydraulic shear mechanism, which is critical in controlling transient changes of hydraulic properties in shear zones, faults, and fractures.

In Chapter 3, we survey conceptual models for fractured porous media. We focus on the mixed-dimensional discrete fracture matrix model, in which fractures are modeled as two-dimensional surfaces in the three-dimensional rock. Details on notation and projection operators for mixed-dimensional domains are summarized toward the end of the chapter.

Then, in Chapter 4, we present the set of partial differential equations that describe fluid flow, rock deformation, and fracture slip. These equations are coupled and non-linear.

In Chapter 5, we present the details on the discretization of the system of equations, including the structure of the global linear system, which is solved with a Newton-type method.

Chapter 6 is devoted to the stimulation experiment at the Grimsel Test Site. We provide details on the geological context and characterization studies of the rock mass. Then, we present the set of parameters and initial conditions used in the numerical simulation. We conclude the chapter by presenting and discussing the main findings.

Finally, in Chapter 7, we reflect on the findings in light of our model choices, and discuss limitations and extensions to the model.

2 Characteristics of fractured porous media

Subsurface rock is heterogeneous and deformable and can be studied across many scales. At the microscale, rock can be described as a solid material superimposed by a possibly saturated void space. The geometry and structural properties of the rock at this scale are important for understanding mesoscale processes. However, these details are too complex to be explicitly represented if the scale at which processes of interest occur is tens of meters or more. Fortunately, averaged descriptions of the rock mass can be introduced in which microscale properties and processes can be ignored in favor of macroscale properties and tendencies.

In this chapter, we describe the subsurface and its characteristic features that are of importance to experimentation and modeling of hydromechanically coupled processes. We seek idealized descriptions of the rock mass that are easy to understand conceptually and where relatively simple models for the rock mass response can be constructed. This is a useful exercise even as we know that the rock mass is a dynamically evolving structure that does not conform to any particular idealized model. Often, the lessons learnt in idealized settings can be helpful to understand the range of behavior we can expect to find in the heterogeneous rock within Earth's crust.

The compact, crystalline, and granitic rock mass at the Grimsel Test Site (GTS) can, like other rock masses, be divided into distinct structures. Most fundamentally is the intact rock which supports the overburden rock mass, is subject to elastic and plastic deformation, and is saturated by one or more fluid phases. In subsurface rock with sufficient anisotropy, stresses can concentrate in planar or curviplanar regions. The applied stresses deform the rock mass, and depending on the rock properties, the deformation can be characterized as either brittle or ductile (Figure 2.1). With sufficient differences between the maximum and minimum compressive stresses, the brittle rock breaks, forming fractures or faults (i.e. brittle shear zones) (Pine & Batchelor, 1984). Fractures and faults are discontinuous features of the rock mass that divides the rock into blocks of rock that supports relative displacement. Typically, these structures has significantly contrasting mechanical and hydraulic properties compared to the surrounding, intact rock.

Extended shear deformation of ductile rock masses in anisotropic stress regimes lead to zones of intense strain. These zones are denoted (ductile) shear zones. As with faults and fractures, the hydrogeological properties of shear zones can be remarkably dissimilar compared to the surrounding rock. In-between the end-member types, there are brittle-ductile shear zones that combine features of faulting in brittle rock and shearing in ductile rock. Figure 2.1 illustrates ductile, brittle, and brittle-ductile rock deformation.

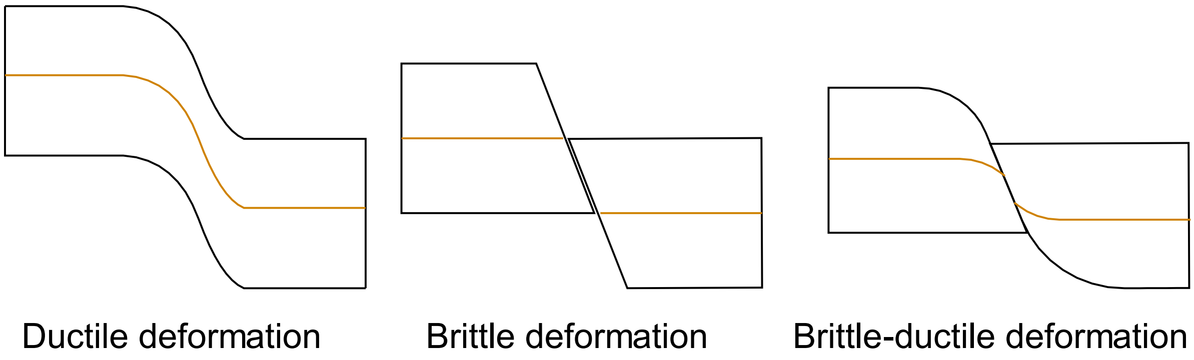

Figure 2.1 Schematic view of types of deformation response in rock.

The hydraulic shearing experiment that we simulated in this thesis, targeted a ductile shear zone. This chapter will survey the typical structure of fault zones, which turns out to be a suitable description of the ductile shear zones at GTS. We devote particular attention to the hydraulic structure of fault zones, and aspects of how shearing along fault zone surfaces affects properties and processes in the structures.

Two effects that we will *not* describe in detail, are the geochemical and thermal couplings to the rock-fluid system. While the hydraulic stimulation response can be impacted by these effects (see e.g. Finnie et al. (1979); Ghassemi (2012); Hou et al. (2017); Wintsch et al. (1995)), the GTS experiment lasts for a relatively short time and uses normal water at constant in-situ temperature of $11\ {}^\circ\mathrm{C}$. As such, we assume these processes have a negligible impact on the state and transient evolution of the rock-fluid system.

This chapter is structured as follows. In Section 2.1, basic properties of rocks are described, including the transition from microscale to macroscale properties. The composition and hydraulic structure of fault zones are described in Section 2.2. Finally, the hydromechanical mechanisms and response to shearing are discussed in Section 2.3.

2.1 Pores and cracks in subsurface rock

Rock is a natural porous material consisting of the rock fabric and void space along grain boundaries of the rock or through the rock grains, see Figure 2.2. The structure of the void space, or pores, influences properties like permeability and rock strength, while the meso-scale structure and defects are important to understand deformation and failure of the rock. The pores are connected by pore throats, which is the narrowest point of passage between two pores. Depending on rock type, the diameter of the pore throats span $3\ \mathrm{nm}$ to $\sim 500\ \mu\mathrm{m}$ (Zhang et al., 2016) and may significantly influence rock properties despite accounting for only $\sim 0.1\ \%$ of the porosity of some rock types (Shapiro et al., 2017).

The porosity refers to the ratio of the available *connected* (i.e. accessible) void to total volume within a rock and varies for different rock types. The porosity can be as large as $20\ \%$ for certain types of sandstone, or about $1\ \%$ for granitic rock. The heterogenous nature of naturally occurring rock and its deformation history can lead to a porous space of markedly non-elongated shape. On the microscopic scale, a porous space of non-elongated shape can occur overlappingly with porous space of elongated shape. These classes can be separated as (micro)*cracks* and *pores*, respectively (Paterson & Wong, 2005).

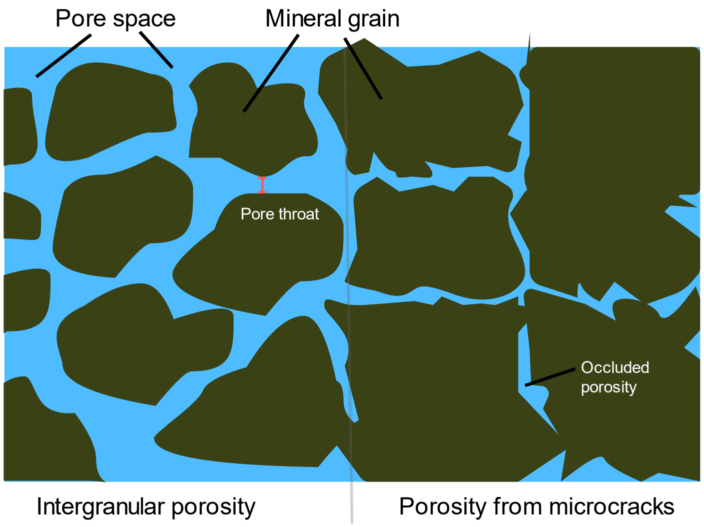

Figure 2.2 Illustration of the pore space. Rock porosity typically come from intergranular pores (left), or microcracks (right).

On the microscale, microcracks are rock discontinuities with length typically on the order of $100\ \mu\mathrm{m}$ and a crack aspect (width to length) ratio on the order of 10^{-3} to 10^{-5} (Kranz, 1983). It is understood that microcracks form from mechanical, thermodynamic, chemical, or pressure induced processes. Microcracks found in crystalline rock form predominately as the local stress exceeds the local rock strength, for example due to an applied deviatoric stress or stress concentrations around cavities or at grain boundaries (Kranz, 1983). The stress conditions to initiate microcracking may also be influenced by the pressure distribution of saturating fluid or due to deformation or failure of the intact rock.

Low-porosity rock such as granite is denoted *compact rock*. The porosity and permeability of compact rock are often controlled by microcracks (Paterson & Wong, 2005). The presence of microcracks may vary depending on the local stress conditions. With increasing normal stress, such as the hydrostatic stress at depth, it has been shown that crystalline rock has very few, if any, cracks in-situ. With applied deviatoric stresses on the rock mass however, the resulting state of the microcracks is extraordinarily complex. Each microcrack can open, close, propagate, or stop propagating (Kranz, 1983).

Core samples collected from the crystalline host rock at the GTS before the injection experiment are free of open microcracks (Wenning et al., 2018). The porosity is therefore expected to occur mainly due to intergranular pores, which are spherically shaped pores located predominately around the mineral grain boundaries (Wang et al., 2016). However, microcracks can still form from deformation of the shear zones and can therefore have an impact on the near-zone properties.

To enable macroscopic analysis of a rock volume, the heterogenous medium consisting of pores on the microscale are averaged over a scale where the microscopic phenomena can be ignored in favor of macroscopic physical phenomena of interest. To achieve this, we associate to the microscale properties, such as porosity, an elementary representative volume (REV) relevant to the macroscale over which the volumetrically averaged properties vary continuously. The assumption that this procedure is possible is referred to as the *continuity hypothesis*. The coalescence of cracks, forming fractures, joints, faults, and other macroscale structures may in regions of high heterogeneity inhibit the separation of length scales.

That is, the REV scale that is appropriate to homogenize the porous medium, may not be an appropriate REV scale for the cracks (Berryman & Wang, 1995; Boutin & Royer, 2015).

Furthermore, the hydrogeologic properties of pores and cracks occurring overlappingly in natural subsurface rock are often highly heterogenous. This motivates the treatment of cracks and pores as separate superimposed porous systems. Many approaches exist to achieve this, depending on which research questions are being posed and the capabilities of the physical laws and conceptual models used to describe the dynamics in these systems (e.g. Berre et al. (2019) and references therein).

2.2 Fault zone structure

The macroscopic formation of fractures under compressive load is a result of the coalescence of microcracks, as opposed to the continual propagation of a single microcrack. Fractures can be categorized as joints or faults. Faults are fracture surfaces where relative displacement has occurred along the nominal plane of the fracture (Jaeger, 2007). Joints are fracture surfaces where little such transverse displacement has occurred. Fractures are often approximately planar, and therefore provide planes along which sliding can occur.

Shear zones are zones that have experienced significant deformation surrounded by regions with less deformation. Shear zones can be categorized on a continuous scale between brittle and ductile depending on the deformation history. Brittle shear zones, or faults, are characterized by stress concentrations along very thin, discontinuous surfaces with physical properties often orders of magnitude dissimilar compared to the host rock. Ductile shear zones on the other hand tend to deform over larger regions, with stresses distributed throughout the zone. Ductile shear zones are typically also associated with the development of anisotropic structural properties along the elongated directions due to alignment of minerals (Mainprice, 2007; Wenning et al., 2018). Structures that share properties of both end-member types are often termed brittle-ductile shear zones.

The shear zones at GTS can be categorized as ductile and brittle-ductile (Krietsch et al., 2018a). However, brittle faulting has also occurred forming cohesive granular fault rock, incohesive fragmented rock and incohesive small-grained rock, denoted cataclasite, breccia, and fault gouge, respectively (Ziegler et al., 2013). The target shear zone of the hydraulic shearing experiment that was simulated in this thesis is ductile with a localized high strain zone that is hydraulically connected to nearby ductile shear zones through sub-parallel brittle fractures (Wehrens et al., 2017). The classical description of fault zones (see below) are for these reasons also useful to describe the shear zones at GTS (Brixel et al., 2020).

A typical fault is usually composed of multiple parts, each with a different hydrogeological structure (Faulkner et al., 2010). We call these the fault core, damage zone, and protolith. The fault core is the region where most displacement takes place during deformation or slip. The surrounding damage zone consists of smaller faults and fractures of varying lengths, orientations, and properties. The protolith is another term for the host rock that is not greatly influenced by the fault-related permeability structures (Caine et al., 1996).

Direct and dense measurements of a fault zone’s structure may be prohibitively difficult at depth; however, it is possible to infer its structure based on known controlling factors. These factors include depth, protolith lithology, tectonic movement, displacement history, frictional properties and fluid flow (Sibson, 1977).

The fault zone depth is a useful indicator for the damage zone structure. This is because many subsurface processes depend on the effective stress normal to the fault, and the in-situ temperature, both of which approximately have a linear relationship with depth in many geological conditions (Gupta & Roy, 2007; Tiab & Donaldson, 2012).

Depending on the deformation history, a fault zone may consist of only a single fault core. In this case, subsidiary faults or fractures may branch off from the core. On the other hand, the core itself may consist of multiple anastomosing (i.e. branching and reconnecting) cores, where the damage zone spans the entire core structure with variable degree of fracturing (Faulkner et al., 2010). These cores can be found on multiple scales. For example, the Carboneras fault in southeastern Spain consists of multiple cores ($< 5\ \mathrm{m}$ thick) and extensively damaged host rock, with a total damage zone width of more than $1\ \mathrm{km}$ (Faulkner et al., 2003). This case contrasts the instances where the bulk of the dynamics occur along discrete surfaces. As such, fault zones should in many cases instead be qualitatively understood as finite-width zones of fault rock, often with strikingly disparate properties compared to the protolith (Wibberley et al., 2008).

For compact rocks the fault core is generally fine-grained, as is observed at the GTS (Wenning et al., 2018). The surrounding damage zone is often dominated by fractures and other macro- and micro-structures that are often found to exponentially decrease in frequency as distance to the fault core increases (Faulkner et al., 2010). Additionally, the curvature of faults may affect the tendency for fractures in the damage zone to open or remain closed. For example, fracture opening could be favored on the top of anticlinal structures (Houwers et al., 2015).

2.2.1 Hydraulic structure of fault zones

Caine et al. (1996) presented a model that relates the fault zone structure to typical permeability architectures, as shown in Figure 2.3. The division is useful to understand how different combinations of fault core and damage zone size impact the permeability structure of the fault zone. Four end-member states can be described with this scheme, as summarized in the following. A *localized conduit* is characterized by one or more non-anastomosing, localized slip surfaces. The fault core and damage zone are hardly, if at all, developed. Fluid flow in this end-member category can best be modeled by conceptualizing the slip surfaces as discrete curviplanar surfaces. The *distributed conduit* is like the localized conduit in that the fault core is poorly developed. However, fluid may flow along numerous fractures, slip surfaces or deformation bands. A *localized barrier* is characterized by a larger fault core, but undeveloped damage zone. The fault core inhibits crossflow like an aquitard, which contrasts the more permeable nearby protolith. Examples of this include structures with cataclastic deformation bands (Ballas et al., 2015). Finally, the *combined conduit-barrier* is characterized by a cataclastic fault core that inhibits cross flow surrounded by a highly permeable damage zone composed of slip surfaces and fracture networks.

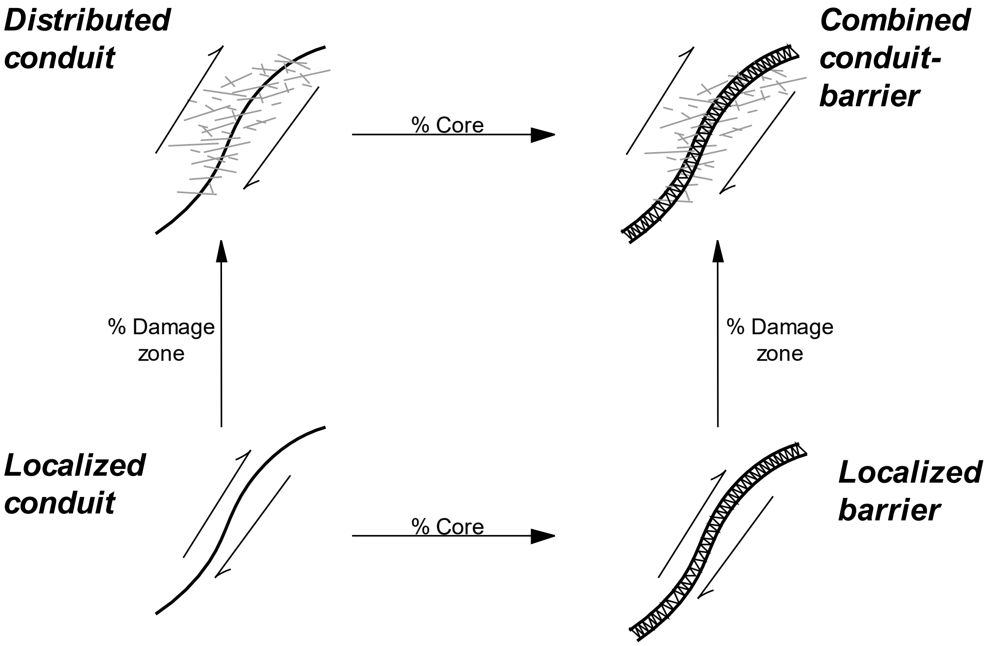

Figure 2.3 Conceptual models for fault zone permeability structure. Redrawn from Caine et al. (1996).

2.3 Hydraulic stimulation of fractured rock

A distinction can be made between hydraulic stimulation caused by hydraulic fracturing of faults or intact rock, and hydraulic shearing of existing faults. In hydraulic fracturing, the fluid pressure exceeds the minimum principal compressive stress (σ_3). If the process occurs in intact rock, then a tensile fracture forms which is oriented normal to σ_3 (Zoback et al., 1977). However, if the process occurs in a network of fractures, then the propagation mechanism also depends on factors such as the orientation of incident fractures (Blanton, 1982; Lamont & Jessen, 1963; Zhou & Xue, 2011).

In contrast, hydraulic shearing of pre-existing faults typically occurs at lower pore pressures (de Pater & Beugelsdijk, 2005). Consequently, the flow pathways should be sufficiently connected in order to avoid excessive build-up of fluid pressure (Berkowitz, 1995; Lutz et al., 2010). Additionally, the stress regime needs to be sufficiently anisotropic (Pine & Batchelor, 1984), and the faults need to be favorably oriented with respect to the local stress state (Lutz et al., 2010; Murphy & Fehler, 1986).

Hydraulic shearing can be induced both in the so-called primary effected zone and the secondary effected zone (Krietsch et al., 2020). In the primary effected zone, hydraulic shearing is a result of an increase of pore pressure which reduces the effective stress normal to the fault. If the shear stress overcomes the frictional resistance to sliding, the fracture slips. In the secondary effected zone, poroelastic effects can induce slip on faults that are outside the region with elevated pore pressure, for example due to stress redistribution caused by slip on faults within the primary effected zone.

There are several conditions that influence the concomitant transmissivity increase, such as slip-induced dilatancy, normal load, and production and compaction of fault gouge.

Slip-induced dilatancy refers to the process where shear displacement of a fracture causes separation of the fracture surfaces due the roughness and rigidity of the rock (Zhou et al., 2018). The surface separation, or aperture, provides additional volume for fluid flow, effectively increasing the fracture transmissivity. For hard rocks, the transmissivity can be enhanced by several orders of magnitude (Y. Guglielmi et al., 2015; Krietsch et al., 2020), and is considered irreversible in subsurface conditions (Lee & Cho, 2002). However, there is an upper limit to dilation due to shearing which is related to the height of the asperities in the fracture (Esaki et al., 1998). This limits the transmissivity enhancement due to hydraulic shearing.

The shearing process can produce fault gouge from crushing of the rough fracture surfaces. The presence of gouge generally inhibits flow and may be further amplified by compaction due to the normal stress acting to compress the gouge. Lee and Cho (2002) found that gouge production counteracted dilatancy beyond 7-8 mm. This should be understood in the sense that, while the maximum void aperture increases due to shear, the mean aperture remains constant, and therefore the transmissivity remains at most constant for extended shear (Zhou et al., 2018).

The non-linear relationship between the separation of fracture surfaces and transmissivity has prompted the introduction of the mechanical and hydraulic aperture. The mechanical aperture usually refers to the mean distance between the fracture walls. In the idealized case of a fracture that is planar and smooth (i.e. no roughness) and with a constant separation between the fracture surfaces, the fluid flow within the fracture can be solved analytically which leads to a result known as the cubic law (Witherspoon et al., 1980),

$$T = \frac{\rho_f g b^3}{12\mu}$$

where ρ_f $\left(\mathrm{kg\,m^{-3}}\right)$ and μ $(\mathrm{Pa\,s})$ are the fluid density and viscosity, respectively, g $\left(\mathrm{m^2 s^{-1}}\right)$ is the gravitational acceleration, T $\left(\mathrm{m^2 s^{-1}}\right)$ is the transmissivity, and b (m) denotes the hydraulic aperture. Transmissivity is the flow rate through a unit width of rock under a unit hydraulic gradient (see Appendix 8.1 for details). For a rough-walled fracture, the hydraulic aperture is the aperture of a smooth and planar fracture with parallel walls that would produce the same flow rate for a given pressure gradient as the rough-walled fracture (Lavrov, 2017).

The fracture roughness causes the flow to become more tortuous and non-laminar, reducing the effective flow rate. This implies that the hydraulic aperture is smaller than the mechanical aperture (Barton et al., 1985). Lavrov (2017) suggested the hydraulic aperture could be as much as $5 - 10$ times smaller than the mechanical aperture. In laboratory experiments, relationships between the mechanical and hydraulic aperture have been proposed. Barton et al. (1985) used concepts related to surface roughness to devise a model to relate the mechanical and hydraulic aperture. For small apertures, a highly non-linear relationship is expected. For large apertures on the other hand, the hydraulic and mechanical apertures tend to be similar.

A distinction should be made between fractures in contact, and not in contact. While Witherspoon et al. (1980) suggested that the cubic law is valid in either case with little to no modifications, later studies by Bandis et al. (1983); Barton et al. (1985) and others found that normal loading may have significant impact on fracture closure up to a state of maximum closure. Moreover, mismatches between fracture surfaces subject to normal loading induce other non-linear behavior. A more recent study by Oron and Berkowitz (1998) suggested that both the geometry and area fraction of contact regions may cause faster-than-cubic decrease in transmissivity as the contact area non-linearly increases. Lee and Cho (2002) saw similar results in granite for small mechanical apertures and stresses above 3 MPa. Although several studies have explored relations that account for fracture asperities and surface roughness (e.g. Kamali and Pournik (2015); Zimmerman et al. (1992); Zimmerman et al. (1991)), the unmodified cubic law, as a lowest-order approximation, is expected to be sufficiently accurate for fracture surfaces of considerable separation (Brown, 1987).

3 Conceptual model for flow and mechanics in fractured porous media

The hydromechanical dynamics in natural subsurface rock are extraordinarily complex due to the interaction between the porous rock and discontinuous fractures in addition to the coupling between the hydraulic and mechanical processes. The proper equations to model hydromechanical interactions in a rock volume depends on the assumptions of the conceptual representation of the rock volume itself. Different conceptual models for flow and mechanics in fractured porous media are well-suited to accurately model different aspects of interest to the modeler. Additionally, the model choices require different kinds of solution strategies that demand different amounts of computing resources. Generally, we would like to minimize the computer resources needed to find a satisfactory solution to the problem at hand.

This chapter presents three common conceptual frameworks used to model hydro-mechanical processes in fractured porous media, as illustrated in Figure 3.1. The end-member cases of (multi-)continuum models and discrete fracture network (DFN) models are characterized by only modeling the continuous medium or the discontinuous fractures, respectively. However, there are ways for multi-continuum models to incorporate ideas from discrete fracture models, and vice versa DFN models to use ideas from continuum modeling. DFN models have proven useful to simulate dynamics in large numbers of fractures across multiple scales. However, the lack of a representation of the continuum means that a well-connected network is needed for the approach to be useful. On the other hand, continuum models assume that parameters and variables are continuous, an assumption that may be too strong given the discontinuous nature of subsurface structures such as localized barriers or combined conduit-barriers.

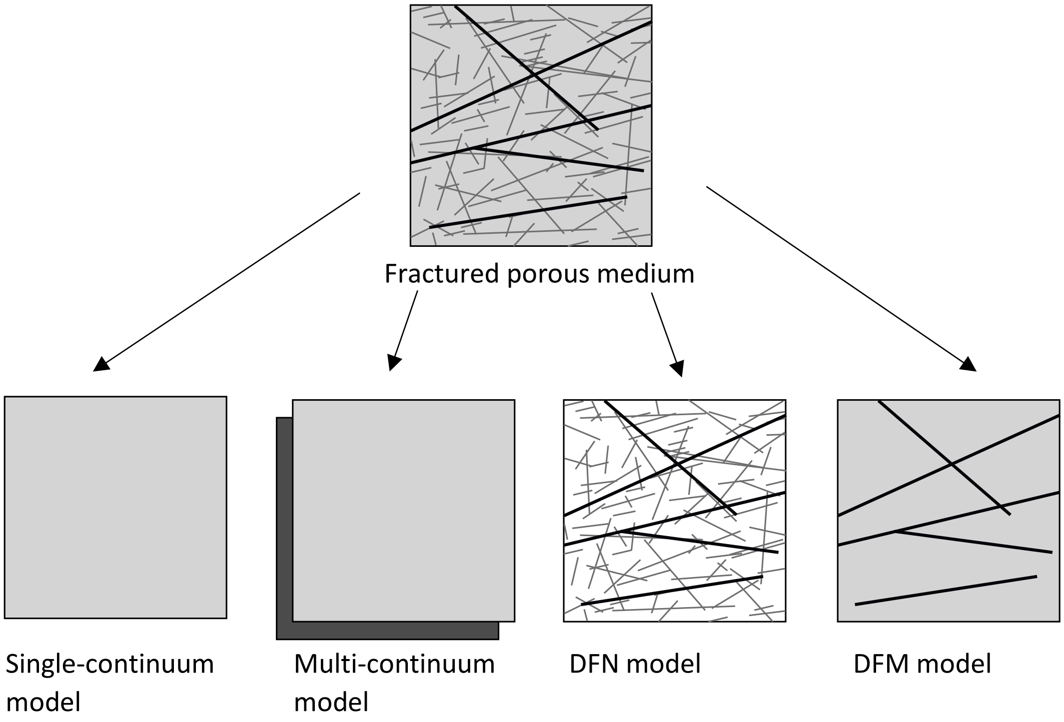

Figure 3.1 Illustration of conceptual models for fractured porous media. The figure is adapted from Sandve (2013).

A compromise between the two approaches are the discrete fracture matrix (DFM) models, characterized by explicitly representing both the fracture network and the continuum. These models are well-suited to apply different physical laws to the continuum and to the fractures which are tailored to the nature of the physical processes being studied. Owing to the high length-to-thickness aspect ratio of fractures, a reduction of dimensionality procedure allows fractures to be modeled as two-dimensional inclusions in the three-dimensional volume, which results in a mixed-dimensional model. We introduce the fracture aperture, which recognizes that the fractures has a volume and therefore allows for coupled equations to be posed in the continuum and the fractures in a dimensionally consistent way.

The mixed-dimensional DFM model used in this thesis is implemented in PorePy[1], a flexible, object-oriented modeling software implemented in Python (Keilegavlen et al., 2020). The framework allows the prescription of equations in each domain, and a physically meaningful description of the exchange of e.g. energy and mass between each domain (Reichenberger et al., 2006). The mixed-dimensional DFM meshes are generated using gmsh (Geuzaine & Remacle, 2009).

This chapter is structured as follows. Section 3.1 reviews single- and multi-continuum models including strategies to include fracture physics. In Section 3.2, DFN models are briefly described. Section 3.3 provides an overview of of DFM models. A description of mixed-dimensional DFM models is provided in Section 3.4, including explicit modeling of interfaces, fracture intersections, and operators to project variables between adjacent domains.

---

[1] https://github.com/pmgbergen/porepy

3.1 Continuum models

Continuum models are a broad class of models that implicitly represent fracture dynamics by altering the parameters of the continuum However, the fracture geometry is not explicitly modeled. Two common approaches are the single-continuum and the multi-continuum family of models. For the flow problem, both approaches attempt to identify an effective permeability $\mathcal{k}_e$ that incorporates the effects of the heterogenous porous medium containing a network of fractures of varying size, roughness, orientation, aperture, frequency, and gouge content. Using the standard Darcy relation for the specific flux and gradient of the pressure, we have

$$\langle q \rangle = -\left\langle \frac{\mathcal{k}}{\mu} \nabla (p + \mathcal{g}) \right\rangle = -\frac{\mathcal{k}_e}{\mu} \langle \nabla (p + \mathcal{g}) \rangle \tag{3.1}$$

where q is the flux, $\mathcal{k}$ is the permeability, μ is the viscosity, and $\mathcal{g}$ is an external potential field. The upscaling or averaging operator $\langle \cdot \rangle$ is the method that relates the average flux to the gradient of the pressure. Ideally, the volume over which the upscaling procedure is performed should correspond to a representative elementary volume (REV) containing the heterogeneous porous medium and the fractures. If we can find such an REV, then the single-continuum model is an upscaling procedure from microscale pores and cracks to a macroscale model where the permeability and porosity vary continuously in space.

Natural subsurface media are often found to have complex fracture networks, which can make it impossible to find an REV due to lack of scale separation. For example, a fracture with substantially different properties than the surrounding porous medium may span the domain of interest. Then an REV enclosing the fracture may be too large compared to the scale of the problem we are interested to solve.

The multi-continuum models try to alleviate this by introducing multiple continua, each with their own set of equations, and with transfer terms between the continua. However, for complex fractured porous media, challenges remain. First, the multi-continuum models, like the single-continuum models, assume that the upscaled parameters and variables within each continuum vary continuously in space. Furthermore, no general approach to formulate the transfer terms are known, although multiple are proposed (Berre et al., 2019).

Despite this, multi-continuum models are useful for their computational efficiency and ability to model certain aspects of porous media accurately. One such aspect is the modeling of pores and cracks. Pores may provide significant storage, while the cracks control permeability variations. In this case, a multi-continuum model may propose different constitutive relations for each continuum that accurately describe their influence on the dynamics. Note that blocking fractures do not contribute to flow, and therefore other models are usually preferred in those cases (Berre et al., 2019).

Some research has been invested in the extension to coupled stress and fluid flow models. Oda (1986) developed a model where cracks are replaced by parallel planar plates connected by springs and the elastic stiffness tensor and permeability tensor are replaced by equivalent quantities. The fracture network is therefore replaced by a model for an anisotropic, elastic porous medium accounting for fracture orientation, size, and aperture. A drawback of this approach is the assumption that the cracks are sufficiently small compared to the intact rock so that they can be replaced continuous equivalents.

Furthermore, certain assumptions are made on the origin of conductivity and the decomposition of the elastic strain, which may hold only in certain field cases. These assumptions are not based on a theoretical foundation in the sense of continuum mechanics.

Gan and Elsworth (2016) extended the crack model of Oda (1986) to include effects such as friction and aperture which depend on normal closure, shear dilation, and fracture opening. A dual continuum model is employed to model rock and fracture porosity. The framework can be interpreted as a discrete fracture model with explicit geometric consideration of fractures. However, the upscaled nature of continuum models implies that properties like the permeability are “smeared” in space. As such, the framework may be more suitable for simulation of long-term reservoir behavior, rather than detailed short-term simulations.

3.2 Discrete fracture network models

Discrete fracture network (DFN) models explicitly represents the geometric features of fractures such as extent, orientation, shape, and aperture in a computational framework while disregarding the explicit representation of the surrounding rock volume (Lei et al., 2017). Equations are only posed in the fractures, ignoring processes that occur in the intact rock. This approach may be favorable for compact rock, where the porosity of the host rock is incredibly low, and storage and conduction of fluid predominately takes place in fractures and faults.

For practical use in subsurface simulations, the initial location of the fractures must usually be known. This is often not the case due to sparse observations in the subsurface but is critical, for example, for a flow model since conduction through the domain occurs exclusively within the fracture network. Various statistics based on the field data can be used to stochastically generate realizations of well-connected fracture networks, for example by using methods of fractal geometry and power law models (Bonnet et al., 2001). The system of equations can then be solved for each realization. Since realizations are random, multiple realizations are often needed to constrain the uncertainty of the computed solution with respect to the location, geometry, and properties of the fractures (Ren et al., 2017).

For coupled processes such as hydraulic, mechanical, thermal, or chemical processes, additional methodology may be needed since these processes may also be sensitive to the unfractured part of the domain. For example, Koh et al. (2011) applied an iterative technique where the stress state at the previous time step is used to estimate the aperture distribution of the fracture network at the current time step. The aperture is then used to calculate an equivalent permeability for an upscaled continuum model, which then enables the estimation of the mechanical stress, displacement, fluid pressure, and temperature distribution in the reservoir.

3.3 Discrete fracture matrix model

Discrete fracture matrix (DFM) models are characterized by explicitly representing both fractures and the continuum (or matrix) and can therefore be viewed as a combination of continuum models and DFN models. For DFM models, small-scale fractures and cracks are typically upscaled to the matrix so that the parameter fields in the matrix considers the hydraulic and mechanical effects of the small-scale features. Many of the upscaling methods typically used for continuum modeling can be applied to DFM models. As opposed to continuum models however, macroscale fractures and faults are kept in the model, which means that the impact of the fracture geometry on the coupled dynamics can be directly modeled. For example, blocking fractures, such as localized barriers, can be modeled with DFM models, but not with continuum models.

Several classes of DFM models exist depending on the approach used to model the interaction between fractures and the matrix. Some models do not explicitly represent the fracture surfaces in the computational grid. Instead, fracture-matrix interaction is incorporated by modifying the numerical methods (see Keilegavlen et al. (2020) and references therein). These approaches result in so-called non-conforming meshes, where the grid cells in the matrix are not constrained by the geometric location or orientation of the fractures, see Figure 3.2. This can be an advantage in certain conditions, since the accuracy of the solution for a discretization scheme can depend on the quality of the mesh. Regular meshes for instance, can greatly improve the convergence properties of some discretization schemes.

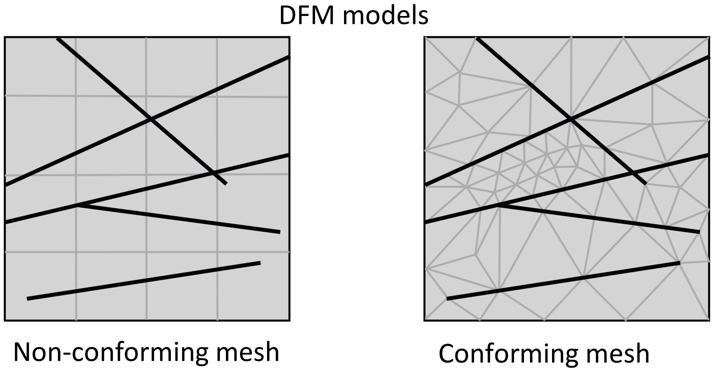

Figure 3.2 Illustration of discretization approaches for discrete fracture matrix models. The grey lines are the matrix mesh. The figure is adapted from Berre et al. (2019)

Other approaches introduce interfaces on the boundary between the matrix and the fractures. The meshes for these approaches are conforming. This means that the fracture surfaces are geometric boundaries for internal boundaries in the matrix, which generally needs unstructured meshes. Gebauer et al. (2002) presented an equidimensional approach where the fracture and matrix are modeled in the same dimension. Then, the governing equations are solved using a multigrid method based on a hierarchical decomposition of the fracture and intact rock. However, these methods can be computationally intensive for problems that has fractures with high aspect ratios. Instead, fractures can be modeled as lower-dimensional domains in the matrix.

3.4 Mixed-dimensional DFM model

The high-aspect ratio of fractures seen in subsurface media motivates a reduction of dimensionality procedure (Berre et al., 2018b). In a three-dimensional reservoir, fractures are modeled as two-dimensional inclusions and fracture intersections are modeled as one-dimensional inclusions. This approach is referred to as a mixed-dimensional DFM model, and is often computationally much more efficient (see e.g. Angot et al. (2009); Keilegavlen et al. (2020)) than equidimensional models with discrete fractures (Gebauer et al., 2002; Neunhäuserer et al., 2002). With this approach, each lower-dimensional inclusion of dimension d is the result of a reduction of $(3-d)$ dimensions compared to the 3d-matrix. At each point in the inclusion, we let a_d^V $[\mathrm{m}^{3\text{-}\mathrm{d}}]$ denote the magnitude of this reduction (Berre et al., 2018b). In practice, a_d^V is the length or cross-sectional area that is collapsed to produce a 2d-fracture or 1d-intersection, respectively. We refer to this variable as the *specific volume*. With proper formulation of the primary variables and equations on each domain, this results in a physically consistent modeling approach.

While natural fractures generally can be curviplanar, fractures in this thesis will represented fractures as discrete, planar, lower-dimensional structures of arbitrary orientation, and embedded in the 3D volume so that the fractures represent internal boundaries in the medium. We illustrate the mixed-dimensional geometry, including the hierarchical decomposition of geometric objects in Figure 3.3 (Keilegavlen et al., 2020).

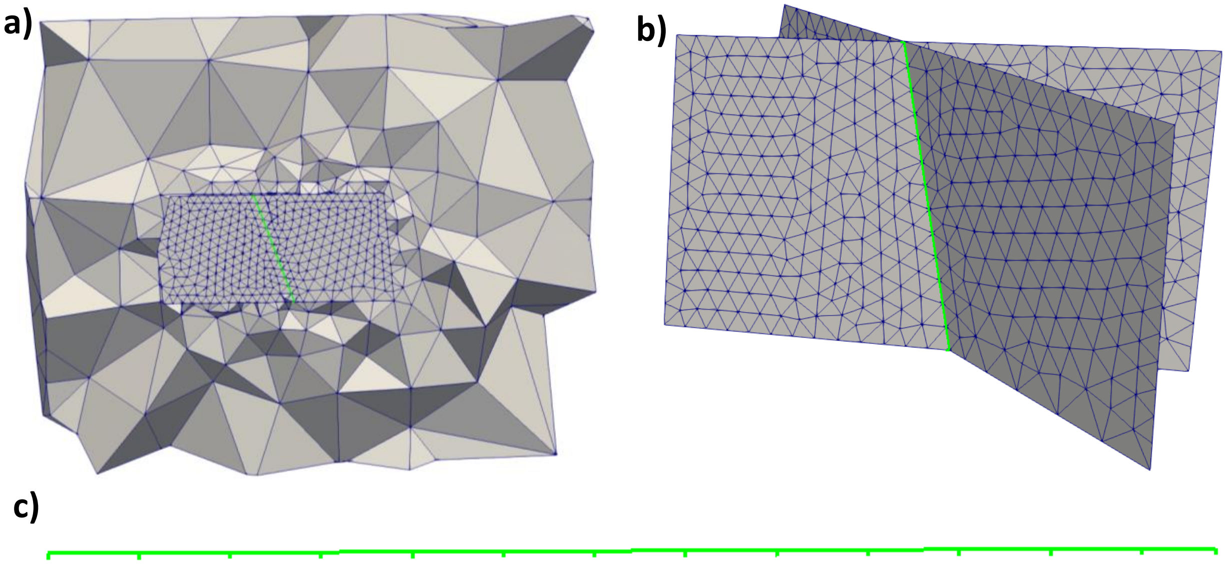

Figure 3.3 Illustration of a mixed-dimensional geometry, including mesh in 3D, 2D and 1D. ***a)*** *The 3D mesh is sliced to expose one of the fractures.* ***b)*** *The 2D fractures intersect, forming a one-dimensional domain along the intersection segment.* ***c)*** *The mesh for the 1D fracture intersection.*

3.4.1 Explicit representation of fracture intersections

The structure and physical processes occurring in one-dimensional fracture intersections can be complex (Abell et al., 2012). From a geological perspective, such intersections may be the result of a younger fault propagating through an older fault zone. It may not be entirely clear if the structure of these intersections should be thought of as a “direct” combination of the two fractures, or if one of the faults' properties is more significant to the structure of the intersection compared to the other. If one of the fractures undergoes shear deformation, the deformation may elongate the intersection or even "disconnect" the crossing fracture from the original location of the intersection line (c.f. Figure 2.1). Similarly, a propagating tensile fracture may create a new intersection by propagating through a pre-existing fracture. These observations obfuscate a clear path to modeling of intersections for most conceptual models. Therefore, some models have excluded explicit consideration of the one-dimensional fracture intersections arguing that the small volumes of the intersections lead to numerical instabilities. Instead, the intersections are viewed as a transition zone between the adjacent fractures and by modifying the discretizations, the physical properties and processes in the intersections can be accounted for (Karimi-Fard et al., 2004; Stefansson, 2016). The approach favored by the PorePy simulator allows for representation of all types of lower-dimensional domains (Keilegavlen et al., 2020). This is a major advantage over models that exclude explicit representation of intersections. By modeling intersections as separate subdomains, specialized equations and parameters can be selected to most accurately model the dynamics that occur in these structures.

3.4.2 Subdomain notation and interface projection operators

The DFM model in PorePy enables communication between variables in subdomains of different dimensions (Keilegavlen et al., 2020). The simulator limits direct communication to subdomains of co-dimension 1. This means that a 3D matrix can interact with 2D fractures, but not directly with 1D intersections. These interactions are accommodated by including interfaces that encapsulate the lower-dimensional objects. A 2D fracture, for example, has one interface on either side to facilitate interaction with the 3D matrix.

The interfaces are constructed to facilitate coupling between subdomains in the mixed-dimensional model. The interfaces have interface variables for physical quantities such as the fluid flux or contact traction. Through the use of various projection operators, variables in the lower-dimensional subdomain and variables adjacent to the internal boundary of the higher-dimensional subdomain can be mapped to the interface (or mortar) domain, and coupled to the interface variable. This coupling typically represents some constitutive relation between the dynamics in the subdomains.

Specifically, denote $\Omega_{d,i}$ the subdomain of dimension $d = \{1,2,3\}$, indexed by i. We omit the subscript i for any object if no ambiguity arises. We may have an arbitrary number of subdomains of dimension 1 or 2, but only one of dimension 3. The external boundary for each domain is denoted $\partial\Omega_d$, and is defined as the part of the boundary that is not adjacent to another domain of co-dimension 1. Internal boundaries are denoted $\partial\Omega_d^I$, and are geometrically superimposed on the adjacent lower-dimensional domains (of co-dimension 1) and the interfaces separating these domains. We denote the interface between a higher-dimensional subdomain Ω_h and a lower-dimensional subdomain Ω_l as $\Gamma_j \equiv \partial\Omega_h^I \cap \Omega_l$ (the index j depends on the indexes of the two subdomains, which is suppressed here). The two interfaces on either side of a lower-dimensional subdomain are identified by a superscript $+$ or $-$, which is arbitrary up to implementation in numerical software. This allows us to identify $\partial\Omega_h^+,\ \partial\Omega_h^-$, the sides of the higher-dimensional internal boundary adjacent to Γ^+ and Γ^-, respectively. Finally, we denote n_h the unit normal vector from $\partial\Omega_h^I$ to Ω_l, and n_l the unit normal vector from Ω_l to Γ^-. See Figure 3.4 for an illustration of the domains and interfaces (Stefansson et al., 2020b).

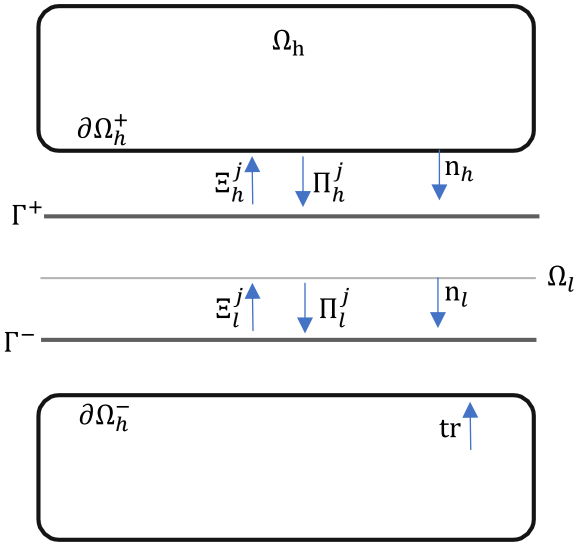

Figure 3.4 Schematic illustration of coupling operators between generic subdomains. The interfaces Γ^+ and Γ^- correspond to $\partial\Omega_h^+$ and $\partial\Omega_h^-$, respectively. The operators Ξ project from the interfaces to a subdomain, and the operators Π project from the subdomains to the interfaces. The trace operator tr projects to the internal boundary of Ω_h. Geometrically, all surfaces between $\partial\Omega_h^+$ and $\partial\Omega_h^-$ coincide. The figure is adapted from Stefansson et al. (2020b).

We define the projection operators as follows (Keilegavlen et al., 2020). The mapping of a variable from an interface to a subdomain is indicated by Ξ, while the mapping from a subdomain to an interface is denoted Π. The operators are subscripted by h and l, corresponding to Ω_h and Ω_l, respectively, and superscripted by j, corresponding to Γ_j. For example, $\Xi_h^j v_j$ denotes the mapping of the interface variable v_j from the interface Γ_j to the boundary of higher-dimensional domain, $\partial\Omega_h^I$. The mapping Π_h^j for a variable $\xi \in \Omega_h$ is achieved by introducing a suitable trace operator that projects the variable to the internal boundary $\partial\Omega_h^I$, $\mathrm{tr} : \ \Omega_h \rightarrow \partial\Omega_h^I$. Then, the projection of ξ to Γ_j is $\Pi_h^j \mathrm{tr}(\xi)$.

4 Governing equations

This chapter describes a model that couples fluid flow and deformation in a three-dimensional domain to an arbitrary number of two-dimensional fractures in which fluid flow, traction balance, non-penetration, and a friction law are modeled. Fractures are also coupled to fracture intersections, in which fluid flow is modeled. The model is used to explore the hydraulic and mechanical response to fluid injection in isothermal conditions. The model reflects geological conditions typical to Enhanced Geothermal Systems (EGS), where multiple shear zones, fractures and faults of variable thickness, conductivity, and orientation interact with the host rock. The model assumes isothermal, single-phase flow, and small deformations in a linearly elastic medium. Matrix hydraulic and mechanical properties are temporally invariant, while fractures deform according to a Coulomb type friction law and contact model. Formation and propagation of fractures is not modeled.

4.1 The Biot model for poroelasticity

The poroelastic model describes the dynamics of a system consisting of a skeletal framework of bulk porous material that is saturated by a fluid. Changes to the stress in the porous material affects fluid pressure, and changes in the fluid pressure or fluid mass induces volumetric changes in the porous material.

Biot's linear poroelastic model is expressed in terms of two independent variables and their coefficients. The basic variables to describe the effects on the solid are stress or strain. Likewise, the effects on the fluid are expressed in terms of pore pressure or increment of fluid content. Strain is a second-rank tensor, which for small deformations is linearized as the symmetric part of the displacement gradient,

$$\boldsymbol{\varepsilon} = \mathrm{sym}(\nabla u) = \frac{1}{2}(\nabla u + \nabla^T u). \tag{4.1}$$

The volumetric (or bulk) strain ε_V measures the deformation of the REV with volume V, and is defined as the sum of the normal strains which also equals the divergence of the displacement. With the convention that extensional strains are positive,

$$\varepsilon_V = \frac{\delta V}{V} = \mathrm{tr}(\boldsymbol{\varepsilon}) = \nabla \cdot u. \tag{4.2}$$

The increment of fluid content ζ is the fractional volume of fluid added to a control volume, and can be defined as the change in fluid mass content (fluid mass per unit reference volume) m_f relative to an initial state m_{f_0}, normalized by the initial density ρ_{f_0} (Wang, 2000),

$$\zeta \equiv \frac{m_f - m_{f_0}}{\rho_{f_0}} \equiv \frac{\delta m_f}{\rho_{f_0}}. \tag{4.3}$$

The fluid content was used as a basic variable by Biot (1941), and is convenient because it is dimensionless, as opposed to the related state variable density, which is used in e.g. Botti et al. (2020); Garipov et al. (2016); Salimzadeh et al. (2018).

The linear constitutive equations can be described in terms of (a) stress or strain, and (b) pore pressure or increment of fluid content. This leads to four complementary formulations for the relations between these variables. For the finite volume discretization methods used in this thesis, strain and pore pressure are most convenient to work with as independent variables. A formulation of this type is termed a mixed stiffness formulation in the literature (Wang, 2000). To illustrate the structure of the relations, consider an isotropic medium with an isotropically applied stress σ that is positive for tensile stresses. Two linear constitutive equations are sufficient to describe the dependent variables in terms of the primary variables,

$$\sigma = a_{11}\varepsilon + a_{12}p \tag{4.4}$$

$$\zeta = a_{21}\varepsilon + a_{22}p \tag{4.5}$$

where each of the coefficients a_{ij} are determined by considering the incremental change in the dependent variable to its corresponding independent variable, where the other independent variable is held constant. For example, a_{11} is obtained by measuring the stress response due to changes in the applied strain, subject to constant pore pressure,

$$a_{11} = \left.\frac{\partial\sigma}{\partial\varepsilon}\right|_{p=0}. \tag{4.6}$$

These coefficients are termed *drained, undrained, constrained* or *unconstrained* for constant pressure, constant fluid content, constant strain, or constant stress, respectively (Wang, 2000). Biot (1941) showed that the coefficients are symmetric, i.e. $a_{12} = a_{21}$. This means that the coupling coefficient for the pore pressure in the stress – strain relation is identical to the strain in the fluid content – pressure relation.

In the most general linear case, for anisotropic stress and strain in non-principal coordinates, the mixed stiffness formulation reads

$$\boldsymbol{\sigma} = 2G\boldsymbol{\varepsilon} + \lambda\mathrm{tr}(\boldsymbol{\varepsilon})\boldsymbol{I} - \alpha p\boldsymbol{I} \tag{4.7}$$

$$\zeta = \alpha\mathrm{tr}(\boldsymbol{\varepsilon}) + S_\varepsilon p \tag{4.8}$$

where $\boldsymbol{\sigma}$ $[\mathrm{Pa}]$ is the total stress, G $[\mathrm{Pa}]$ is the shear modulus, λ $[\mathrm{Pa}]$ is Lamé's first coefficient, α $[-]$ is the Biot coefficient, and S_ε $[\mathrm{Pa}]$ is the constrained specific storage coefficient. The shear modulus and Lamé's first coefficient, collectively, constitute the Lamé parameters, which can be computed from Young's modulus and Poisson's ratio, two moduli commonly reported in the literature.

The constrained specific storage coefficient is an important coefficient for describing the physical system. Depending on various assumptions on the fluid – rock interactions, the coefficient can be parameterized with different moduli or compressibilities. If we assume that the porosity is constant for constant differential pressure (i.e. equal changes in confining pressure and pore pressure), then the constrained specific storage coefficient S_ε can be expressed as,

$$S_\varepsilon = c_f\phi + \frac{\alpha - \phi}{K_S} \tag{4.9}$$

where c_f $\left[\mathrm{Pa}^{-1}\right]$ is the fluid compressibility, K_S $[\mathrm{Pa}]$ is the bulk modulus of the solid matrix composing of the porous skeleton, and ϕ $[-]$ is the porosity.

4.2 Poroelastic mechanical model

The poroelastic mechanical model is based on the quasi-static momentum balance equation for an elastic porous medium, which reads

$$\nabla \cdot \boldsymbol{\sigma} + f = 0 \tag{4.10}$$

where $\boldsymbol{\sigma}$ $[\mathrm{Pa}]$ is the total stress and f $\left[\mathrm{Pa\ m}^{-1}\right]$ is the body force per unit volume (Coussy, 2003). The stress represents the combination of the stresses of both the fluid and solid skeleton. Under the assumptions of small deformations in a linearly elastic medium, we can express the constitutive relation for the stress as

$$\boldsymbol{\sigma} = \boldsymbol{\sigma}' - \boldsymbol{\alpha} p = \mathcal{C} : \boldsymbol{\varepsilon} - \boldsymbol{\alpha} p \tag{4.11}$$

where $\boldsymbol{\sigma}'$ $[\mathrm{Pa}]$ is the effective mechanical stress tensor, $\boldsymbol{\alpha}$ $[-]$ is the Biot coupling tensor, $\mathcal{C}$ $[\mathrm{Pa}]$ is the fourth-order stiffness tensor, $\boldsymbol{\varepsilon}$ $[-]$ is the strain tensor, and p $[\mathrm{Pa}]$ is the fluid pressure. The Biot coupling tensor is usually approximated as isotropic, such that

$$\boldsymbol{\alpha} = \alpha\boldsymbol{I} \tag{4.12}$$

where $\boldsymbol{I}$ is an identity tensor, and α $[-]$ is the Biot coefficient.

For isotropic media, the stiffness tensor can be expressed as a linear combination of any two moduli among the elastic moduli for isotropic materials. For instance, with the Lamé parameters,

$$\mathcal{C} : \boldsymbol{\varepsilon} = 2G\boldsymbol{\varepsilon} + \lambda\,\mathrm{tr}(\boldsymbol{\varepsilon})\,\boldsymbol{I} = G(\nabla u + \nabla^T u) + \lambda\,\mathrm{tr}(\nabla u)\boldsymbol{I}. \tag{4.13}$$

However, any two of the other moduli, bulk modulus K $[\mathrm{Pa}]$, Young's modulus E $[\mathrm{Pa}]$, Poisson's ratio ν $[-]$, or P-wave modulus M $[\mathrm{Pa}]$ may also be used. Commonly measured moduli in geological characterization studies are Young's modulus and Poisson's ratio, which are related to the Lamé parameters by

$$E = \frac{G(3\lambda + 2G)}{\lambda + G}, \qquad \nu = \frac{\lambda}{2(\lambda + G)}. \tag{4.14}$$

Integrating Eqn. 4.10 over the domain Ω, applying Eqn. 4.11 and using the divergence theorem, the equation describing the mechanical state in the intact rock is given by

$$\int_{\partial\Omega} (\mathcal{C} : \boldsymbol{\varepsilon} - \alpha p\boldsymbol{I}) \cdot n\, dA + \int_{\Omega} f\, dV = 0. \tag{4.15}$$

4.3 Poroelastic flow model

4.3.1 Mass balance

Biot and Willis (1957) expressed continuity of the fluid as a balance of the increment of fluid content with the bulk relative displacement of the fluid and solid scaled by the porosity,

$$\zeta = -\nabla \cdot \left[\phi\left(U_f - U_s\right)\right] \tag{4.16}$$

where the subscripts $\{f, s\}$ refer to the displacement of the fluid and solid, respectively. The porosity appears because it corresponds to the fraction of the overall volume occupied by the fluid and may be taken outside the divergence operator for spatially invariant porosity. Since the increment of fluid content is taken positive for fluid added to the REV, a negative sign appears in Eqn. 4.16. By taking the time-derivative of Eqn. 4.16 for constant porosity, we get

$$\frac{\partial \zeta}{\partial t} = -\nabla \cdot \left[\phi\left(\frac{\partial U_f}{\partial t} - \frac{\partial U_s}{\partial t}\right)\right] \equiv -\nabla \cdot q \tag{4.17}$$

where $q \equiv \phi\left(\dot{U}_f - \dot{U}_s\right)$ is the relative velocity through the pores, between the fluid and the solid, usually referred to as the *specific discharge*. The dot is shorthand for time derivative, $\dot{x} \equiv \partial x / \partial t$.

An additional term Q can be added to the right-hand side of Eqn. 4.17 to account for the rate of fluid per unit time added to the REV,

$$\frac{\partial \zeta}{\partial t} + \nabla \cdot q = Q \tag{4.18}$$

which is an expression for mass balance for the fluid. For an incompressible fluid, the fluid density stays constant. Then, the increment of fluid content would only depend on the changes in the pore volume. Complementary, for an incompressible rock, the fluid content would only change due to the fluid compressibility $\left(c_f\right)$, i.e. $\zeta = \phi c_f p$ (Wang, 2000).

4.3.2 Darcy's law

Darcy's law is a linear constitutive relation that relates the specific discharge and the fluid pressure. It was originally conceived for the one-dimensional case in 1856 by Darcy through numerous experiments in a vertical sand column (Wang, 2000). The three-dimensional form of Darcy's law, which holds under the assumption of laminar flow, can be stated for an arbitrary fluid as follows,

$$q = -\frac{\mathscr{k}}{\mu} \nabla(p + \mathscr{g}) \tag{4.19}$$

where $\mathscr{g}$ is an external potential field, in most cases the gravitational potential, $\mathscr{g} = \rho_f g z$, $\mathscr{k}$ $\left[\mathrm{m}^2\right]$ is a second-rank symmetric tensor termed the intrinsic permeability, and is understood to be a function of the pore geometry. The term μ $[\mathrm{Pa\ s}]$ is the fluid viscosity.

4.3.3 Transient fluid flow

The partial differential equation governing fluid flow is derived by combining Darcy's law (Eqn. 4.19) with the fluid continuity equation (Eqn. 4.18),

$$\frac{\partial \zeta}{\partial t} - \nabla \cdot \frac{\mathscr{k}}{\mu} \nabla (p + \mathscr{g}) = Q. \tag{4.20}$$

We seek a mixed stiffness formulation where the fluid pressure and strain (or equivalently displacement) are primary variables, and stress and fluid content are functions of the primary variables. By substituting Eqn. 4.8 into Eqn. 4.20, we get

$$\frac{\partial}{\partial t}(\alpha \nabla \cdot u + S_\varepsilon p) - \nabla \cdot \frac{\mathscr{k}}{\mu} \nabla (p + \mathscr{g}) = Q \tag{4.21}$$

where S_ε is the constrained specific storage coefficient (ref. Eqn. 4.9). This equation is reminiscent to the hydrogeologic transient flow equation in a horizontal aquifer, with two exceptions (Wang, 2000). The specific storage is uniaxial in the groundwater case, and the coupling term $\alpha \nabla \cdot u$ is absent. With volumetric expansion, the REV can hold more fluid, causing effective influx of fluid and potentially reducing the pore pressure. Note that since $\nabla \cdot u \equiv tr(\boldsymbol{\varepsilon})$, strain and displacement are mathematically equivalent choices for the kinematic primary variable in the case of small deformations.

Integrating Eqn. 4.21 over the domain Ω and using the divergence theorem, the equation describing the fluid flow in the intact rock is given by

$$\int_\Omega \frac{\partial}{\partial t}(\alpha \nabla \cdot u + S_\varepsilon p)\, dV - \int_{\partial \Omega} \frac{\mathscr{k}}{\mu} \nabla (p + \mathscr{g}) \cdot n \, dA = \int_\Omega Q \, dV\,. \tag{4.22}$$

4.4 Flow in fractures

Fractures are complex structures with significant impact on fluid flow. Fractures are assumed to always allow fluid flow due to fracture surface roughness which provides void space for the fluid. This allows us to relate the hydraulic aperture to the fracture transmissivity through the cubic law (see Section 2.3). The hydraulic aperture can vary in space and time, which technically violates the "parallel plate" assumption of fractures. We assume these errors are small.

Shear zones will be modeled like fractures. The heterogenous properties of the core and damage zone with respect to the host rock result in complex flow patterns. We will assume that the damage zone does not have noteworthy influence on the hydraulic and mechanical dynamics. A single localized conduit (or barrier) is assumed to dominate the flow and deformation patterns. If multiple conduits are present, a single localized conduit is assumed to hydraulically close the other conduits. These simplifying assumptions allow us model shear zones (or faults) as discrete fractures.

With the mixed-dimensional model, we introduce two primary variables on the interfaces to couple the equations in the matrix and the fractures. Consider an interface Γ_j between the 3D matrix Ω_h and a 2D fracture Ω_l. The interface displacement is denoted $u_j \in \mathbb{R}^3$, and is restricted by the projection of the trace of u_h in Ω_h such that

$$u_j = \Pi_h^j \mathrm{tr}(u_h), \text{ on } \Gamma_j. \tag{4.23}$$

This naturally suggests that the internal boundary $\partial\Omega_h^I$ of Ω_h is governed by a Dirichlet condition for the momentum balance. We differentiate between the displacement u_j^+ on the positive interface Γ_j^+, and the displacement u_j^- on the opposing interface Γ_j^-. Then, the displacement jump is defined as $[u_j] \equiv \Xi_l^j(u_j^+ - u_j^-)$, from which we define the normal (scalar) and tangential (vector) components $[u_j]_n \equiv [u_j] \cdot \Xi_l^j n_l$ and $[u_j]_\tau \equiv [u_j] - [u_j]_n \Xi_l^j n_l$, respectively. The positive and negative interfaces are defined so that the normal displacement jump is non-negative, $[u_j]_n \geq 0$.

The interface flux is denoted by v_j and is required to satisfy

$$v_j = \Pi_h^j(q_h \cdot n_h), \text{ on } \Gamma_j \tag{4.24}$$

where q_h is the flux on $\partial\Omega_h^I$ (c.f. Eqn. 4.19).

In the 2D fractures, the primary variables are the fluid pressure p and the effective (tensile) contact pressure $\sigma' \in \mathbb{R}^3$. Due to Newton's third law, continuity of forces is needed on both sides of the fracture,

$$\Pi_l^j(\sigma' - p n_l) = \Pi_h^j\left(\boldsymbol{\sigma} \cdot n_h|_{\partial\Omega_h^+}\right) = -\Pi_h^j\left(\boldsymbol{\sigma} \cdot n_h|_{\partial\Omega_h^-}\right), \text{ on } \Gamma_j \tag{4.25}$$

Note that the total fracture stress does not depend on the Biot coefficient since the fracture is modeled as an open space, not a porous medium.

4.4.1 Flow in and across fractures

The flow in a fracture Ω_l is given by (Keilegavlen et al., 2020; Stefansson et al., 2020a)

$$\frac{\partial a_l^V}{\partial t} + a_l^V c_f \frac{\partial p}{\partial t} - \nabla \cdot \left(a_l^V \frac{\mathscr{k}}{\mu} \nabla(p + \mathscr{g}) \right) = Q + \Xi_l^j v_j. \tag{4.26}$$

For 2D fractures the specific volume equals the hydraulic aperture, $a_l^V = b$. The term $\partial a_l^V / \partial t$ is the temporal volumetric increment due to changes in the displacement jump; for 2D fractures it is equivalent to $\partial b / \partial t$. The fracture permeability in the directions tangential and normal to the fractures can be imposed independently of each other. The permeability $\mathscr{k}$ in Eqn. 4.26 is the effective tangential permeability (Berre et al., 2018b), and is computed from the cubic law,

$$\mathscr{k} = k\boldsymbol{I} = \frac{b^2}{12}\boldsymbol{I} \tag{4.27}$$

where k $[m^2]$ is the isotropic tangential permeability. Therefore the full expression for the fracture conductivity is $a_l^V \mathscr{k}/\mu = b^3/(12\mu)\boldsymbol{I}$, which has an equivalent structure as the cubic law for the transmissivity (see Section 2.3). The flux v_j across the fracture – matrix interfaces is governed by a Robin-type interface condition. This term enters Eqn. 4.26 next to the source term. We compute a finite difference over half the fracture aperture, so that for each fracture interface, v_j satisfies (Berre et al., 2019; Martin et al., 2005)

$$v_j = -\frac{k^{\perp}}{\Pi_j^l \mu}\left(\frac{2}{\Pi_j^l b}\left(\Pi_l^j p_l - \Pi_h^j \mathrm{tr}(p_h)\right) + \Pi_l^j \nabla \mathscr{g}_l \cdot \Pi_h^j n_h\right), \text{ on } \Gamma_j \tag{4.28}$$

where $k^{\perp}$ $[m^2]$ is the effective normal permeability, which is the same as the isotropic tangential permeability (k) projected to the interface, $k^{\perp} = \Pi_l^j k$. Eqn. 4.28 represents the resistance to flow across the fracture, and may cause a jump in the pressure across the fracture. This allows us to model fractures as barriers to flow (for example localized barriers, Section 2.2.1). In that case, the permeability in the fracture is very low, and we will get a discontinuity in the pressure across the fracture (Berre et al., 2019). Since we think of the flux to occur normal to, yet within the fracture, we consider only the external force $\nabla \mathscr{g}$ in Ω_l as opposed to approximating a difference from higher- and lower-dimensional terms. The force is projected to the interface and dotted with the normal vector n_h so that only the part of the force normal to the fracture interface is taken into account.

Integrating Eqn. 4.26 over the domain Ω_l and using the divergence theorem, the equation describing the fluid flow in the fractures is given by

$$\int_{\Omega_l}\left(\frac{\partial a_l^V}{\partial t} + a_l^V c_f \frac{\partial p}{\partial t}\right) dV - \int_{\partial\Omega_l} a_l^V \frac{\mathscr{k}}{\mu} \nabla(p + \mathscr{g}) \cdot n \, dA = \int_{\Omega_l} Q \, dV + \int_{\Omega_l} \Xi_l^j v_j \, dV \, . \tag{4.29}$$

4.4.2 Flow in fracture intersections

Flow in fracture intersections is adapted from Eqn. 4.26, noting that since 3D-1D couplings are not considered, the volumetric increment due to expansion of the 3D matrix is not included,

$$a_l^V c_f \frac{\partial p}{\partial t} - \nabla \cdot \left(a_l^V \frac{\mathscr{k}}{\mu} \nabla(p + \mathscr{g})\right) = Q + \Xi_l^j v_j \tag{4.30}$$

where $a_l^V = b_l^2$ accounts for the volume of the collapsed dimensions. In the same way as for flow in fractures, it is the integrated formulation of the equation that is used in discretization. The aperture b_l is computed by projecting and averaging the aperture from the higher-dimensional neighboring domains. The flux the 1D-2D interface is adjusted to account for area of the fracture boundary through which the higher-dimensional flux flows,

$$v_j = -\left(\Pi_h^j a_h^V\right) \frac{k^{\perp}}{\Pi_j^l \mu}\left(\frac{2}{\Pi_j^l b_l}\left(\Pi_l^j p_l - \Pi_h^j \mathrm{tr}(p_h)\right) + \Pi_j^l \nabla \mathscr{g}_l \cdot \Pi_j^h n_h\right), \text{ on } \Gamma_j \tag{4.31}$$

4.5 Contact model

Fracture deformation is governed by two constitutive laws, a non-penetration law in the direction normal to the fracture, and a Coulomb friction law in the direction tangential to the fracture. The formulation of these laws are adapted from Berge et al. (2019). Let σ_n' and σ_τ' denote the normal and tangential components of σ', respectively (c.f. Eqn. 4.25). Also, recall that the displacement on the interfaces is computed from Eqn. 4.23.

The non-penetration law ensures that the fracture sides cannot penetrate each other, and thus governs the relation between the effective contact pressure and displacement in the normal direction:

$$\begin{aligned} [u_j]_n - \mathfrak{G} &\geq 0 \\ \sigma_n' \left([u_j]_n - \mathfrak{G} \right) &= 0 \\ \sigma_n' &\leq 0. \end{aligned} \tag{4.32}$$

The non-penetration law says that the normal component of the displacement jump is always non-negative. If the fracture faces are out of contact $\left([u_j]_n - \mathfrak{G} > 0 \right)$, then the total normal pressure in the fracture is governed by the fluid pressure (c.f. Eqn. 4.25). On the other hand, if the fracture surfaces are subject to an effective normal compressive pressure ($\sigma_n' < 0$), then the fracture faces must be in contact $\left(\text{i.e. } [u_j]_n - \mathfrak{G} = 0 \right)$. The parameter $\mathfrak{G} \geq 0$ is the gap between the fracture surfaces and depends on the displacement jump. In this thesis, we use

$$\mathfrak{G}\left([u_j]_\tau \right) = \mathfrak{G}_0 + \tan(\theta) \left\| [u_j]_\tau \right\| \tag{4.33}$$

where $\mathfrak{G}_0 \geq 0$ is the residual gap when no deformation has occurred and is typically set to zero. The second term is an empirical shear dilation relation, as described in Stefansson et al. (2020b) and illustrated in Figure 4.1. As we discussed in Section 2.3, shearing may induce dilation due to surface roughness. Herein, we assume the relationship is linear, and that the dilation angle θ is constant. Therefore, no upper limit on the dilation due to extended shearing is considered. Dilation is coupled directly to the contact conditions. This means that not only are the hydraulic parameters impacted by dilation through the cubic law (Eqn. 4.27), but also the deformation of the intact rock. This is in the sense of the balance between interface displacement and the displacement in the matrix adjacent to the fractures (see Eqn. 4.23). A positive fracture gap displaces the intact rock adjacent to the fracture.

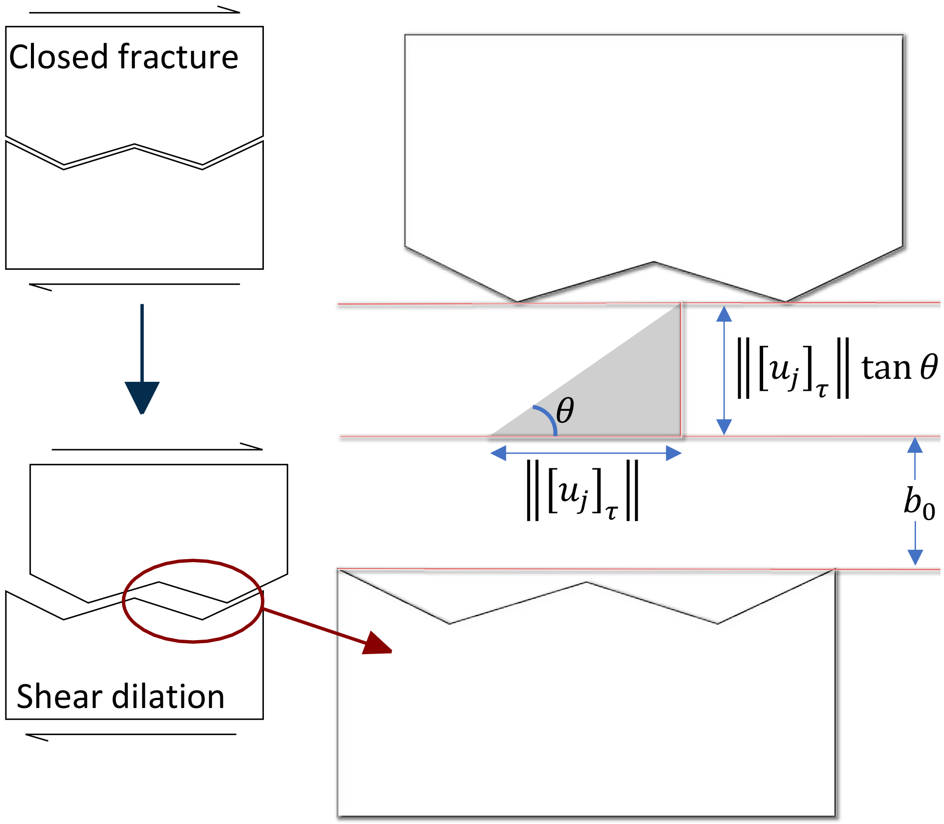

Figure 4.1 Shear dilation due to slip. The fracture aperture for a closed fracture is determined by the initial aperture b_0 *and the aperture due to shear dilation, which is the product of the shear and the tangent of the dilation angle,* $\left\|[u_j]_\tau\right\| \tan\theta$*. The figure is adapted from Koh et al. (2011).*

The equation for the fracture gap is linear. Therefore, the dilation is reversible if the displacement is reversed. In subsurface conditions however, slip is in practice irreversible since stress is relieved upon slip. Before any shearing has occurred, the fractures are typically somewhat conductive due to surface roughness. We take this into account by introducing an initial hydraulic aperture b_0, which can be computed from the initial transmissivity using the cubic law,

$$b = b_0 + [u_j]_n. \tag{4.34}$$

The Coulomb friction law provides conditions for slip to occur. Slip cannot occur unless the effective tangential stress exceed the effective normal stress multiplied with the friction coefficient $\mathfrak{F}$,

$$\begin{cases} \|\sigma'_\tau\| \le \mathfrak{F}|\sigma'_n| \\ \|\sigma'_\tau\| < \mathfrak{F}|\sigma'_n| \to [\delta u_j]_\tau = 0 \\ \|\sigma'_\tau\| = \mathfrak{F}|\sigma'_n| \to \exists \mathfrak{C} \ge 0 : \ \sigma'_\tau = -\mathfrak{C}[\delta u_j]_\tau \end{cases} \tag{4.35}$$

where $[\delta u_j]_\tau$ denotes the temporal increment of $[u_j]_\tau$. The friction law states that if the friction bound ($\mathfrak{F}|\sigma'_n|$) is not reached then the fracture faces are sticking, i.e. no change in the tangential displacement. On the other hand, if the bound is reached, then the slip direction is parallel to the tangential pressure.

Other than fixing the friction coefficient to a constant value as we do, two models are commonly used. The rate-and-state friction model models the friction coefficient in terms of the sliding velocity and a time-dependent state variable that is modeled by an ordinary differential equation (van den Ende et al., 2018). The static/dynamic friction model differentiates between a static friction coefficient that is active during sticking, and a dynamic friction coefficient that is active during sliding. The dynamic coefficient is lower than the static coefficient, which results in cascading sliding as parts of the fracture starts sliding. The friction immediately re-strengthens to the static value when sliding ceases (McClure, 2012).

4.6 Boundary conditions

The governing equations presented in Sect. 4.2 – 4.5 are complemented by a set of boundary conditions. Two types of boundary conditions are specified: boundary conditions on the external boundaries, and boundary conditions on the internal boundaries. On the external boundary, which typically is the external boundary for the 3D-matrix, we can assign a combination of Dirichlet and Neumann conditions.

For the mechanical model and flow model, we consider two independent partitions of the external boundary $\partial\Omega$. For the mechanical model, consider $\partial\Omega_{u,D}$ and $\partial\Omega_{u,N}$, satisfying $\partial\Omega_{u,D} \cup \partial\Omega_{u,N} = \partial\Omega$ and $\partial\Omega_{u,D} \cap \partial\Omega_{u,N} = \emptyset$, that represents the parts of the boundary for Dirichlet and Neumann conditions, respectively. Similarly, but independently, consider partitions of the external boundary for the flow model where Dirichlet and Neumann conditions are enforced. We denote these as $\partial\Omega_{p,D}$ and $\partial\Omega_{p,N}$, respectively. The boundary conditions can be summarized mathematically as:

$$u = \mathrm{g}_{u,D}, \text{ on } \partial\Omega_{u,D} \tag{4.36}$$

$$\boldsymbol{\sigma}' \cdot n = \mathrm{g}_{u,N}, \text{ on } \partial\Omega_{u,N} \tag{4.37}$$

$$p = \mathrm{g}_{p,D}, \text{ on } \partial\Omega_{p,D} \tag{4.38}$$

$$q = \mathrm{g}_{p,N}, \text{ on } \partial\Omega_{p,N}. \tag{4.39}$$

The internal boundaries $\partial\Omega^I$ are boundaries that separate domains of co-dimension 1. Consider an interface Γ_j that separates a higher-dimensional subdomain Ω_h and a lower-dimensional subdomain Ω_l.

On the internal boundary $\partial\Omega_h^I$ of Ω_h, we enforce a Neumann condition (c.f. Eqn. 4.24) (Martin et al., 2005),

$$q_h \cdot n_h = \Xi_h^j v_j, \text{ on } \partial\Omega_h^I. \tag{4.40}$$

In contrast, the interface flux is manifested as a source term on Ω_l, see Eqns. 4.26 and 4.30. On boundaries of the fractures or fracture intersections that are not adjacent to any interface, no-flow Neumann conditions are enforced.

For the contact problem, Dirichlet conditions are enforced on the internal boundaries $\partial\Omega_h^I$ of the intact rock (c.f. Eqn. 4.23), so that

$$\Xi_h^j u_j = \mathrm{tr}(u_h), \text{ on } \partial\Omega_h^I. \tag{4.41}$$

4.7 Gravitational effects

The necessary adjustments to include the effects of gravity in the equations are summarized in the following. Let the external potential field be $\mathscr{g} = \rho_f g z$. Thus, $\nabla \mathscr{g} = \left[0, 0, \rho_f g\right]^T$. The fluid density can be modeled by using an exponential function of the pressure (Berre et al., 2018a),

$$\rho_f = \rho_{f,0} e^{c_f (p - p_0)} \tag{4.42}$$

for a given reference pressure and fluid density, p_0 and $\rho_{f,0}$ respectively. To be concrete, we could consider the reference pressure $p_0 = 1 \text{ atm} = 0.1 \text{ MPa}$ and reference density $\rho_{f,0} = 1000 \text{ kg/m}^3$ at $11\ °\text{C}$.

The poroelastic mechanical model, Eqn. 4.10, subject to a gravity force $f = -\nabla \mathscr{g}$, can be expressed as

$$\nabla \cdot \boldsymbol{\sigma} - \begin{bmatrix} 0 \\ 0 \\ \rho_m g \end{bmatrix} = 0 \tag{4.43}$$

where ρ_m is the rock density. The transient fluid flow equation, Eqn. 4.21, can be expressed as

$$\frac{\partial}{\partial t}(\alpha \operatorname{tr}(\boldsymbol{\varepsilon}) + S_\varepsilon p) - \nabla \cdot \frac{\mathscr{k}}{\mu}\left(\nabla p + \begin{bmatrix} 0 \\ 0 \\ \rho_f g \end{bmatrix}\right) = Q. \tag{4.44}$$

Comparable results apply for fracture flow, Eqn. 4.26. For the fracture – matrix interface, Eqn. 4.28, we get

$$v_j = -\frac{k^\perp}{\Pi_j^l \mu}\left(\frac{2}{\Pi_j^l b}\left(\Pi_l^j p_l - \Pi_h^j \operatorname{tr}(p_h)\right) + \Pi_l^j \left[0,0,\left(\rho_f\right)_l g\right]^T \cdot \Pi_h^j n_h\right) \tag{4.45}$$

Due to the non-linearity of Eqn. 4.42, it can be challenging to directly include the expression for ρ_f in numerical simulations. Instead, one could argue that the density variations with respect to the expected pressure variations are exceedingly small for slightly compressible fluids such as water. Therefore, the pressure from the previous time step could be used to parameterize the density. Alternatively, one could include updates to density in the Newton iterations that are needed due to the contact conditions.

4.8 Dimensional analysis

The governing equations encompass dynamics on multiple scales. Scale disparities are manifested in the parameters of the governing equations and the scale of the solutions. When inverting the matrix representing the linear system of equations to find the solution, generally the solution will be less accurate if the entries in the matrix are far from unity. Preconditioners are one way to improve the solution accuracy (see e.g. Castelletto et al. (2018) and references therein). Another, conceptually much simpler approach is to scale the parameters and domain of the problem. To achieve this, we introduce dimensional scales and present the procedure to represent the system in non-dimensional form.

4.8.1 Matrix flow and deformation

The following dimensional scales,

L	[m]	characteristic length of the domain
P	[Pa]	characteristic magnitude of p and σ
T	[s]	characteristic time scale of observable dynamics

are used to transform the system to non-dimensional form. The coordinate transform

$$x = L\hat{x} \quad y = L\hat{y} \quad z = L\hat{z} \tag{4.46}$$

and substitutions

$$\begin{gathered} \mathscr{k} = L^2\hat{\mathscr{k}} \quad \mu = PT\hat{\mu} \quad Q = \frac{1}{T}\hat{Q} \quad p = P\hat{p} \quad \mathscr{g} = P\hat{\mathscr{g}} \\ S_\varepsilon = \frac{1}{P}\hat{S}_\varepsilon \quad \mathcal{C} = P\hat{\mathcal{C}} \quad f = \frac{P}{L}\hat{f} \quad u = L\hat{u} \end{gathered} \tag{4.47}$$

define the non-dimensional variables and parameters. We consider the governing equations 4.15 and 4.22, both in integrated form,

$$\int_{\partial\Omega} (\mathcal{C} : \boldsymbol{\varepsilon} - \alpha p \boldsymbol{I}) \cdot n \, dA + \int_{\Omega} f \, dV = 0 \tag{4.48}$$

$$\int_{\Omega} S_\varepsilon \frac{\partial p}{\partial t} + \alpha \frac{\partial(\nabla \cdot u)}{\partial t} \, dV - \int_{\partial\Omega} \frac{\mathscr{k}}{\mu} \nabla(p + \mathscr{g}) \cdot n \, dA = \int_{\Omega} Q \, dV \,. \tag{4.49}$$

Since the spatial coordinates are scaled, scaled variants of the linear operators must also be formulated. With a slight abuse of notation, we apply the substitutions

$$\begin{gathered} dA = L^2 d\hat{A} \quad dV = L^3 d\hat{V} \\ \nabla = \frac{1}{L}\widehat{\nabla} \qquad \nabla \cdot = \frac{1}{L}\widehat{\nabla} \cdot \quad \frac{\partial}{\partial t} = \frac{1}{T}\widehat{\frac{\partial}{\partial t}} \end{gathered} \tag{4.50}$$

noting that the gradient/divergence of the displacement is dimensionless. We find

$$PL^2 \left(\int_{\partial\Omega} \hat{\mathcal{C}} : \boldsymbol{\varepsilon} - \alpha \hat{p} \boldsymbol{I} \, d\hat{A} + \int_{\Omega} \hat{f} \, d\hat{V} \right) = 0 \tag{4.51}$$

$$\frac{L^3}{T} \left(\int_{\Omega} \hat{S}_\varepsilon \widehat{\frac{\partial}{\partial t}}(\hat{p}) + \alpha \widehat{\frac{\partial}{\partial t}}(\widehat{\nabla} \cdot \hat{u}) d\hat{V} - \int_{\partial\Omega} \frac{\hat{\mathscr{k}}}{\hat{\mu}} \widehat{\nabla}(\hat{p} + \hat{\mathscr{g}}) \, d\hat{A} - \int_{\Omega} \hat{Q} \, d\hat{V} \right) = 0. \tag{4.52}$$

The scaling of boundary conditions is reported for completeness. To conform with the numerical implementation, we consider Dirichlet conditions directly, but Neumann conditions integrated, so that

$$\begin{aligned} u &= \mathrm{g}_{u,D}, \text{ on } \partial\Omega_{u,D} & \int_{\partial\Omega} \boldsymbol{\sigma}' \cdot n \, dA &= \int_{\partial\Omega} \mathrm{g}_{u,N} \, dA \,, \text{ on } \partial\Omega_{u,N} \\ p &= \mathrm{g}_{p,D}, \text{ on } \partial\Omega_{p,D} & \int_{\partial\Omega} q \cdot n \, dA &= \int_{\partial\Omega} \mathrm{g}_{p,N} \, dA \,, \text{ on } \partial\Omega_{p,N}. \end{aligned} \tag{4.53}$$

Then, by applying the additional substitutions

$$\begin{aligned} \mathrm{g}_{u,D} &= L\hat{\mathrm{g}}_{u,D} \quad \mathrm{g}_{u,N} = P\hat{\mathrm{g}}_{u,N} \\ \mathrm{g}_{p,D} &= P\hat{\mathrm{g}}_{p,D} \quad \mathrm{g}_{p,N} = \frac{L}{T}\hat{\mathrm{g}}_{p,N} \end{aligned} \tag{4.54}$$

and by substituting relevant parts of Eqn. 4.47, 4.50 and 4.54 into Eqn. 4.53, we find consistent scaled boundary conditions.

4.8.2 Fracture flow

For the non-dimensional form of the equations in the fracture and fracture intersections, we note that for the flow model (Eqns. 4.26 and 4.30), the specific volume terms are defined to exactly account for the collapsed dimension that is not integrated over explicitly. For the fluid injection term, we have suppressed that it is integrated over the specific volume. This is because it is provided in integrated form, $\int_{\Omega} Q\, dV\ \ [L^3T^{-1}]$, for all dimensions. Finally, the flux terms are on the form $\left[a_h^V \cdot q_l\right] = \left[L^{3-(d+1)} \cdot LT^{-1}\right]$, so that integrated over the domain Ω_d yield terms with units $[L^3T^{-1}]$. With these remarks, the same procedure as in the previous section will yield a consistent non-dimensional form.

The contact laws should be straightforward.

5 Discretization

Discretization of differential equations is the process of approximating the operators in an equation in terms of a finite number of degrees of freedom in the domain. Most basic, and indeed most common, are the equations where the operators are linear in terms of the primary variables. The primary variables are arranged in a system and solved with the methods of linear algebra. In other cases, the physics cannot reasonably be described linearly. These problems are significantly more challenging because in general we have no guarantee to find a (unique) solution to the problem. One common approach consists of guessing a solution, then computing the direction in the n-dimensional solution space where the next solution would give a smaller error compared to the existing guess. The computation of this direction can be challenging due to unresolved non-linearities. Some methods apply a linearization scheme at this point to solve the global system in terms of increments of solutions in the estimated direction for the true solution.

In this chapter, we describe the core discretization methods for the poroelastic equations with contact mechanics that were introduced in Chapter 4. The full discrete system is cast in mixed-dimensional form, as presented in Chapter 3, which gives the global linear system a block type structure. For the system of governing equations, three classes of operators can be identified. There are terms that control the evolution of the primary variables through time (Eqns. 4.21, 4.26, 4.30), terms that combine a conserved flux with a first-order diffusion relation (Eqns. 4.10, 4.11, 4.19), and non-linear terms arising from the contact problem (Eqn. 4.35).

The chapter is structured as follows. In Section 5.1, the structure of the mixed-dimensional linear system is presented. In Section 5.2, we present details of the temporal discretization. Section 5.3 introduces finite volume methods for conservation laws, while Section 5.4 provides details on the multi-point finite volume schemes that are used to discretize Darcy's law for the fluid flux, and Hooke's law for linear elasticity. In Section 5.5, we present the discretization approach for the contact problem using a semi-smooth Newton method.

5.1 Structure of the mixed-dimensional system

We use a mixed-dimensional discrete fracture matrix (DFM) model with conforming meshes (see Section 3.4). Conforming meshes are attractive because there is a one-to-one correspondence between the cells in the lower-dimensional subdomain and the internal boundary of the higher-dimensional subdomain.

To understand the fundamental principles of the mixed-dimensional system, we consider a 3D domain (Ω_h) with one embedded 2D fracture (Ω_l). The poroelastic Biot equations in the higher-dimensional subdomain (Ω_h) are coupled to a frictional contact law and flow in the fracture. The primary variables are therefore displacement u and pressure p. These allow computation of stress/contact pressure σ.

The interface variables are interface displacement u and interface fluid flux v. Consider vectors of these variables for all degrees of freedom in each domain. We can visualize the mixed-dimensional system as a two-level block system of linear equations over the subdomains (Ω_h, Ω_l) and interface (Γ),

$$\begin{array}{c} \text{Eqn. ref} \\ 4.22 \\ 4.15 \\ 4.29 \\ 4.32, 4.35 \\ 4.28 \\ 4.25 \end{array} \left(\begin{array}{ccc} \overbrace{\begin{bmatrix} P & P_u \\ U_p & U \end{bmatrix}}^{\Omega_h} & \overbrace{\begin{bmatrix} & \\ & \end{bmatrix}}^{\Omega_l} & \overbrace{\begin{bmatrix} P_v & P_u \\ & U_u \end{bmatrix}}^{\Gamma} \\ \begin{bmatrix} & \\ & \end{bmatrix} & \begin{bmatrix} P & \\ & \Sigma \end{bmatrix} & \begin{bmatrix} P_v & P_u \\ & \Sigma_u \end{bmatrix} \\ \begin{bmatrix} V_p & \\ U_p & U_u \end{bmatrix} & \begin{bmatrix} V_p & \\ U_p & U_\sigma \end{bmatrix} & \begin{bmatrix} V & \\ & U \end{bmatrix} \end{array} \right) \begin{pmatrix} \begin{bmatrix} p \\ u \end{bmatrix} \\ \begin{bmatrix} p \\ \sigma \end{bmatrix} \\ \begin{bmatrix} v \\ u \end{bmatrix} \end{pmatrix}. \tag{5.1}$$

Here, each capitalized letter in the block matrix is the discretization matrix for a variable in an equation. The capital letters are the same along a given row since they identify the equation corresponding to the variable given by the lower-case variant of the diagonal entry. The subscripts identify coupling terms; notice that for each column, the subscripts are the same since they refer to the same variable. For instance, the first row is

$$(Pp + P_u u)|_{\Omega_h} + (P_v v + P_u u)|_{\Gamma}.$$

Symbols are interpreted according to the domain and equation they occur in. Therefore, no equivalence between the second and fourth term is implied. The empty blocks in Eqn. 5.1 indicate that the corresponding variable has no influence on the particular equation. For domains with additional fractures or fracture intersections, the block matrix structure is simply extended, but the main idea remains the same. For an appropriate right-hand side that contains the source terms, boundary conditions, and information from previous time steps or Newton iterations, we have a complete linear system for the coupled problem.

5.2 Temporal discretization

We consider a general time-dependent problem of the form

$$\frac{d\xi}{dt} = F(\xi) \tag{5.2}$$

where ξ is the unknown quantity to be determined in terms of the operator F. The standard way to approximate the time derivative is with a finite-difference scheme,

$$\frac{d\xi}{dt} \approx \frac{\xi^{k+1} - \xi^k}{\Delta t} + \mathcal{O}(\Delta t^2). \tag{5.3}$$

The significant question is how to evaluate the right-hand side of Eqn. 5.2. A computationally efficient option is the explicit time-stepping approaches, where we evaluate the new value ξ^{k+1} using the previous value ξ^k, that is,

$$\xi^{k+1} = \xi^k + \Delta t F(\xi^k). \tag{5.4}$$

The attractiveness of this approach lies in its simplicity, but it is limited by a constraint put on the time step Δt, which generally depends on the length scale of the spatial resolution of the domain. For parabolic equations there is generally a quadratic relationship between the timestep and length scale of the spatial resolution, $\Delta t \leq C\Delta x^2$, which becomes prohibitively restrictive for the problems and timescales we are interested in (Nordbotten, 2015). Therefore, a fully implicit time discretization that evaluates the operator F at the new time step is preferred,

$$\xi^{k+1} = \xi^k + \Delta t F\left(\xi^{k+1}\right). \tag{5.5}$$

The time step Δt is usually taken as a constant throughout simulations. For some problems it may be useful to consider robust methods to adapt the time step to capture large variations in the solution (see e.g. Grabowski et al. (1979)).

We also note that since we discretize the operator F using finite-volume methods, we will in practice solve the integrated equation

$$\int_\omega \xi^{k+1}\, dV = \int_\omega \xi^k\, dV + \Delta t \int_\omega F\left(\xi^{k+1}\right) dV\,, \tag{5.6}$$

over subdomains $\omega \subset \Omega$.

5.3 Finite volume methods

5.3.1 Basic continuous structure

This section introduces the basic concepts and features of finite volume (FV) methods, which are the class of methods we use to discretize the Biot equations. The Biot equations are a system of conservation laws, each of which can be formulated on the form

$$\frac{\partial \xi}{\partial t} + \nabla \cdot q = f \tag{5.7}$$

where ξ is the quantity to be conserved, q is a flux function, and f is a source term. We emphasize that this equation is a statement of the local conservation of the continuous quantity ξ. This implies that the divergence of the flux should exist pointwise. Alongside the conservation laws, the Biot equations also need so-called constitutive relations $q = f(\xi, \nabla\xi, \nabla^2\xi, \dots)$, which express some prior, empirical knowledge of the system. In this thesis, we are interested in first-order diffusive relations

$$q = \mathcal{C}\nabla\xi + g \tag{5.8}$$

where $\mathcal{C}$ is a symmetric, positive definite tensor, and g is an external force (i.e. a coupling term, in the context of the Biot equations). This equation is simply a notational short-hand for the flux term of Darcy's law and Hooke's law for linear elasticity. For example, Darcy's law can be recovered by identifying $\mathcal{C}$ as the permeability divided by viscosity and ξ as the pressure.

The equations 5.7 – 5.8 admit solutions given sufficient regularity of the variables (Nordbotten, 2015). When this is not the case, we seek solutions in the weak sense, where discontinuous solutions are permitted (Toro, 1999). Consider a domain $\Omega \subset \mathbb{R}^n$. Then, within any measurable subdomain $\omega \subset \Omega$, the accumulation of ξ is conserved (Nordbotten & Keilegavlen, 2020). Mathematically,

$$\frac{d}{dt}\int_\omega \xi\, dV + \int_{\partial\omega} q \cdot n\, dS = \int_\omega f\, dV\,, \tag{5.9}$$

where Stokes theorem was applied to get the second term, and n is an outward unit normal vector to ω. The subdomains ω are also referred to as control volumes or cells.

5.3.2 Basic discrete structure

To solve Eqn. 5.9 numerically, we subdivide Ω into a finite number of non-overlapping subdomains, enforce Eqn. 5.9 for each subdomain, and devise an appropriate method to discretize the flux term. We refer to Nordbotten and Keilegavlen (2020) in the following.

We discretize the domain Ω by identifying the pair $(\mathcal{T}, \mathcal{F})$. We define $\mathcal{T}$ to be the finite set of non-overlapping subdomains $\omega_k \subset \Omega$. We identify the set of faces of ω_k as the intersections $\partial\omega_k \cap \partial\mathscr{b}_i$, $\mathscr{b}_i \in (\mathcal{T} \cup \{\Omega\})$ having positive measure, and denote it $\mathcal{F}_k$. The set of all faces is then $\mathcal{F} = \bigcup_i \mathcal{F}_i$. We denote an arbitrary face by σ and note that i.e. $n_{\sigma,k}$ refers to the outward unit normal of ω_k restricted to the face $\sigma \in \mathcal{F}_k$. With these definitions, we reformulate Eqn. 5.9 for a subdomain ω_k,

$$\frac{d}{dt}\int_{\omega_k} \xi \, dV + \sum_{\sigma \in \mathcal{F}_k} \int_{\sigma} q \cdot n_{\sigma,k} \, dS = \int_{\omega_k} f \, dV \,. \tag{5.10}$$

For a suitable temporal method for the first term, we define the numerical scheme by the method that approximates

$$T_{\sigma,k} = \int_{\sigma} q \cdot n_{\sigma,k} \, dS \,. \tag{5.11}$$

We note that the integrated terms in Eqn. 5.10 are either assumed to be known, like the integrated source on the right-hand side, or have a simple form such that quadrature rules can be applied to compute the integrals. For example, the flux terms, q, will be assumed piecewise constant in each cell so that the integrated fluxes, $T_{\sigma,k}$ are easy to compute.

5.4 Multi-point finite volume methods

The multi-point finite volume (MPFV) methods is a family of cell-centered finite volume schemes which improves the well-known two-point flux approximation (TPFA) commonly used to solve first-order diffusive scalar problems. Two improvements of the classical method can be summarized as follows: 1) The multi-point flux approximation (MPFA) converges on non-K-orthogonal grids as the grid is refined, as opposed to TPFA. This means that the MPFA is suitable for unstructured grids. 2) MPFA can be extended to solve vector variable problems, for instance Hooke's law for linearly elastic materials, a method that is referred to as the multi-point stress approximation (MPSA) (Nordbotten & Keilegavlen, 2020).

The scheme is based on the construction of a refined grid in which local gradient unknowns are defined. The refined grid is constructed from the intersection of the primal grid with a dual grid. The cells in the dual grid are centered around the vertices (s_k) of the cells in the primal grid. For each pair of adjacent cells that are also adjacent to s_k, we split the face that is separating these cells along some central point x_σ, resulting in two subfaces. We denote the subfaces as $\tilde{\sigma}$. The cells in the dual grid are then formed around s_k by connecting the points x_σ and the cell centers x_k associated with each face and cell adjacent to s_k. Finally, we identify the refined grid as the intersection of the primal and the dual grid, as illustrated in Figure 5.1.

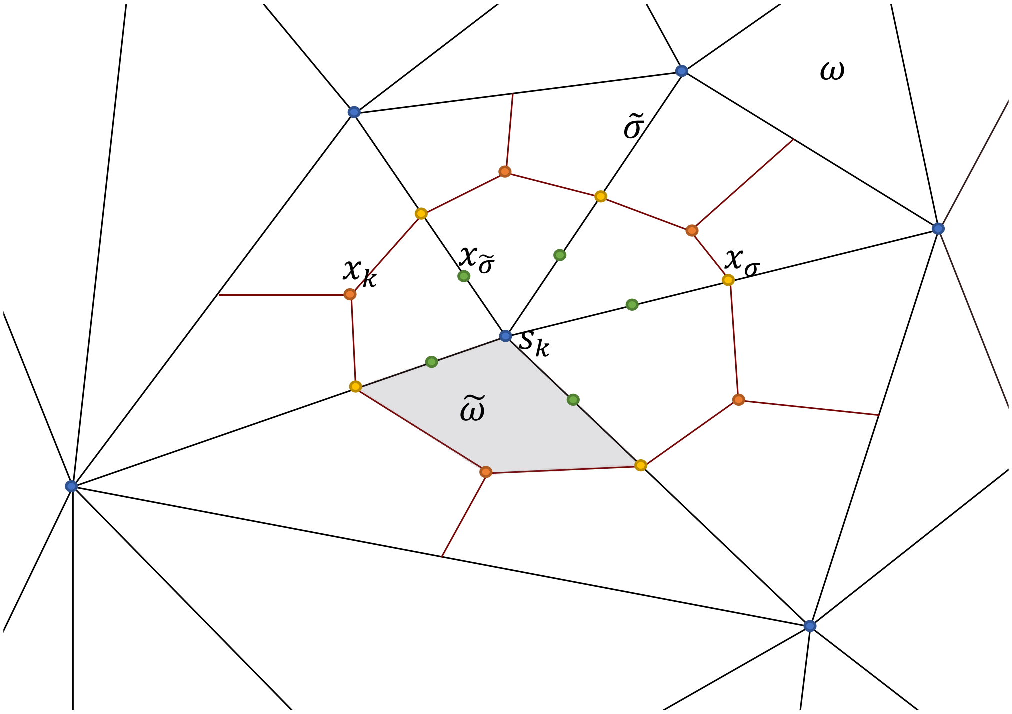

Figure 5.1 Visualization of primal grid with black grid lines, and the dual grid with red gridlines. The refined grid is the intersection of the primal and dual grid. The shaded region indicates a sub-cell in the refined grid. The local systems for MPFA and MPSA are constructed around the vertices s_k. Continuity of primary variables is enforced at $x_{\tilde{\sigma}}$. Flux balance is enforced across subfaces $\tilde{\sigma}$.

We refer to cells in the refined grid as sub-cells, denoted as $\tilde{\omega}$. In the sub-cells, the variables for pressure and displacement are assumed to be linear. Consequently, the gradients of these variables, denoted $\tilde{\nabla}\xi$, are constant. We enforce continuity of the local flux balance across the subfaces $\tilde{\sigma}$,

$$\int_{\tilde{\sigma}} q_{\tilde{\sigma},K} \cdot n_{\tilde{\sigma},K}\, dS = -\int_{\tilde{\sigma}} q_{\tilde{\sigma},L} \cdot n_{\tilde{\sigma},L}\, dS\,. \qquad (5.12)$$

The subscripts L and K specify quantities in the sub-cells ω_L and ω_K, respectively. The fluxes are defined according to the Darcy's law and Hooke's law, which, in each sub-cell depend on the local gradients for pressure and displacement, respectively. Additionally, for each subface $\tilde{\sigma}$, we enforce continuity in pressure and displacement on a point $x_{\tilde{\sigma}}$, which we refer to as a continuity point,

$$\xi_K + \tilde{\nabla}\xi_K \cdot (x_{\tilde{\sigma}} - x_K) = \xi_L + \tilde{\nabla}\xi_L \cdot (x_{\tilde{\sigma}} - x_L). \qquad (5.13)$$

Boundary conditions are applied by directly enforcing the discrete equivalents of the equations from Section 4.6. For Neumann conditions, the right-hand side of Eqn. 5.12 is modified, and for Dirichlet conditions, the right-hand side of Eqn. 5.13 is modified.

Around each vertex s_k and using Eqns. 5.12 and 5.13, we can form a local linear system of equations to express the local gradients $\widetilde{\nabla}\xi$ in terms of the cell-center primary variables. This allows us to formulate and solve the global linear system only with respect to the cell-center primary variables.

Discretization of the coupled HM-equations are achieved by using the total stress (cf. Eqn. 4.11) when enforcing the local flux balance (Eqn. 5.12). This is the term P_u in block (1,1) in Eqn. 5.1, which is the impact of pressure on the momentum balance. The coupling of mechanical effects in the mass balance, U_p in block (1,1), is achieved by constructing discrete vector divergence terms from the local gradients for displacement. For additional details, we refer to Berge et al. (2019); Keilegavlen and Nordbotten (2017); Nordbotten (2015); Nordbotten and Keilegavlen (2020).

We note that in the mixed-dimensional setting, the discretization approach is adjusted according to the dimension of the subdomain. This means that Darcy fluxes in all dimensions are discretized using the MPFA scheme, adjusted for the local dimension of the subdomain. Adjacent higher- and lower-dimensional grids are coupled with discrete equivalents of the interface fluxes, Eqns. 4.28, 4.31. We use matching grids in our model, which means that the various projection operators Π_h^j, Ξ_h^j between faces of Ω_h and cells of Γ, and Π_l^j, Ξ_l^j between cells of Ω_l and Γ_j are bijective mappings, so that projection of variables are straightforward (Stefansson et al., 2020b).

Non-linear terms from the contact mechanics are discretized in each fracture cell, assembled in the global system, then solved iteratively in a Newton scheme as described below. Shear-induced dilation is directly coupled to the contact problem, which means that other discretizations that depend on the aperture, such as MPFA in fractures, need to be updated before every Newton iteration. For certain parameter combinations, such as those used for the GTS simulation, the ratio between the largest and smallest terms in the linear system that is solved in every Newton step was very large ($> 10^{15}$). We mitigated this issue by scaling all equations (see Section 4.8), which resulted in ratios $\sim 10^6$. In certain situations, the solution could spontaneously diverge for unknown reasons. In these cases, we restarted the time step to achieve convergence.

5.5 Contact problem discretization

The contact problem (see Eqns. 4.32, 4.35) is solved using a semi-smooth Newton method. We use the method described by Berge et al. (2019) and references therein. The discretization is posed in each cell $\omega_k \in \mathcal{T}$ of the 2D fracture Ω_l. We seek admissible solutions $([u_j], \sigma')$ in each ω_k. Recall $[u_j]$ is the displacement jump, computed as $[u_j] = \Xi_l^j (u_j^+ - u_j^-)$, and σ' is the effective contact pressure in the fracture. Throughout this section, these variables, and other parameters, refer to the discrete quantity within each cell $\omega_k \in \mathcal{T}$. In this context, we also disregard the subscript j for the displacement in order to minimize notation.

The idea is to reformulate the inequality constraints of the contact conditions and the friction law in terms of a non-linear complementary vector-valued function, which we decompose to a tangential and normal part. The tangential complementary function, denoted $C_\tau([\delta u]_\tau, \sigma'_\tau)$ contains the information from the friction law, while the normal complementary function, denoted $C_n([u]_n, \sigma'_n)$ contains the information from the non-penetration condition. These functions are posed so that, for a cell ω_k, the pair $([u], \sigma')$ is admissible provided that $C_\tau([u]_\tau, \sigma'_\tau) = 0$ and $C_n([u]_n, \sigma'_n) = 0$. A semi-smooth Newton method is applied to this problem, which leads to an active set method. The cells are classified as sliding, sticking or not in contact. This classification imposes certain constraints on $[u]$ and σ' in ω_k for the next Newton step.

5.5.1 Discrete formulation

The discrete formulation of the non-penetration condition (see Eqn. 4.32) reads

$$\begin{cases} [u]_n - \mathfrak{G} \geq 0 \\ \sigma_n'([u]_n - \mathfrak{G}) = 0\,, \qquad \omega_k \in \mathcal{T} \\ \sigma_n' \leq 0 \end{cases} \tag{5.14}$$

and the Coulomb friction law (see Eqn. 4.35)

$$\begin{cases} \|\sigma_\tau'\| \leq \mathfrak{F}|\sigma_n'| \\ \|\sigma_\tau'\| < \mathfrak{F}|\sigma_n'| \rightarrow [\delta u]_\tau = 0 \\ \|\sigma_\tau'\| = \mathfrak{F}|\sigma_n'| \rightarrow \exists \mathfrak{C} \geq 0 :\; \sigma_\tau' = -\mathfrak{C}[\delta u]_\tau \end{cases} , \qquad \omega_k \in \mathcal{T}. \tag{5.15}$$

Recall that $\mathfrak{F}$ is the coefficient of friction, which is understood to be cell-wise (i.e. $\mathfrak{F}_k$), and $[\delta u]$ is the temporal increment of $[u]$. For time-dependent problems, this increment is the difference between the current Newton step and the displacement jump from the previous time step. In the static case, the displacement $[u]_\tau$ replaces the sliding velocity $[\delta u]_\tau$.

5.5.2 Semi-smooth Newton method

We define

$$\begin{aligned} b^k = &\quad \mathfrak{F}\left(-\sigma_n'^k - c_n\big([u]_n^k - \mathfrak{G}\big)\right) \\ b_{\geq 0}^k = &\quad \max\{0, b^k\}. \end{aligned} \tag{5.16}$$

The friction bound for the current iteration is $b_{\geq 0}^k$. The friction bound is set to zero if negative values of b^k are encountered during iterations. Due to the non-penetration condition, only one of $\sigma_n'^k$ and $[u]_n^k - \mathfrak{G}$ will be nonzero. In Eqn. 5.16, $c_n > 0$ $\left(\mathrm{Pa\ m^{-1}}\right)$ is a numerical parameter, and $\max\{\cdot,\cdot\}$ returns the maximum of its two arguments.

The complementary function for the non-penetration condition (Eqn. 5.14) is written as

$$C_n([u]_n, \sigma_n') = -\sigma_n' - \frac{b_{\geq 0}^k}{\mathfrak{F}}. \tag{5.17}$$

The Coulomb contact conditions (Eqn. 5.15) are written in terms of the complementary vector-valued function

$$C_\tau([\delta u]_\tau, \sigma_\tau') = -\sigma_\tau' \max\{b^k, \|-\sigma_\tau' + c_\tau[\delta u]_\tau\|\} - b_{\geq 0}^k(-\sigma_\tau + c[\delta u]_\tau) \tag{5.18}$$

where $c_\tau > 0$ is a numerical parameter usually taken to be identical to c_n. Admissible solutions for $([u], \sigma')$ satisfy (Hüeber, 2008; Hüeber et al., 2008)

$$C_n([u]_n, \sigma_n') = 0 \tag{5.19}$$

$$C_\tau([u]_\tau, \sigma'_\tau) = 0. \tag{5.20}$$

5.5.3 Active set formulation

The complementary functions are *semi-smooth* and hence slantly differentiable functions, which allow for the computation of the so-called *generalized Jacobian* (see Hüeber (2008); Hüeber et al. (2008) and references therein). The next semi-smooth step is computed as the solution of a linear system constructed using the generalized Jacobian and complementary functions. This system separates the cells $\omega_k \in \mathcal{T}$ into the inactive sets $\mathcal{J}_\tau^{k+1}$, $\mathcal{J}_n^{k+1}$ and the active set $\mathcal{A}_\tau^{k+1}$, which are computed with respect to the current solution $\left([u]^k, \sigma'^k\right)$.

In the following, we will denote regular inner products with $\langle\cdot,\cdot\rangle : \mathbb{R}^n \times \mathbb{R}^n \to \mathbb{R}$, i.e. $\langle a, b\rangle = \sum_i a_i b_i$.

Not in contact

The set of cells that are not in contact for the next iteration satisfy

$$\mathcal{J}_n^{k+1} = \{\omega_k \in \mathcal{T} : b^k \leq 0\}. \tag{5.21}$$

For these cells, we enforce zero contact pressure homogenous Neumann condition

$$\sigma'^{k+1} = 0, \qquad \omega_k \in \mathcal{J}_n^{k+1}. \tag{5.22}$$

In contact and sticking

The set of cells in contact and sticking satisfy

$$\mathcal{J}_\tau^{k+1} \coloneqq \left\{\omega_k \in \mathcal{T} : \left\|-\sigma_\tau^k + c[\delta u]_\tau^k\right\| - b^k < 0\right\}. \tag{5.23}$$

In the normal direction, we account for the dilation of the cell (Stefansson et al., 2020b). Recall Eqn. 4.33 for the normal gap $\mathfrak{G} : \mathbb{R}^n \to \mathbb{R}$. In the discrete setting, we have

$$\mathfrak{G}^k([u]_\tau) = \mathfrak{G}_0 + \tan(\theta)\left\|[u]_\tau^k\right\|, \qquad \omega_k \in \mathcal{T} \tag{5.24}$$

To satisfy the formulation of the semi-smooth method, Eqn. 5.20, we compute the derivative $D_{\mathfrak{G}}^k$ of $\mathfrak{G}^k$ with respect to the tangential displacement jump $[u]_\tau^k$,

$$D_{\mathfrak{G}}^k = \begin{cases} \tan(\theta)\dfrac{[u]_\tau^k}{\left\|[u]_\tau^k\right\|} & \text{if } \left\|[u]_\tau^k\right\| > 0 \\ \vec{0} & \text{if } \left\|[u]_\tau^k\right\| = 0 \end{cases} \tag{5.25}$$

where $\vec{0} \in \mathbb{R}^2$ is a vector of zeros. The derivative at $\left\|[u]_\tau^k\right\| = 0$ is the continuation of the Jacobian, which we set to zero. We will only use overhead arrows to signify vectors if they unambiguously refer to a vector containing the given symbol in all rows.

The normal displacement jump in the next iteration accounts for the expansion of the normal gap due to dilation from the previous to the current iteration,

$$[u]_n^{k+1} = \mathfrak{G}^k + \langle D_{\mathfrak{G}}^k, [u]_\tau^{k+1} - [u]_\tau^k \rangle.$$

In terms of the new iteration, we have

$$[u]_n^{k+1} - \langle D_{\mathfrak{G}}^k, [u]_\tau^{k+1} \rangle = \mathfrak{G}^k - \langle (D_{\mathfrak{G}}^k), [u]_\tau^k \rangle, \qquad \omega_k \in \mathcal{I}_\tau^{k+1}. \tag{5.26}$$

In the tangential direction we set a Robin condition

$$[\delta u]_\tau^{k+1} - \frac{\mathfrak{F}[\delta u]_\tau^k}{b_{\geq 0}^k} \sigma_n'^{k+1} = [\delta u]_\tau^k, \qquad \omega_k \in \mathcal{I}_\tau^{k+1}. \tag{5.27}$$

If the previous state had zero tangential velocity, the tangential direction reduces to a homogenous Dirichlet condition. In contrast, if the previous state was sliding, we enforce the full Robin condition.

Note that Eqn. 5.26 contains a term for the tangential displacement in the next iteration, whereas Eqn. 5.27 is posed in terms of the sliding velocity. Upon constructing the full boundary condition, we note that for the new iteration $(k+1)$, which in the transient case estimates the new time step $(m+1)$, the sliding velocity is defined as

$$[\delta u]_\tau^{m+1,k+1} = [u]_\tau^{m+1,k+1} - [u]_\tau^{m,} \tag{5.28}$$

where $[u]_\tau^{m,}$ simply refers to the converged solution from the previous time step. Then,

$$\begin{pmatrix} I_l & \vec{0} \\ \left(-D_{\mathfrak{G}}^k\right)^T & 1 \end{pmatrix} \begin{pmatrix} [u]_\tau^{k+1} \\ [u]_n^{k+1} \end{pmatrix} + \begin{pmatrix} \overleftrightarrow{0}_l & \dfrac{\mathfrak{F}[\delta u]_\tau^k}{b_{\geq 0}^k} \\ \vec{0}^T & 0 \end{pmatrix} \begin{pmatrix} \sigma_\tau'^{k+1} \\ \sigma_n'^{k+1} \end{pmatrix} = \begin{pmatrix} [\delta u]_\tau^k + [u]_\tau^{m,} \\ \mathfrak{G}^k - D_{\mathfrak{G}}^k [u]_\tau^k \end{pmatrix}, \qquad \omega_k \in \mathcal{I}_\tau^{k+1} \tag{5.29}$$

where I_l and $\overleftrightarrow{0}_l$ are an identity matrix and a matrix of zeros, respectively, with size equal to the dimension of Ω_l.

In contact and sliding

The set of cells in contact and sliding satisfy

$$\mathcal{A}^{k+1} \coloneqq \{\omega_k \in \mathcal{T} : \|-\sigma_\tau^k + c_\tau [\delta u]_\tau^k\| \geq b^k > 0\}. \tag{5.30}$$

In the normal direction, we account for the expansion of the cell, as outlined in Eqn. 5.24 – 5.26. That is,

$$[u]_n^{k+1} - \langle D_{\mathfrak{G}}^k, [u]_\tau^{k+1} \rangle = \mathfrak{G}^k - \langle D_{\mathfrak{G}}^k, [u]_\tau^k \rangle, \qquad \omega_k \in \mathcal{A}^{k+1}. \tag{5.31}$$

In the tangential direction we estimate the sliding direction and distance,

$$\sigma_\tau'^{k+1} + \tilde{L}^k [\delta u]_\tau^{k+1} + \mathfrak{F} v^k \sigma_n'^{k+1} = r^k + b^k v^k, \qquad \omega_k \in \mathcal{A}^{k+1} \tag{5.32}$$

where $\tilde{L}^k \in \mathbb{R}^n \times \mathbb{R}^n$, $v^k \in \mathbb{R}^n$, and $r^k \in \mathbb{R}^n$, which can be computed from the previous iterate. These functions are regularized in order to mitigate an issue where the exact form of $\tilde{L}^k$ is not guaranteed to be positive-definite during iterations despite being so in the converged limit. Details of the functions and regularization approach can be found in Berge et al. (2019); Wohlmuth (2011).

Like the case for contact and sticking, the next iteration for the normal and tangential conditions both depend on the tangential displacement $[u]_\tau^{k+1}$ due to the dilation term. The formulations can be combined in a similar way as with the full sticking conditions, Eqn. 5.29.

6 Numerical simulation of an in-situ stimulation experiment at the Grimsel Test Site, Switzerland

This chapter concerns the numerical simulation of a hydraulic shearing experiment conducted as part of the In-situ Stimulation and Circulation (ISC) experiment at the Grimsel Test Site (GTS) in the Central Swiss Alps. The tunnel system is located approximately 450 meters below the surface and encapsulates the decameter size rock volume in which five major shear zones have been identified. A series of hydraulic shearing (HS) and hydraulic fracturing (HF) experiments were conducted in the intact rock mass and shear zones in 2017. The HS experiments aimed to enhance the transmissivity of the shear zones. The HS1 experiment was conducted on February 15, 2017, in one of the ductile shear zones. Transmissivity enhancement and slip dislocation were observed near the injection point, and pressure perturbations were measured in nearby boreholes. We have used data from geological, hydraulic, and mechanical characterization campaigns of the rock mass to construct a model for numerical simulation. To avoid over-parameterizing the system state, we simplified the shear zone geometry, hydraulic, and mechanical parameters. Perturbations to the shear zone geometry and background permeability were investigated and compared to the observed pressure profile, transmissivity enhancement, and cumulative slip.

The subsequent sections are structured as follows. Section 6.1 describes the geological and hydro-mechanical characterization studies conducted in the rock mass. Section 6.2 provides an overview of the setup and observations from the HS1 experiment. In Section 6.3 and Section 6.4 we describe the model geometry and model parameters, respectively. Simulation results are presented and discussed in Section 6.5.

6.1 Geological context and hydro-mechanical rock mass characterization

To model the coupled hydromechanical dynamics of a geothermal reservoir, detailed knowledge of the geological context of the target volume is important. In this section, we aim to give an overview of the rock mass characterization that is relevant to the numerical model. First, we provide a description of the mapped shear zones, and a conceptual model of shear zone geometry and extent from geological mapping of the volume. Then, we bring this model into context with the hydraulic and mechanical characterization of the shear zones and overall rock mass.

6.1.1 Shear zone characterization

Characterization of the rock mass uncovered many types of structures including persistent foliations, brittle fractures, and ductile and brittle-ductile shear zones. The shear zones have significant hydraulic and mechanical impact on the rock mass (see Chapter 2). Krietsch et al. (2018a) presented a comprehensive dataset used to provide a complete understanding of the shear zones located in the decameter scale test volume. Two tunnels, termed AU and VE, bound the volume in the east-west direction, in which five major shear zones were identified. A total of 15 boreholes were used to map out shear zone locations and orientations throughout the ISC test volume. An overview of the boreholes in the ISC test volume is provided in Table 6.1. In Figure 6.1 we provide an overview of the GTS laboratory, including the ISC experimental volume with boreholes.

Table 6.1 Overview of boreholes in the test volume. Adapted from Table 2 of Krietsch et al. (2018a).

Borehole Type	Count	Borehole Lengths [m]	Main Purpose
INJ	2	44.66 – 44.80	injection rate and pressure monitoring
FBS	3	44.00 – 47.58	Strain monitoring
GEO	4	30.10 – 40.09	Seismic monitoring
PRP	3	32.33 – 47.91	Pressure and strain monitoring
SBH	3	18.20 – 23.90	Stress measurement

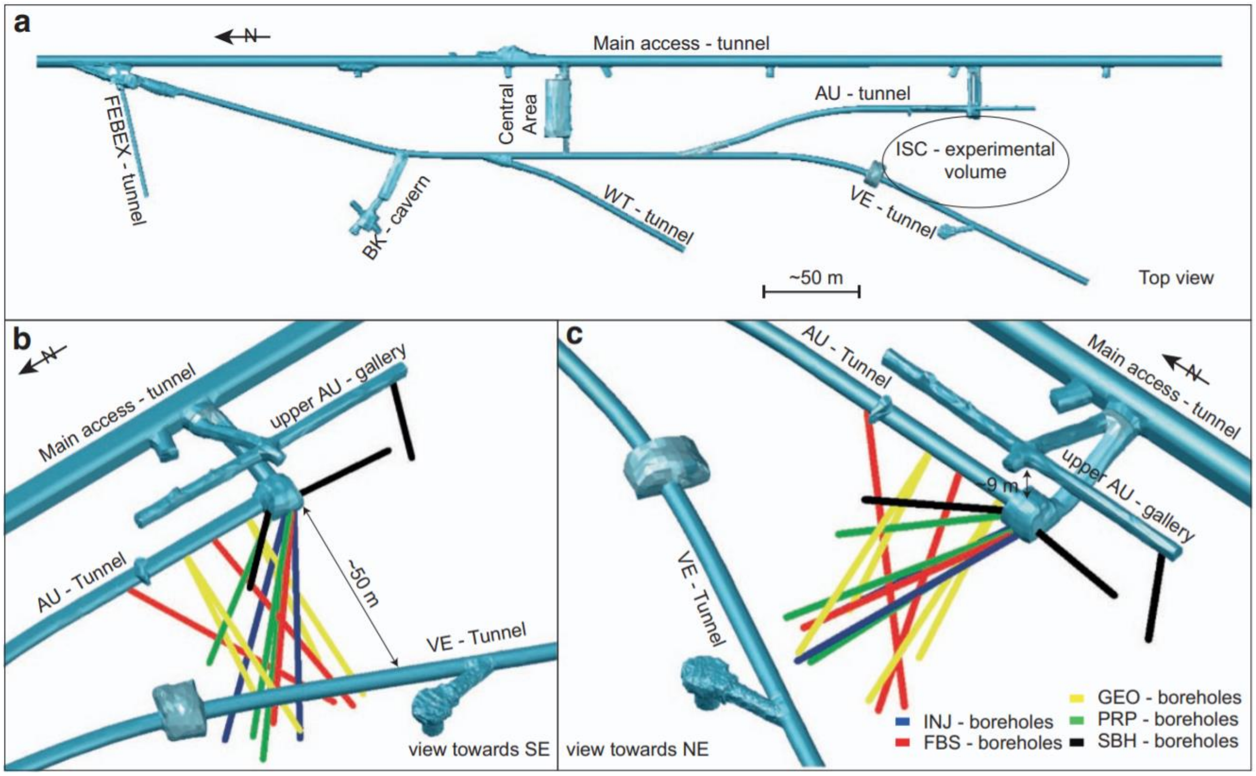

Figure 6.1 Overview of the GTS underground laboratory (a). The ISC experimental volume is located in the southern end of GTS, with boreholes included in (b) and (c). Figure from Krietsch et al. (2018a).

The shear zones are divided into two sets (S1 and S3) with respect to age and orientation. Three ductile shear zones (S1) (strike N52°E, dip 77°SE) are sub-parallel to a persistent foliation and branching off from the set are partly filled brittle fractures. Two parallel brittle-ductile shear zones (S3) (strike N93°E, dip $65°\mathrm{S}$) bound a highly fractured zone (>20 fractures / meter). The S3 shear zones are 2-3 meters apart and approximately $\sim 100\ \mathrm{ml/min}$ discharge is measured between the two shear zones. The shear zones vary greatly in damage zone thickness, ranging $173\ \mathrm{mm}$ to $1670\ \mathrm{mm}$ for the S1 set, and $38\ \mathrm{mm}$ to $312\ \mathrm{mm}$ for the S2 set (Krietsch et al., 2018a).

Based on observations of the location and orientation of shear zones in the boreholes and tunnels, Krietsch et al. (2018a) proposed two conceptual models for the shear zone geometry. The simplified model (Figure 6.2, left) consists of planar patches interpolated from observations. The final model (Figure 6.2, right) fitted the observations using a third-order polynomial, and constrained the orientations of the resulting shear zones near borehole and tunnel observations. Both models disregard data on shear zone thickness.

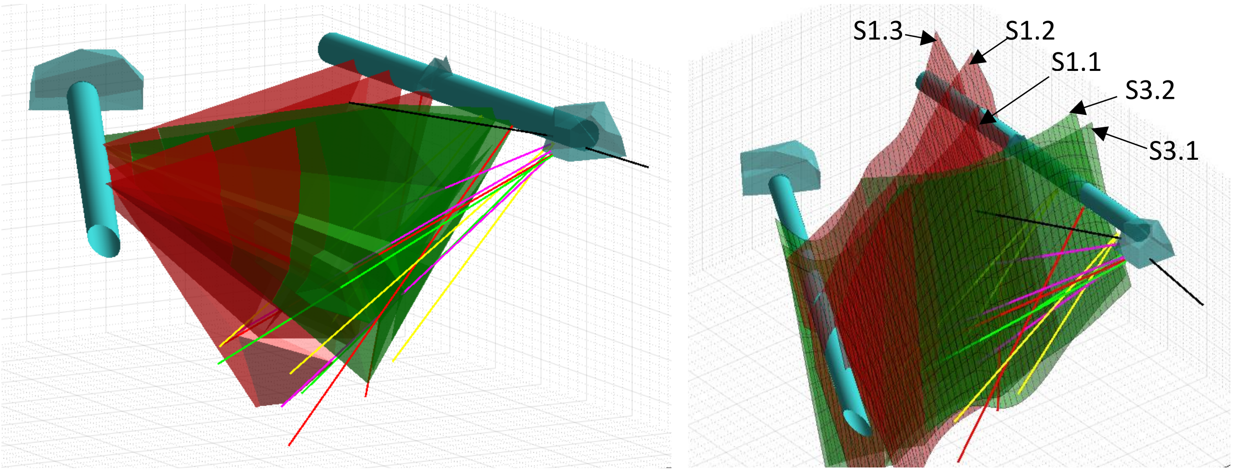

Figure 6.2 Visualization of the geological model based on (left) a simplified model where the shearzone is modeled using piecewise planar patches from shear zone intersections with boreholes and tunnels, and (right) a best-fit third-order polynomial using shear zone intersections and orientations with tunnels and boreholes. The figure is constructed using the Matlab visualization tool from Krietsch et al. (2018a).

As can be seen in Figure 6.2, the shear zones intersect both tunnels. The tunnels, which are at atmospheric pressure, act to relieve pressure from the shear zones. The unperturbed pressure in the shear zones are less than $0.5\ \mathrm{MPa}$ (Jalali et al., 2018), significantly lower than the hydrostatic pressure at $480\ \mathrm{m}$, which is $\sim 4.8\ \mathrm{MPa}$.

6.1.2 Hydraulic characterization

The hydraulic conditions at the Grimsel site are highly heterogenous and anisotropic along the directions normal and parallel to the foliations. The initial hydraulic characterization of the background rock and target shear zones must be assumed to be scale dependent, and likely only accurate in a region near the measurement points. Furthermore, the hydraulic structure of the shear zones evolve due to slip dislocation following the injection experiments. For these reasons, the true hydraulic conditions before the HS1 experiment are uncertain.

Jalali et al. (2018) applied a multi-scale approach to estimate the connectivity and conductivity of the major and persistent structures throughout the volume prior to the hydraulic stimulation experiments.

A double-packer system was installed at varying depths and intervals in the $45\ \mathrm{m}$ deep INJ boreholes to measure interval transmissivity. The results from these measurements are dependent on the interval length but may nonetheless give a reasonable estimate for the hydraulic parameters near the test intervals. Both pulse injection (PI) and constant head injection (CHI) tests were conducted. The PI tests are single-hole, with an interval length of $2-4\ \mathrm{m}$, and give an indication of the depth and location of conductive fractures in the volume, but are restricted in that the data only represents the conditions near the borehole. The CHI tests are cross-hole with an interval length of $0.52\ \mathrm{m}$, and typically targeted individual fractures and shear zones. These tests expanded the measurement scale to $\sim 10\ \mathrm{m}$. Table 6.2 lists the recorded transmissivity for various intervals, depths and boreholes in the test volume, compiled from (Jalali et al., 2018).

Table 6.2 Summary of Hydraulic Measurements in the INJ and SBH boreholes. The Constant Head Injection (CHI) experiments has an interval length of $0.52\ \mathrm{m}$. The Pulse Injection (PI) tests has an interval length of $2\ \mathrm{m}$. The starting point of each interval is reported as depth. Data from Jalali et al. (2018).

Borehole	**Label**	**Depth [m]**	**Transmissivity $[\mathrm{m}^2/\mathrm{s}]$**	**Location / Shear zone**
INJ2	PI.1	39	1E-10	S1.3
	PI.8	32	1E-09	S1.2
	PI.9	29	5E-08	S1.1
	CHI#1	28.53	6.1E-10	Near S1.1
	CHI#2	27.11	3.7E-08	Near S3.2
	CHI#3	26.25	3.7E-09	S3.2
	CHI#4	24.83	1.8E-08	S3.2
	CHI#5	24.31	1.8E-08	Near S3.2
	CHI#6	23.38	3.9E-07	Between S3.1 and S3.2
	CHI#7	22.89	4.0E-06	Between S3.1 and S3.2
	CHI#8	21.96	6.1E-07	Between S3.1 and S3.2
INJ1	CHI#9	21.96	6.1E-07	S3.2
	CHI#10	31.64	2.6E-10	S3.2
	CHI#11	28.58	1.8E-09	Near S3.1
	CHI#12	27.67	3.7E-07	S3.1
	CHI#13	27.16	2.3E-08	Near S3.1
	HF5	11.5	5.9E-13	--
	HF6	15.9	5.1E-12	--
	HF7	17.8	3.1E-12	--
	HTPF	19.8	3.8E-12	S3.1

The transmissivity data shows that the fractured zone between the two S3 shear zones is highly conductive compared to the overall granitic rock. The highest recorded transmissivity values correspond to CHI#7 and CHI#12 tests. However, these results are also influenced by the presence of the excavated tunnels as significant flow rates were observed in the tunnels during these tests. Wenning et al. (2018) measured the permeability in core samples throughout the SBH4 borehole, a 23.90 m long borehole drilled sub-horizontally from the AU tunnel towards $\sim 320°$, intersecting the mylonitic cores of the S3 structure (i.e. S3.1 and S3.2). The mylonitic cores are regions of reduced permeability and increased anisotropy. Permeability in the direction normal to the mylonitic cores is an order of magnitude smaller than the foliation-parallel permeability, measured at $0.03 \times 10^{-19}\ \mathrm{m}^2$ and $0.57 \times 10^{-19}\ \mathrm{m}^2$, respectively. The anisotropy can be explained by changes in mineralogy as the cores are approached.

Additional constant rate cross-hole pressure tests between the two S3 shear zones indicate heterogeneity in the fractures since pressure responses from fluid injected in one borehole is different from the case where fluid is injected in the other borehole (Jalali et al., 2018). This may also indicate that fluid flows naturally in one direction rather than the other. Overall, the highly fractured zone between the S3.1 and S3.2 shear zones plays a key role in the fluid flow and mechanical deformation. Fluid injected near the fractured zone is expected to trace few conductive fractures, as opposed to fluid injection away from the two S3 shear zones, which may be characterized by more intricate flow through a fracture network (Jalali et al., 2018).

For comparison, the permeability measured in the intact rock was found to be ranging $0.99 \text{ to } 8.38 \times 10^{-19}\ \mathrm{m}^2$ (Wenning et al., 2018). For in-situ water at $11\ °C$, this roughly equates to a hydraulic conductivity (i.e. the transmissivity through a unit width of rock) of $0.77 \text{ to } 6.50 \times 10^{-12}\ \mathrm{m/s}$. Brixel et al. (2020) found similar results using single-hole measurements in situ, with values ranging $10^{-21} \text{ to } 10^{-18}\ \mathrm{m}^2$ (i.e. $10^{-14} \text{ to } 10^{-11}\ \mathrm{m/s}$).

6.1.3 Mechanical characterization

Numerous characterization campaigns have been conducted at the Grimsel Test Site to determine the rock mechanical properties of the Grimsel granite (e.g. Krietsch et al. (2018b); Nejati (2018); Pahl et al. (1989)). In some cases, the measurements from different studies can vary appreciably. This can be due to different measurement techniques, equipment sensitivity, data interpretation, test location, or local host rock properties. For these reasons, it can be challenging to assess which parameters to use in simulations. Furthermore, Nejati (2018) argued the Grimsel granite exhibits substantial anisotropic properties due to the presence of foliations.

Krietsch et al. (2018b) conducted an extensive stress characterization survey on the ISC rock mass to characterize the in-situ stress field and elastic parameters (see also Gischig et al. (2018)). Two main methods were used, stress relief and hydraulic methods, that each highlight important and useful information for modeling and interpreting deformation response due to fluid injection in fractured subsurface reservoirs. The hydraulic methods are suitable to estimate the least principal stress direction and magnitude by inducing hydraulic fractures (HF). Additionally, hydraulic testing on pre-existing fractures (HTPF) can provide an estimate for the normal stress acting on the fractures. Stress relief methods provide estimates for the linear elastic parameters such as Young's modulus, shear modulus and Poisson's ratio, and the full stress tensor by inverting for the strain using the estimated parameters.

Stress relief methods measures the elastic response of the rock assuming the rock is linearly elastic throughout the test. Testing was conducted both near the shear zones and away from them, enabling estimation of the far-field stress in addition to the stress perturbation near the shear zones. The idea of estimating both the unperturbed (far-field) and perturbed (near shear zones) stress is motivated in part by the observation of significant rotation of the stress near the shear zones. At the Soultz-sous-Forêts site in France for example, the maximum horizontal stress was found to rotate up to 90° near major shear zones. This effect can significantly alter the elastic response of the rock mass due to fluid injection (Valley & Evans, 2010).

Additionally, two separate hypotheses for the rock mass were investigated: (1) assuming an isotropic elastic rock model, and (2) assuming a transversely isotropic rock model. The latter model predicts elastic parameters that are different in the vertical direction compared to the horizontal directions, and therefore lead to two Young moduli and Poisson's ratios, and an independent cross-shear modulus. With certain assumptions on the degree of anisotropy within the rock mass, the model can be constrained. Additional accuracy was obtained by integrating the HF test results, described below. The principal stress obtained from inverting for strains assuming a transversely isotropic model, with additional constraints informed by HF tests, are on average $13.1\ \mathrm{MPa}$ for σ_1 $(104.48/39.21$, i.e. dip direction/dip), $9.2\ \mathrm{MPa}$ for σ_2 $(259.05/47.90)$, and $8.7\ \mathrm{MPa}$ for σ_3 $(003.72/12.89)$. Additional information on representation of the stress in a Euclidean coordinate system can be found in Appendix 8.2.

Hydraulic fracture (HF) tests were conducted in locations away from natural fractures. These tests estimate the least principal stress direction and magnitude by initiating and propagating hydraulic fractures through multiple injection cycles. The instantaneous shut-in pressure (ISIP) is the pressure that is measured as the final injection cycle is completed, and is used as an estimate of the minimum principal stress (σ_3) (McLennan & Roegiers, 1982). The direction of the stress component is inferred from the plane along which the hydraulic fracture propagates (i.e. normal to σ_3). Two boreholes, SBH1 and SBH3, were used to estimate σ_3 in unperturbed rock (see Figure 6.3). SBH1 is steeply plunging (75°) and SBH3 is sub-horizontal ($-5°$). The results from the HF tests are considered ground truth, and since the magnitude of the measured stress never exceeded $9.7\ \mathrm{MPa}$, the full stress tensor could be further constrained.

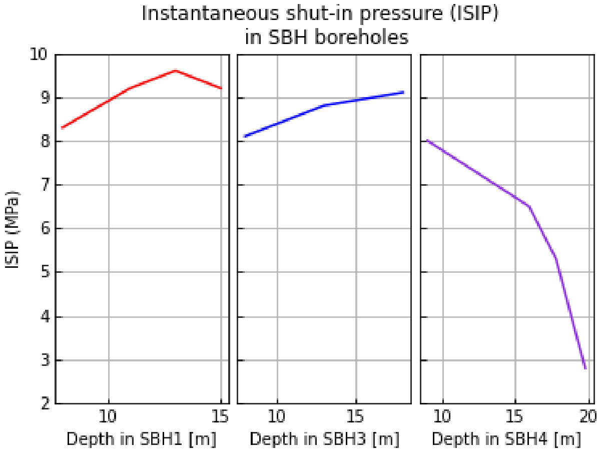

Figure 6.3: Instantaneous shut-in pressure results from two HF tests (SBH1, SBH3) and one HTPF test (SBH4). There is a decrease in ISIP as the S3 shear zone is approached in SBH4 at 19.7 m depth. The unperturbed rock has small variations in ISIP throughout SBH1 and SBH3. Data from (Krietsch et al., 2018b).

Hydraulic testing of pre-existing fractures (HTPF) was conducted in the SBH4, a sub-horizontal ($-5°$) borehole that intersects the S3 shear zone at $20\ \mathrm{m}$. The lowest stress value of $2.8\ \mathrm{MPa}$ was recorded at $19.8\ \mathrm{m}$ depth in SBH4, which is likely to have been affected by the nearby fractured zone. Since the stimulated fracture is not necessarily oriented normal to the minimum principal stress, $\sigma_3 = 2.8\ \mathrm{MPa}$ should be considered an upper bound for the true value of σ_3 in this region. The perturbed stress tensor was estimated from the stress measurements conducted near the shear zones.

Coupled hydromechanical processes in porous media are sensitive to the Biot coefficient (Berre et al., 2020). The Biot coefficient emerges from the constitutive relation in poroelasticity where the total stress tensor is assumed to consist of the stresses of the porous skeleton, and the stresses of the pore fluid. By considering the skeletal bulk modulus (K_D) and the bulk modulus of the solid material composing the rock fabric (K_S), the isotropic Biot coefficient for an elastic medium is computed as $\alpha = 1 - (K_D/K_S)$. Selvadurai et al. (2019) analyzed estimates of the elastic constants from previous studies at the Grimsel Test Site. The skeletal bulk modulus can be computed from Young's modulus and Poisson ratio in isotropic or transversely isotropic conditions. The effective bulk modulus for the Grimsel granite was estimated by considering the mineralogical fractions of the Grimsel granite. The highly heterogenous rock mass at the Grimsel Test Site means that some measurements of elastic constants may result in unrealistic estimates for the bulk moduli. By excluding these results, a set of realistic estimates for the Biot coefficient were determined. Assuming an isotropic elastic medium, the Biot coefficient ranges from 0.48 to 0.64 depending on which measurements are considered. The skeletal bulk modulus ranged from $24\ \mathrm{GPa}$ to $27\ \mathrm{GPa}$. In the transversely isotropic case, the lower and upper estimates for the Biot coefficient were 0.64 to 0.71, and skeletal bulk modulus approximately $19\ \mathrm{GPa}$. A summary of these parameters is listed in Table 6.3.

Table 6.3 Elastic properties of the Grimsel granite, including Young's modulus (E), Poisson's ratio (ν), skeletal bulk modulus (K_D), and the Biot coefficient (α) for a transverse isotropic elastic rock model, and an isotropic elastic rock model. For the transversely isotropic model, the subscript T refers to directions along foliations, while the subscript N refers to directions normal to the foliations. The data for the Biot coefficient is from Selvadurai et al. (2019). The other data is from the respective references as listed in the first row.

Reference	Pahl et al. (1989)	Bouffier (2015)	Dambly et al. (2019)	Nejati (2018); Nejati et al. (2019)
Elasticity type	Isotropic	Isotropic	Isotropic	Transversely isotropic
Young modulus, $E\ [GPa]$	40	26	44	$E_N \approx 13$ $E_T \approx 25$
Poisson's ratio, $\nu\ [-]$	0.25	0.33	0.2	$\nu_{TT} \approx 0.15$ $\nu_{NT} \approx 0.15$
Skeletal bulk modulus $K_D\ [GPa]$	~ 27	~ 25	~ 24	~ 19
Biot coefficient, $\alpha\ [-]$	$0.48 - 0.59$	$0.52 - 0.62$	$0.54 - 0.64$	$0.64 - 0.71$

6.2 Description of HS1 stimulation at 39.75-40.75 m in INJ2 into S1.3

The HS1 stimulation experiment is part of a larger study of six stimulation experiments targeting S1 and S3 shear zones (Krietsch et al., 2020). All six stimulation experiments were conducted using a standardized injection protocol, which allows for comparison of results targeting different shear zones, as results do not depend on the injection methodology. The injection protocol consists of four cycles, C1 to C4, as illustrated for HS1 in Figure 6.4. C1 and C2 are pre-stimulation phases where water is injected in pressure increments to estimate jacking pressure and injectivity of the target shear zone. C3 is the main stimulation phase, which, as initially planned, consisted of stepwise rate increments over the duration of 40 minutes, followed by shut-in for 40 minutes and venting for 20 minutes. The rate increments were planned to be 10, 15, 20 and 25 l/min. Permanent changes to the target shear zone, such as slip and transmissivity enhancement, were estimated at the injection interval during the post-stimulation cycle C3 for each experiment. For all stimulation experiments, a higher-rate injection regime for C3 was considered provided the cumulative volume did not exceed the target maximum of 1000 liters, determined by the seismicity risk (Doetsch et al., 2018; Gischig et al., 2016). For HS1, which targeted the S1.3 shear zone, a high-rate regime was used. The C3 main stimulation cycle for HS1 consisted of five steps, as listed in Table 6.4. The first four steps lasted for approximately five minutes each, starting at $15\ \mathrm{l/min}$, with $5\ \mathrm{l/min}$ increments for subsequent steps. The fifth step, at $35\ \mathrm{l/min}$, lasted for approximately 15 minutes. The injection steps for HS1 were followed by shut-in for approximately 46 minutes and venting for 20 minutes.

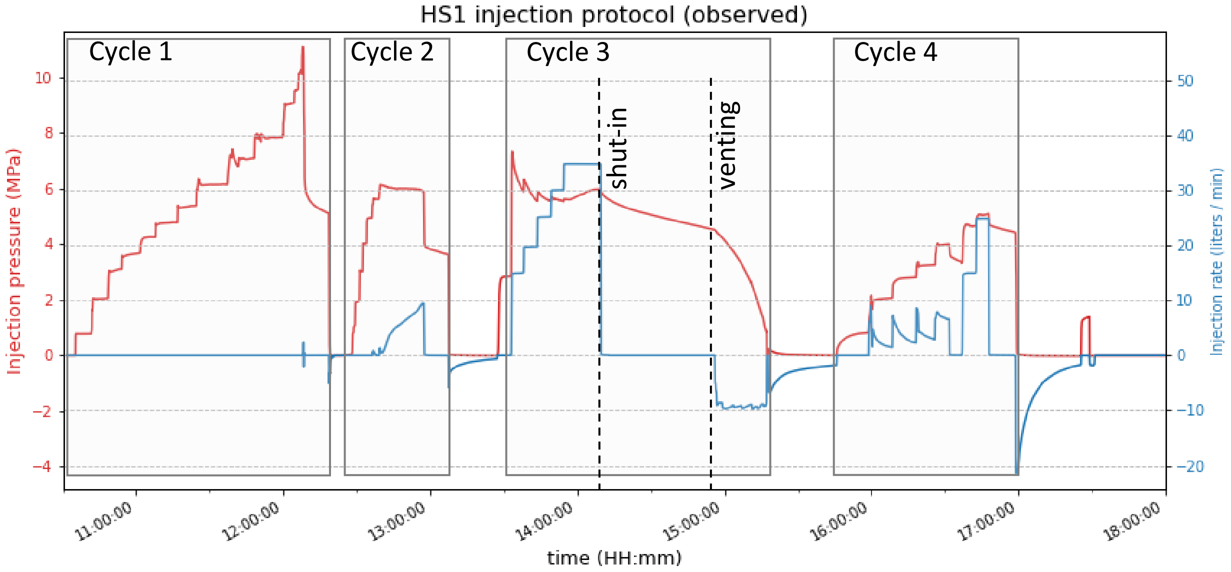

Figure 6.4 Injection protocol for experiment HS1, which targets S1 structure S1.3, with each cycle indicated. Shut-in and venting for cycle 3 are marked by vertical lines. The target shear zone is vented before and after every cycle. Data from Krietsch et al. (2019).

Table 6.4 Injection rate and step duration during C3 main-stimulation phase of HS1. The duration of the five injection steps combined is 36 minutes, 20 seconds. Note that venting is pressure-controlled (the well is to the tunnel, at atmospheric pressure), so no injection rate is not applicable. Data compiled from Krietsch et al. (2019).

Step	Step 1	Step 2	Step 3	Step 4	Step 5	Shut-in	Venting
Injection rate $(\mathrm{l/min})$	15	20	25	30	35	0	$-$
Duration $(\mathrm{mm:ss})$	$04:51$	$05:30$	$05:30$	$05:09$	$15:06$	$46:25$	$20:20$

The six stimulation experiments were conducted sequentially, with at least twelve hours between the end of one experiment until the start of the next. The time between each stimulation experiment allows for most of the induced fluid pressure disturbances to drain out from the system. However, the shear zones may remain stimulated after each experiment, which means that some deviation from the hydromechanical parameters compared to the pre-characterization tests should be expected.

The pre- and post-stimulation phases were intended to characterize the hydraulic changes (jacking pressure and transmissivity) and mechanical changes (cumulative slip). For HS1, fluid was injected to the rock-mass using a double-packer system where fluid injection is restricted to a specific interval in the borehole. An overview of the hydro shearing (HS) experiment HS1 is provided in Table 6.5, including target shear zone, interval depth, estimated pre- and post-transmissivity values (estimated from injectivities), and cumulative slip dislocation. Due to rock heterogeneity, the pre- and post-stimulation characterization can conservatively be assumed to only be valid locally near the borehole. The cumulative slip dislocation at the injection interval was estimated to be $0.7-0.81\ \mathrm{mm}$ for HS1. The interval transmissivity increased by more than three orders of magnitude, from $8.3\times10^{-11}\ \mathrm{m^2/s}$ to $1.5\times10^{-7}\ \mathrm{m^2/s}$ (Krietsch et al., 2020). The resulting interval transmissivity for HS1 is comparable to the results from the other HS experiments, despite the pre-stimulation transmissivity for these experiments ranging $10^{-10}\ \mathrm{m^2/s}$ to $10^{-7}\ \mathrm{m^2/s}$.

Table 6.5 Summary of the HS1 stimulation experiment with estimates of pre- and post-stimulation transmissivities. The data is from Table 1 in Krietsch et al. (2020).

	Date	Injection borehole	Interval depth (m)	Structure	Pre-stimulation transmissivity $(\mathrm{m^2/s})$	Post-stimulation transmissivity $(\mathrm{m^2/s})$	Cumulative slip dislocation (mm)
HS1	15.02.2017	INJ2	39.75 - 40.75	S1.3	8.3×10^{-11}	1.5×10^{-7}	0.7 – 0.81

In addition to transmissivity changes and slip dislocation, the surrounding boreholes were also used to monitor interval pressure, seismic events, backflow from boreholes, tilt, and strain. These measurements were used to estimate the extent of propagation of the pressure front, extent of the deformation field (Krietsch et al., 2020), and the seismically activated area (Villiger et al., 2020a).

6.3 Shear zone model geometry from geological context and borehole observations

Mixed-dimensional DFM models are attractive since fractures can be explicitly modeled. However, the computational expense can quickly grow for complex fracture networks. Therefore, a compromise between an accurate representation of the geometry and computational feasibility is sought. For our model of the ISC volume, data on individual fractures were disregarded. Hydraulic parameters are not well constrained in these structures which could lead to over-parameterization of the system, but more importantly, the inclusion of fractures would be a significant challenge to the simulator.

Instead, we only modeled the shear zones. The shear zones are idealized as planar, open fractures. To model the shear zones, we first estimated their orientation, then we constrained their size.

We created a tool in Python that extracts and structures the geospatial data on boreholes, shear zones, and tunnels which is provided by Krietsch et al. (2018a). Then, we computed best-fit planes using the data on shear zone intersections with boreholes. We evaluated both ordinary least squares (OLS) regression and total least squares (TLS) to compute best-fit planes. TLS is a generalization of OLS in that the error is minimized in the direction orthogonal to the regression plane, and has been evaluated on outcrop data of fractures (Jones et al., 2016). OLS on the other hand assumes that some of the geospatial directions are error-free. Testing of both methods on the five shear zones under consideration yielded comparable results. The centroid and orientation of all interpolated shear zones are listed in Table 6.6.

Table 6.6 Coordinates and orientation of the shear zones S1 and S3. The underlying data is from Krietsch et al. (2018a).

	Centroid coordinate			Normal vector coordinate		
Shear zone	x	y	z	x	y	z
S1.1	51.456704	109.806622	20.010900	-0.485314	0.861540	-0.149059
S1.2	47.969502	113.118832	16.959744	-0.496146	0.841186	-0.215046
S1.3	44.821713	117.088891	14.749656	-0.502727	0.813966	-0.291076
S3.1	53.395810	105.063501	22.949580	0.121912	0.940431	-0.317375
S3.2	52.491075	108.564742	21.878384	0.146613	0.942768	-0.299489

Next, we constrained the size of the shear zones. A lower bound on the size of the shear zones are the observations of shear zone intersections in boreholes, which results in a geometry similar the piecewise planar model presented in Krietsch et al. (2018a) (see Figure 6.2, left). However, this model results in low total fluid storage in the shear zones, and since the permeability in the intact rock is low, high pressures within the shear zones would be expected. Larger shear zones provide more storage, and their high transmissivity allow fluid to be quickly diffused far away from the injection point. However, the transmissivity is not well constrained away from the observations, which, depending on the chosen transmissivity values, could lead to unrealistically quick diffusion of the pressure, say, after shut-in. These considerations motivated testing on shear zones of different sizes, as will be explained in Section 6.4.3. The smallest shear zones that were simulated extended at least 10 m beyond the tunnels in the horizontal and spanned the height of the boreholes in the vertical. This was set as the minimum size so that the tunnels could be accounted for, as will be described in Section 6.4.2.

We used gmsh to generate unstructured meshes (Geuzaine & Remacle, 2009). In previous work (e.g. Keilegavlen et al. (2020)), fractures are meshed by explicitly embedding 2D surfaces into the interior of the 3D volume. This approach restricts which algorithms can be used for meshing and mesh optimization. In particular, the Netgen mesh optimizer only supports optimization of 3D volumes, and can therefore not be used for domains with explicitly embedded fractures (Schöberl, 1997). Testing on the ISC shear zones revealed that robust meshing algorithms are needed to achieve convergence.

The shear zones were constructed by inserting a cube into the interior of the domain which was subsequently sliced at locations corresponding to the surfaces of the shear zones. This results in a partition of the domain into 3D volumes, which can be optimized with Netgen. The resulting simulation grid is shown in Figure 6.5. Note that the tunnels are included for visualization purposes and are not explicitly present in the simulation.

We did not include S3.2 in the final model for computational reasons. There were difficulties related to producing high-quality meshes with sufficiently few numbers of cells so that simulations could be run in reasonable time. The issues stem from the short distance $(2 - 3\ \mathrm{m})$ between S3.1 and S3.2. Mechanical and hydraulic parameters are highly heterogeneous and anisotropic in the S3 shear zone, which we are not able to capture irrespective of explicitly modeling one or two mylonitic cores. As such, we collapsed the S3 zone onto the location of the S3.1 mylonitic core.

As can be seen from Figure 6.8 (left), the cells near the shear zones are much smaller than those near the global boundary. We were able to construct the grid with precise control of the characteristic mesh size in the far-field, near the shear zones, near the shear zone intersections, and near the outer edges of the shear zones. The resulting simulation grid consisted of approximately $24\ 000$ cells. Beyond the shear zones, the 3D domain extended at least $100\ \mathrm{m}$ in every direction, with total dimensions of $300 \times 300 \times 300$ meters.

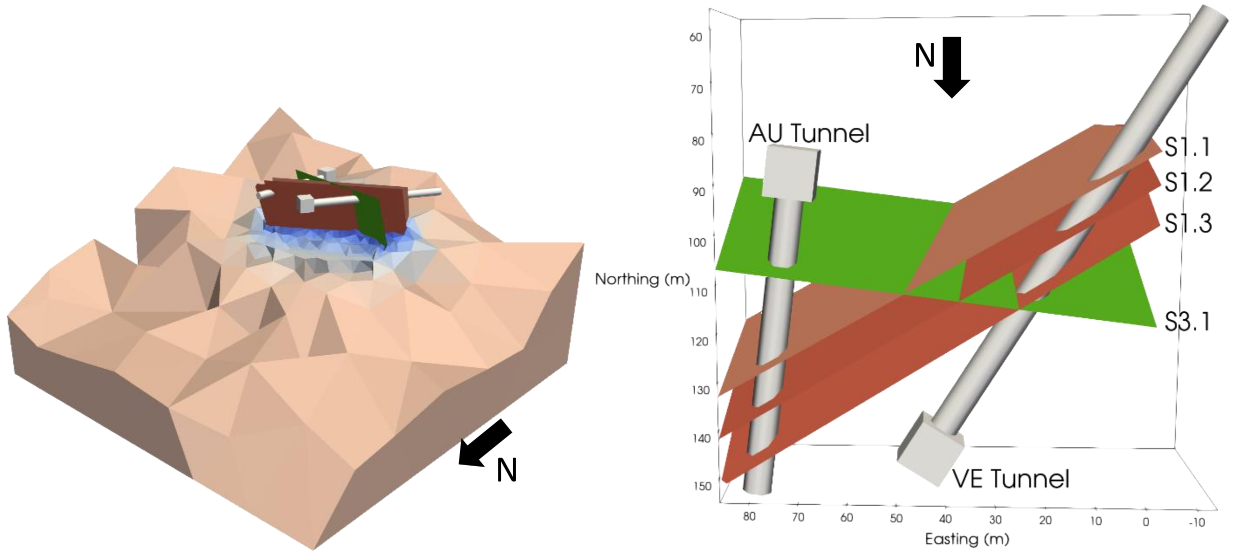

Figure 6.5 Left: The 3D simulation grid, exposing the fractures situated in the 3D volume. Right: The geometric representation of the shear zones in the model, viewed from the top. Tunnels are illustrated, but not explicitly included in the model. ParaView is used for visualization of the simulation grid (Ahrens et al., 2005).

6.4 Model parameters and initial and boundary conditions

This section describes the model parameters, initial conditions, and boundary conditions that are needed to simulate the hydraulic shearing experiment. Then, a description of perturbations to the shear zone geometry and the permeability of the intact rock is provided. These perturbations result in four simulation cases. A succinct summary of the parameters is provided at the end of the section, in Table 6.8, for reference.

6.4.1 Model parameters

An isotropic elastic rock model was used. The elastic coefficients estimated by Pahl et al. (1989) along with the relevant estimate for the Biot coefficient due to Selvadurai et al. (2019) were imposed as constant values throughout the intact rock. The values are provided in the first column of Table 6.3.

A homogenous and isotropic permeability coefficient on the order of $10^{-20}\ \mathrm{m}^2$ was used throughout the intact rock. The value was based on the single-hole measurements by Brixel et al. (2020). The simulation cases, described in Section 6.4.3, supply the exact values for each case.

As noted, homogeneous and isotropic values for permeability and elastic coefficients were chosen despite the presence of foliations that induce transversely isotropic elastic and hydraulic parameters. We opted to ignore this aspect of the parameters. This is motivated by our primary interest in the dynamics occurring within the shear zones. Additionally, since the heterogeneity of the parameters are not well constrained in the hydraulic characterization, we determined that homogeneous transverse isotropic parameters would not improve the interpretability of the results.

Determining representative shear zone transmissivity values are much more challenging for numerous reasons. As indicated by the general description in Section 6.1.1 and the hydraulic characterization in

Section 6.1.2, the shear zones are complex zones, both structurally and hydraulically. The S1 shear zone is characterized as a localized high strain zone with sub-parallel brittle fractures (Wehrens et al., 2017). This indicates that it can be interpreted as a distributed conduit (see Section 2.2.1). In contrast the S3 shear zone can be characterized as a highly fractured conductive zone enclosed by two mylonitic cores. As Table 6.2 shows, the zone between the cores is highly permeable, on the order of $10^{-7} - 10^{-6}\ \mathrm{m}^2/\mathrm{s}$. In contrast, the mylonitic cores are barriers to flow. The S3 zone can therefore be interpreted as a combined conduit-barrier.

Since we modeled the shear zones as planar, open fractures, the conductive fractures surrounding of the S1 shear zone had to be implicitly included in the transmissivities that were enforced. To this end, we used the pulse injection tests listed in Table 6.2, which covered an interval of $2\ \mathrm{m}$, i.e. beyond the S1 shear zone cores. However, for S1.3 specifically, we opted for the transmissivity listed in Table 6.5, which was measured immediately before the main stimulation phase started (Krietsch et al., 2020).

As discussed in the previous section, we opted to collapse the S3 shear zone consisting of the S3.1 and S3.2 mylonitic cores to the location of the S3.1 mylonitic core. As a representative value, the CHI#12 measurement was used (see Table 6.2), which is on the order of the measurements within the highly fractured zone.

For all shear zones, the initial transmissivity was converted to initial aperture using the cubic law, which was subsequently used to calculate specific volumes that would initialize the model parameters. The resulting shear zone aperture after a stimulation experiment

$$a = a_{\mathrm{init}} + a_{\mathrm{dil}} + a_{\mathrm{sep}} \tag{6.1}$$

is controlled by the initial aperture, a_{init}, calculated from the pre-stimulation transmissivity, the aperture due to shear-induced dilatancy, a_{dil}, and the aperture due to the separation of the fracture faces, a_{sep}. Assuming that reactivated fractures close post-stimulation $\left(a_{\mathrm{sep}} = 0\right)$, and that the dilation is calculated from shear slip using the dilation angle, $a_{\mathrm{dil}} = \|[u]_\tau\| \tan\theta$, then we can invert for the dilation angle by rearranging Eqn. 6.1,

$$a = a_{\mathrm{init}} + a_{\mathrm{dil}} = \sqrt[3]{\frac{12\mu T}{\rho g}} + [u]_\tau \tan\theta$$

$$\Longrightarrow \theta = \arctan\left[\sqrt[3]{\frac{12\mu}{\rho g}} \cdot \frac{\sqrt[3]{T} - \sqrt[3]{T_{\mathrm{init}}}}{[u]_\tau}\right] = \arctan\left[1.16 \times 10^{-2} \cdot \frac{\sqrt[3]{T} - \sqrt[3]{T_{\mathrm{init}}}}{[u]_\tau}\right] \tag{6.2}$$

where T_{init} is the initial transmissivity and T is the final transmissivity. Consider for instance HS1, where $T_{\mathrm{init}} = 8.3 \times 10^{-11}\ \mathrm{m}^2/\mathrm{s},\ T = 1.5 \times 10^{-7}\ \mathrm{m}^2/\mathrm{s},\ [u]_\tau = 0.7 \text{ to } 0.81 \times 10^{-3}\ \mathrm{m}$ (see Table 6.5). Using Eqn. 6.2, the dilation angle was estimated to be in the range 4.0° to 4.6°. Since we kept the dilation angle constant irrespective of the amount of total slip, we set the angle slightly lower than the estimated values, to 3°.

6.4.2 Boundary conditions and tunnels

Including gravitational effects in the model led to issues with convergence of the Newton iterations. We have kept Section 4.7 in the thesis for reference, but opted for constant-depth hydrostatic and lithostatic boundary conditions in for the simulation of HS1.

For the stress tensor, we used the measurements from Krietsch et al. (2018b) (see Section 8.2). Setting the stress as a Neumann condition on all external faces does not lead to a consistent system. Therefore, we kept three cells on the bottom center of the domain fixed $(u = 0)$. For hydraulic boundary conditions, we imposed constant pressure equivalent to the hydrostatic pressure at $480\ \mathrm{m}$ depth on the external boundary. We equilibrated the system with these conditions for $30\ 000\ \mathrm{years}$.

The hydraulic effect of the tunnels in the test volume was accounted for by imposing atmospheric pressure in eight shear zone cells, one cell per intersection of the tunnels with the four modeled shear zones. The tunnels were constructed approximately 30 years before the stimulation took place, and as such, we enforced these pressure conditions for 30 years before starting the main stimulation phase. Note that with this approach, the mechanical impact of the tunnels, which are expected to be minor, could be completely ignored.

6.4.3 Construction of the simulation cases

This section describes the setup of four simulation cases for the hydraulic shearing experiment. We considered two different shear zone sizes, and two different values for the intact rock permeability. We chose to vary these parameters since they are not well-constrained in the geological characterization. Therefore, we define option A as the cases where the shear zones are “small”, and option B as the cases where the shear zones are “large” (as detailed below). Likewise, option 1 is defined as the case where a low background permeability is employed, and in option 2 the background permeability is high relative to option 1. Similarly, the case with large shear zones and high background permeability is denoted B2. An overview of the case nomenclature is provided in Table 6.7.

Table 6.7 Overview of naming convention for four numerical simulations of the HS1 experiment.

	Low matrix permeability, 1	High matrix permeability, 2
Small shear zones, A	Case A1	Case A2
Large shear zones, B	Case B1	Case B2

We will now briefly summarize the specific parameter changes. The dimensions of the shear zone bounding box in option A are $[-1,86] \times [80,151] \times [-5,41]$. For option B, the shear zone bounding box are extended by 10 meters towards east ($+x$), 5 meters towards north ($+y$), and 5 meters in each direction in the vertical ($\pm z$), resulting in the dimensions $[-1,96] \times [80,156] \times [-10,46]$. The background permeability for option 1 is $5 \times 10^{-21}\ m^2$, and doubled to $10^{-20}\ m^2$ for option 2.

Table 6.8 Model parameters for the HS1 simulation.

E	Young's modulus	$40\ \mathrm{GPa}$
ν	Poisson's ratio	0.25
K_D	Skeletal bulk modulus	$27\ \mathrm{GPa}$
α	Biot coefficient	0.54
$\mathscr{k}$	Permeability for the intact rock	$10^{-21}\ \mathrm{m}^2$ or $5 \times 10^{-21}\ \mathrm{m}^2$
σ_1	Maximum principal stress	$13.1\ \mathrm{MPa}\ (104.48 / 39.21)$
σ_2	Intermediate principal stress	$9.2\ \mathrm{MPa}\ (259.95 / 47.90)$
σ_3	Minimum principal stress	$8.7\ \mathrm{MPa}\ (003.72 / 12.89)$
ϕ	Porosity	0.7%
ρ_f	Fluid density	$1000\ \mathrm{kg/m}^3$
ρ_m	Rock density	$2700\ \mathrm{kg/m}^3$
$\mathfrak{F}$	Friction coefficient	0.8
c_f	Fluid compressibility	$4 \times 10^{-10}\ \mathrm{Pa}$
μ	Dynamic viscosity	$1.26 \times 10^{-3}\ \mathrm{Pa{\cdot}s}$
θ	Dilation angle	$3°$
T	Initial shear zone transmissivity:	
	- S1.1	$5.0 \times 10^{-8}\ \mathrm{m}^2/\mathrm{s}$
	- S1.2	$1.0 \times 10^{-9}\ \mathrm{m}^2/\mathrm{s}$
	- S1.3	$8.3 \times 10^{-11}\ \mathrm{m}^2/\mathrm{s}$
	- S3.1	$3.7 \times 10^{-7}\ \mathrm{m}^2/\mathrm{s}$
	Characteristic length scale	$1\ \mathrm{m}$
	Characteristic pressure scale	$10^{11}\ \mathrm{Pa}$
	Characteristic time scale	$1\ \mathrm{s}$
	Time step per phase (# of steps):	
	- Initialization of pressure	15 000 years (2)
	- Initialization of tunnels	15 years (2)
	- Stimulation phase	1 to 2.5 min (19 to 22)
	- Shut-in phase	15 min (5)

6.5 Simulation results: HS1 stimulation into S1.3

We aim to present simulations of the HS1 stimulation experiment on February 15th 2017 and compare the results with the estimated transmissivity enhancement, induced slip, and pressure curves as described in Section 6.2. The simulation results are presented by comparing four model simulations corresponding to specific parameter perturbations, as described in the previous section.

6.5.1 Pre-stimulation state

First, we consider the initial pressure profile from the initialization steps. Recall that the system is first equilibrated with respect to the boundary conditions, then, we include the hydraulic effect of the AU and VE tunnels by fixing the pressure in the part of the shear zones that intersect the tunnels to atmospheric pressure ($0.1\ \mathrm{MPa}$). As can be seen in Figure 6.6, the atmospheric pressure profile due to the AU tunnel is clearly discernible. After 30 years of tunnel equilibration, the mean-pressure in S1.3 is $0.2 - 0.3\ \mathrm{MPa}$ for all simulation cases. The peak pressure in S1.3 for the end-member case B2 is $0.1\ \mathrm{MPa}$ higher than the peak pressure for case A1. This variation is explained by faster diffusion rates in the intact rock for cases with higher background permeability (A2, B2). For comparison, the in-situ pressure in the shear zones pre-stimulation was found to be less than $0.5\ \mathrm{MPa}$ (Jalali et al., 2018).

Next, we consider the initial tendency for slip, which is calculated as the ratio of tangential to normal forces on the shear zones. Critically stressed shear zones tend to have values near the coefficient of friction, which is set to 0.8. By virtue of the friction model, the friction bound is the upper bound for the slip tendency. As can be seen in Figure 6.7, none of the shear zones appear to be critically stressed, with values ranging 0.15-0.19. This is reasonably consistent with the estimates from Fig. 15 of Krietsch et al. (2018b). Assuming an unperturbed stress tensor, they found a slip tendency up to 0.25 in some fractures and parts of the S1 shear zone. For other parts of S1, the slip tendency was estimated at ~ 0.2. Note that if the perturbed stress state is assumed (see Section 6.1.3 and Krietsch et al. (2018b)), the slip tendency was found experimentally to be as high as 0.5 for some orientations.

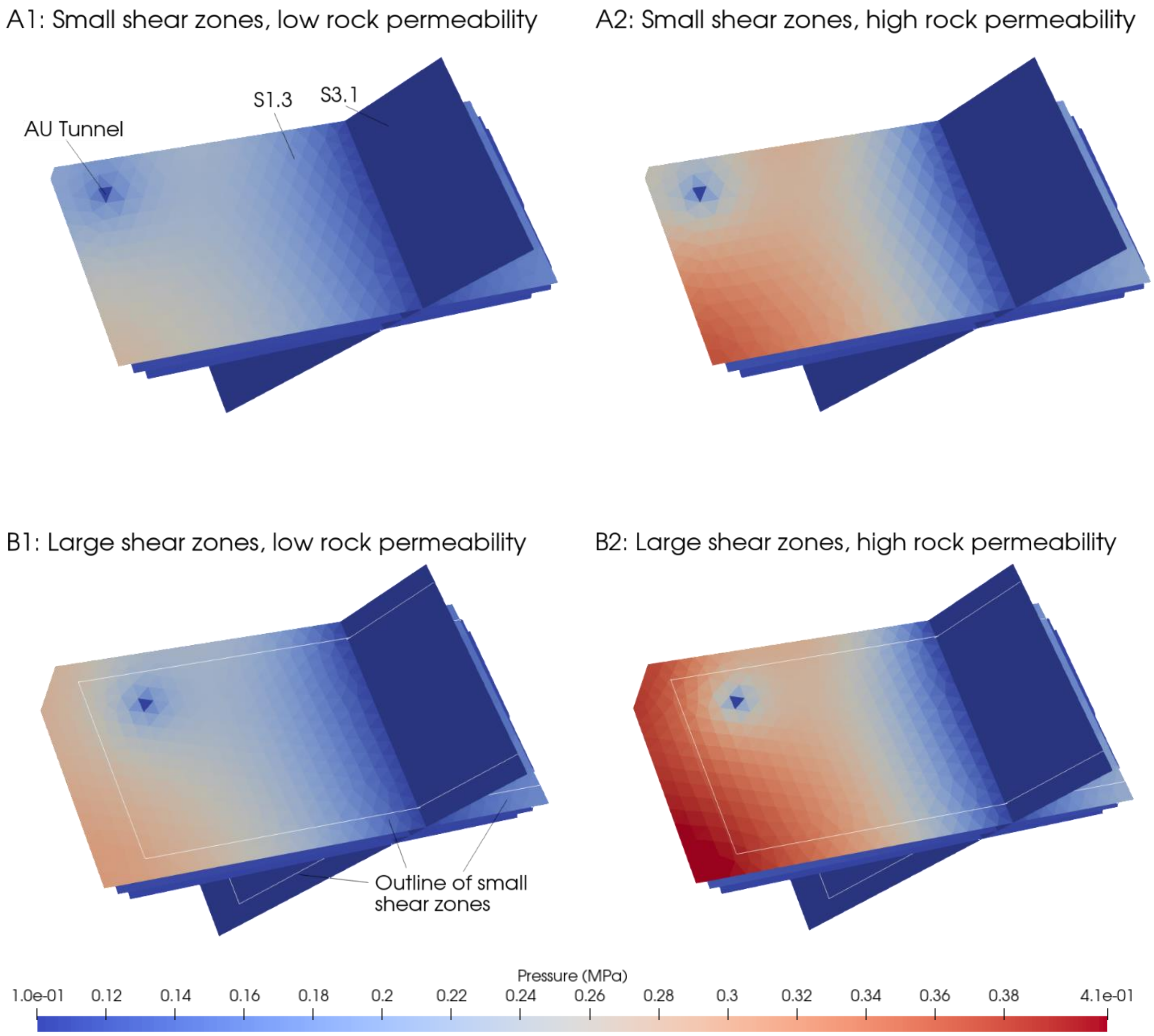

Figure 6.6 Pressure profile on the shear zones after 30 000 years initialization of the mechanical state with z-independent hydrostatic pressure at 480 m depth, followed by 30 years equilibration of fluid pressure due to excavation of the AU and VE tunnels at the ISC-site. Outline of S1.3 for the cases with small shear zones (option A) is displayed to visualize the relative differences in size between the cases.

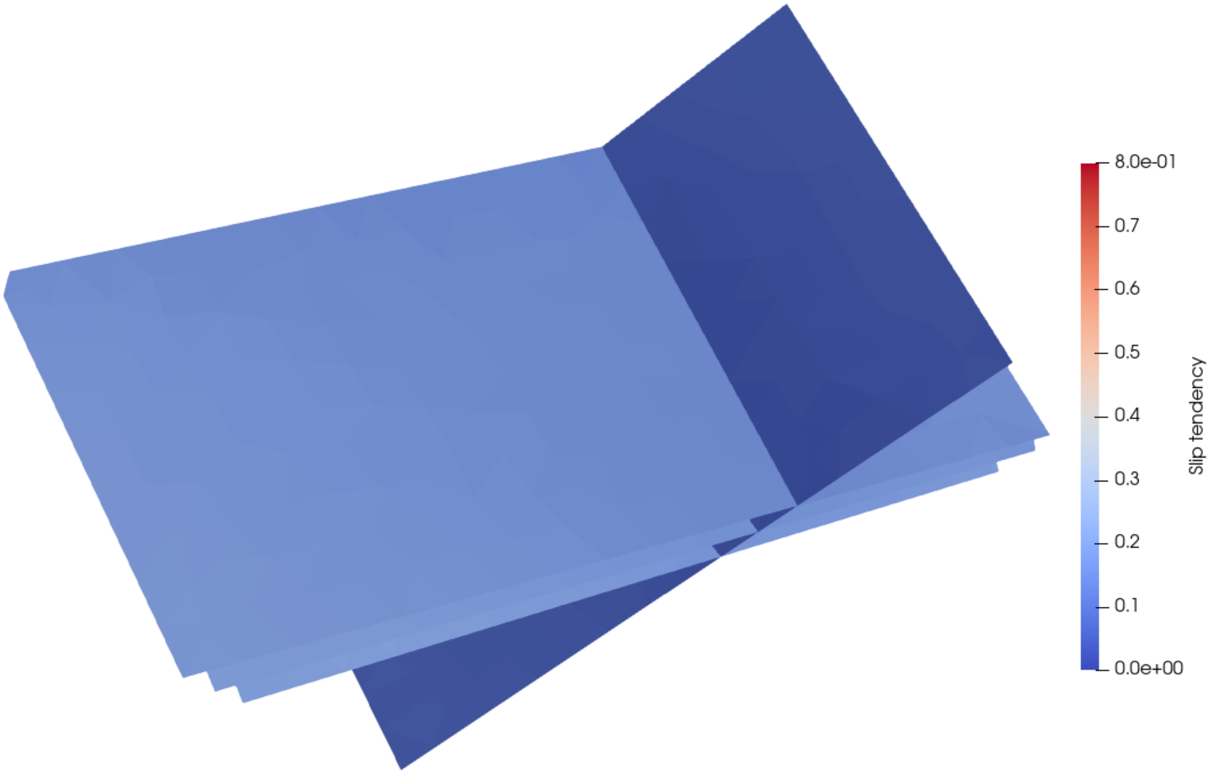

Figure 6.7 Slip tendency for the shear zones just before stimulation begins. For S1.3, the slip tendency is 0.15-0.19. Results from case A1.

6.5.2 Early pressure front propagation

The pressure distribution in S1.3 after 5 minutes of injection is shown in Figure 6.8. For the cases with low background permeability (option 1), the pressure profile extended further across the fracture compared to the cases with high background permeability (option 2). A higher background permeability results in greater pressure leakage into the intact rock, thereby reducing the extent of the pressure front within the shear zone.

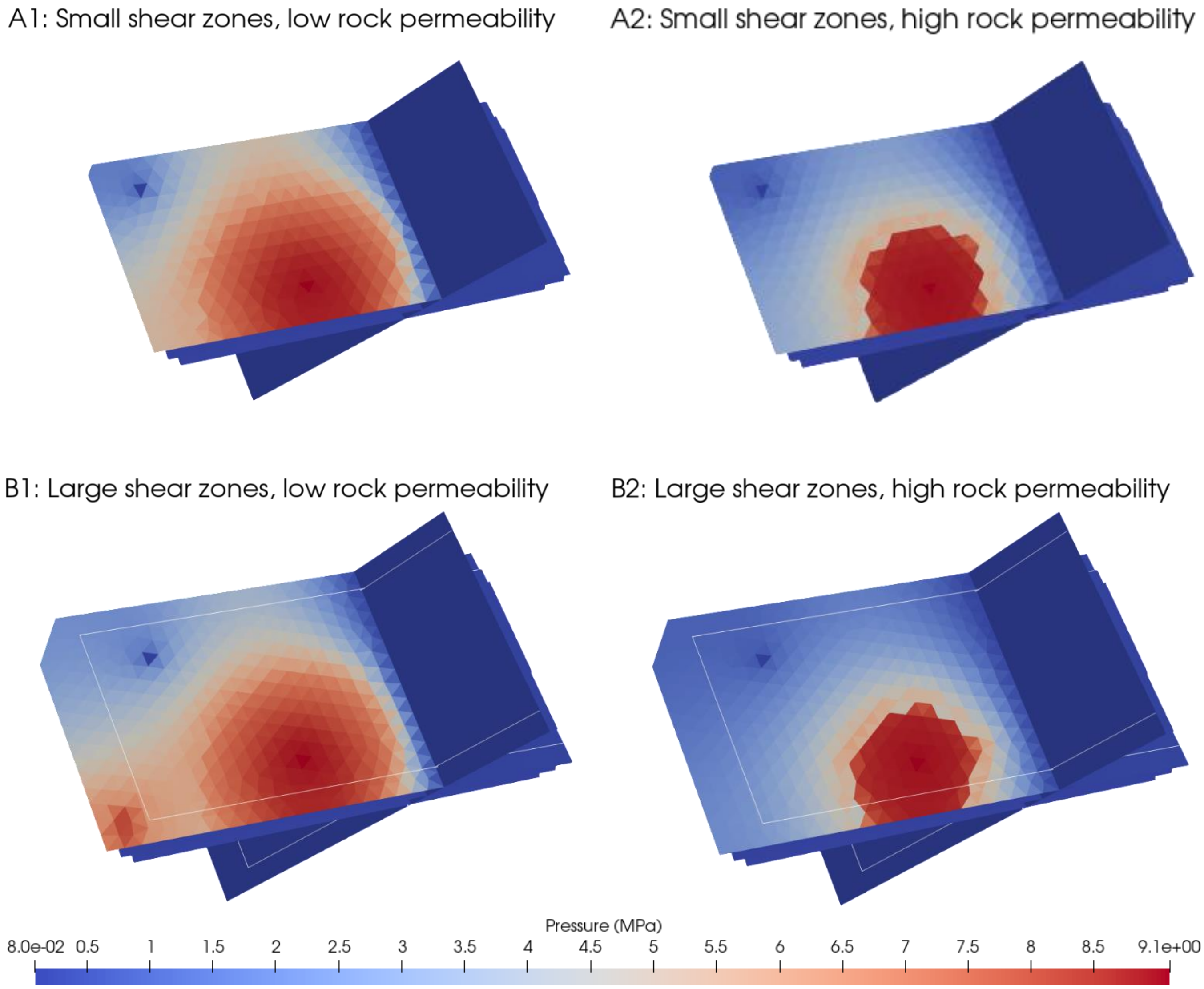

Figure 6.8 Pressure in S1.3 at T=5min after injection start for each simulation case.

To investigate the effect of the shear zone size on the pressure front, consider the state at $T = 7.5\ \mathrm{min}$. This corresponds to 5 minutes with an injection rate $15\ \mathrm{l/min}$, then 2.5 minutes with $20\ \mathrm{l/min}$. Consider the cases with high rock permeability, i.e. case A2 and B2. Figure 6.9 shows the isobars for each case, with a line extending radially from the injection point (of A2) to the 5 MPa isobar. For case B2, the 5 MPa isobar is $\sim 5\ \mathrm{m}$ closer to the injection point. This is expected since the extension of the domain downwards ($-z$ direction) should allow a greater proportion of the fluid to propagate downwards, as opposed to being forced to propagate upwards.

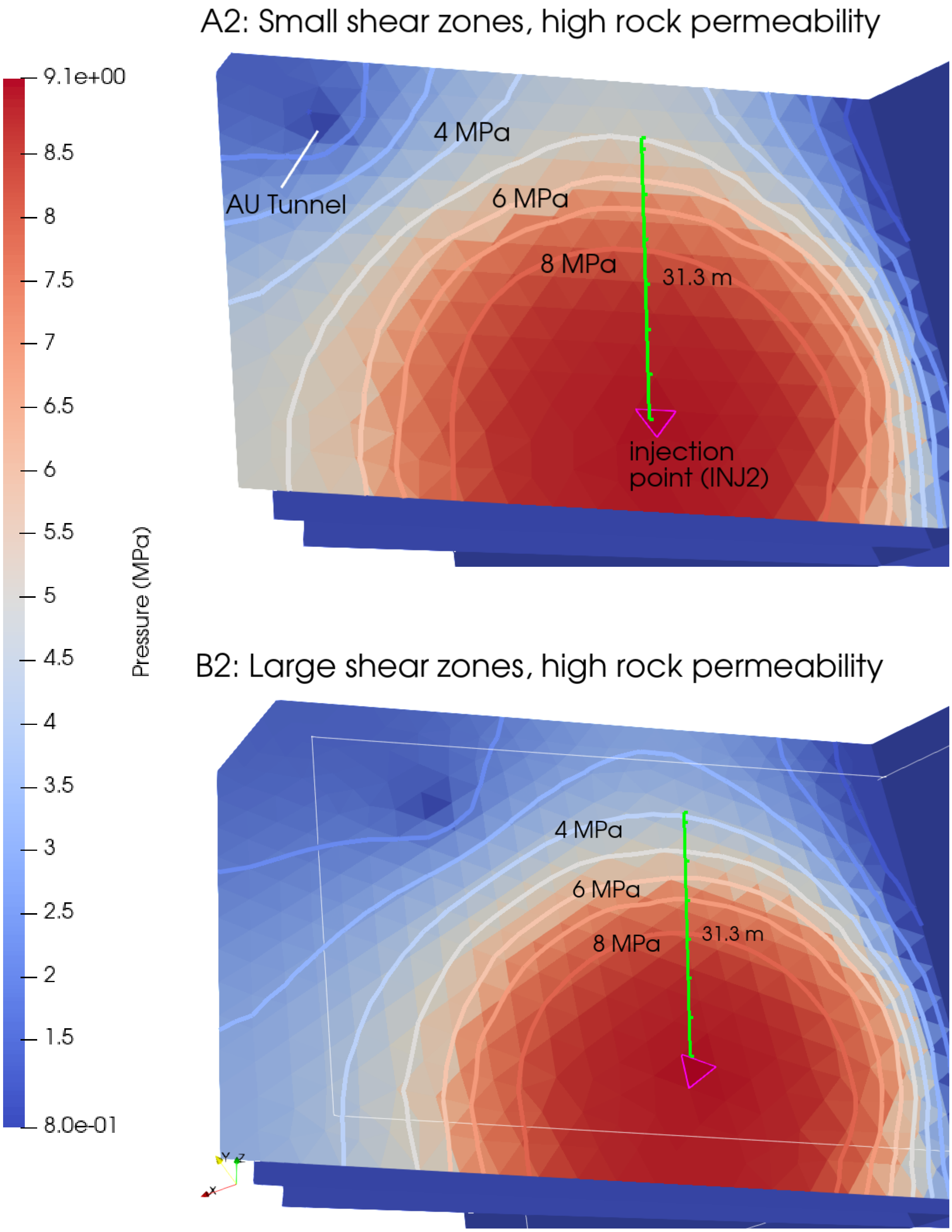
A2: Small shear zones, high rock permeability

B2: Large shear zones, high rock permeability

Figure 6.9 Pressure profile in S1.3 at T=7.5min. Top: Case A2, bottom: Case B2. Isobars, ranging from 1 to 8 MPa, are shown in intervals of 1 MPa. The pink cells denote the injection cell for each case. A green ruler with 5 m increments from the A2 injection cell to the 5 MPa isoline, with a total length of 31.3 m, is displayed. At 31.3 m from the injection point, case A2 has a higher pressure (5 MPa) *than case B2* (4 MPa).

6.5.3 Slip-induced Biot effects

Slip along the S1.3 shear zone is accompanied by a characteristic change in pressure in the intact rock, as seen in Figure 6.10. In the figure, the reference side is on the left corresponding to the positive interface Γ^+, relative to which the displacement jump is computed. As the left side of the shear zone dislocates upwards, the intact rock adjacent to the top left part undergoes compression, while the intact rock adjacent to the bottom left part expands. The opposite effect is seen on the right side, where the top region expands, while the bottom side compresses.

The pressure values in the regions with expansion, termed extensional lobes (Krietsch et al., 2020), are mostly negative. In Figure 6.10b and c, the low-opacity volume cells are regions where the pressure is less than atmospheric (0.1 MPa), also termed “negative” pressure. These regions correspond to the transition from open or sliding to sticking. The minimum negative pressure is at least $-2\ \mathrm{MPa}$ for $T = 7.5\ \mathrm{min}$ and $-3.2\ \mathrm{MPa}$ throughout the simulation period.

Basic analysis of magnitude and total volume of the negative pressure regions was conducted for all four cases. In all cases, the effect of extensional and compressional lobes due to slip was seen. The negative pressure was also correlated with the transition between sticking and sliding/open in all cases. However, we were unable to quantify any systematic differences between the cases.

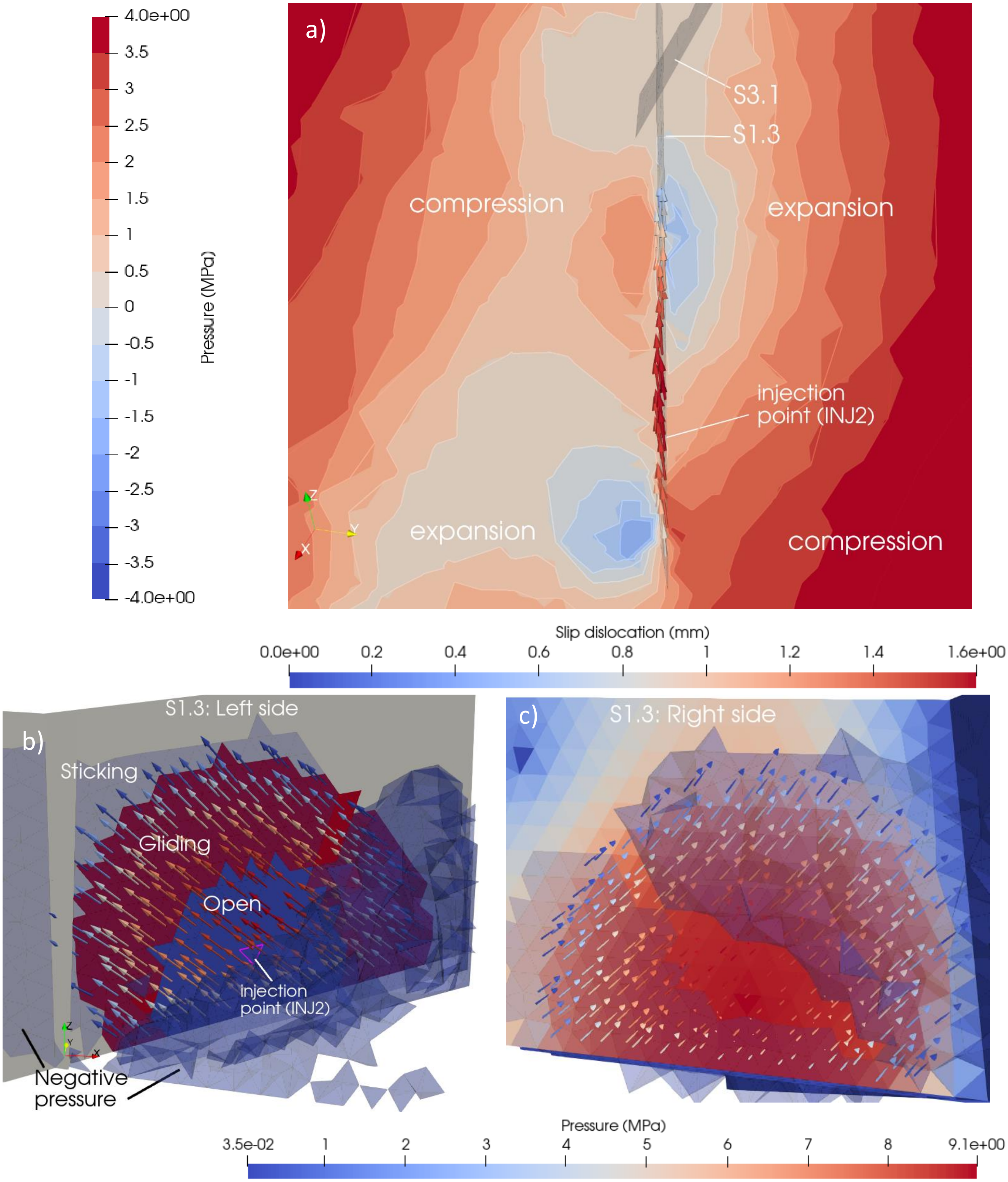

Figure 6.10: Extensional and compressional lobes due to slip on the shear zone surface for case A1 at T=7.5 min. a): side view of S1.3 with the slip vector (mm) on the shear zone. Slip is expressed in relative terms, with respect to the two sides of the shear zone. The slip is directed upward on the left side of S1.3 (reference side), relative to the right side of S1.3. The pressure contours represent a slice of the intact rock on both sides of S1.3. As the left side slips upwards, the cells in the intact rock are compressed

in the direction of the slip (top left) and expanded on the bottom left. The opposite occurs on the right side of the shear zone. b): view of the left side of S1.3. The blue, red, and neutral (off-white) colors represent parts of the shear zone that are open, gliding, and sticking, respectively. c): right view of S1.3. The pressure profile on S1.3 is shown. Note that the pressure scale of c) and a) are different. For b) and c), the low-opacity 3d-cells visualize regions of the intact rock with pressures lower than atmospheric pressure (0.1 MPa). Cells that appear in a dark blue color on the shear zones signify that the intact rock on the opposing side of the shear zone has negative (i.e. less than atmospheric) pressure values. The pressure within the shear zone is always positive.

6.5.4 Transient pressure profile at the injection interval

The average pressure near the INJ2 injection borehole in S1.3 is shown in Figure 6.11 for each simulation case, including the observed pressure profile and injection rate protocol. By near, we mean within a radius of 9 m of INJ2 in S1.3. It is evident that all of the simulated cases overestimated the near-borehole pore pressure by a significant amount. As the stimulation begins, the pressure for every simulation case immediately reaches $\sim 9\ \mathrm{MPa}$, and the pressure remain at this magnitude beyond shut-in at 14:10.

The apparent discrepancy in the temporal occurrence of the initial peak pressure between the cases is due to coarse time steps for cases A1 and B1, relative to cases A2 and B2, for the first time step with fluid injection. A1 and B1 required a longer time step of $dt = 5\ \mathrm{min}$ to converge, while A2 and B2 converged with $dt = 1\ \mathrm{min}$ for the first five minutes. All subsequent time steps during injection were $dt = 2.5\ \mathrm{min}$ for all cases.

The pressure values reported in Figure 6.11 are near-well averages. This procedure smooths out the maximum pressure value that is observed in the injection cell. The maximum peak pressure for any simulation case was $9.38\ \mathrm{MPa}$ at $T = 1\ \mathrm{min}$ for case B2. The corresponding near-well pressure for case B2 at this time was $7.10\ \mathrm{MPa}$. For comparison, the unperturbed stress tensor suggests that the stress normal to the fracture plane pre-stimulation is $9.34\ \mathrm{MPa}$, which is less than the maximum peak pressure for case B2. The peak pressure in the injection cell rapidly declined to values within $0.2\ \mathrm{MPa}$ of the mean near-well pressure a few minutes later for all simulation cases. The large pressure perturbation for the simulations may reflect insufficient fluid storage properties for the shear zone or limitations related to the singularity-like behavior that occurs at the injection point due to the lack of a well model.

A well model may be necessary to accurately reflect the near-well behavior. We model fluid injection by setting a positive value for the source term in the injection cell. This choice can result in an exceptionally large pressure gradient as the injection begins. The near-well behavior is non-linear, and we are unable to capture these effects with the current approach. A dimensionally reduced well model may be justified since the core diameter of the INJ2 injection well is $12\ \mathrm{cm}$. In contrast, the characteristic mesh size of the S1.3 shear zone is about $3 - 4\ \mathrm{m}$. With a well model, the injection interval is treated as a dimensionally reduced 1D segment in the 3D domain (Fabrie & Gallouët, 2000).

The insufficient fluid storage properties may be a result of the choice to model the shear zones as dimensionally reduced fracture surfaces where the fracture thickness equals the hydraulic aperture. Therefore, our model is suited to model the conductivity of the fractures. However, it is less clear whether storage properties are properly modeled with this approach since the shear zones are certainly thicker than what the hydraulic aperture suggests.

As can be seen from Figure 6.11, cases with large shear zones (option B) have a pressure drop markedly earlier than cases with small shear zones (option A). Although the precise pressure perturbations are not entirely resolved due to coarse time steps, we see that approximately 15 minutes after shut-in, the pressure starts to decrease for B-cases. Correspondingly, a similar decrease in pressure occurs approximately 40 minutes after shut-in for A-cases. The discrepancy between small (A) and large (B) shear zones is likely caused by more efficient diffusion of fluid pressure throughout the larger shear zones. For small shear zones, the pressure throughout the S1.3 shear zone is almost completely equilibrated with respect to the pressure at the injection point. In contrast, a pressure gradient away from the injection point is observed within S1.3 for cases with large shear zones. At shut-in, the pressure in B-cases decreases by a combination of diffusion to the intact rock and diffusion within the shear zone itself, while the pressure in A-cases predominately decreases by virtue of diffusion into the intact rock. Notice that the permeability of the intact rock does have an impact, as can be seen from the curves in Figure 6.11. The pressure for A2 and B2 decreases slightly faster than that for A1 and B1, respectively. However, the shear zone permeability is about four orders of magnitude greater than that of the intact rock, which helps explain the importance of shear zone diffusion over diffusion to the intact rock.

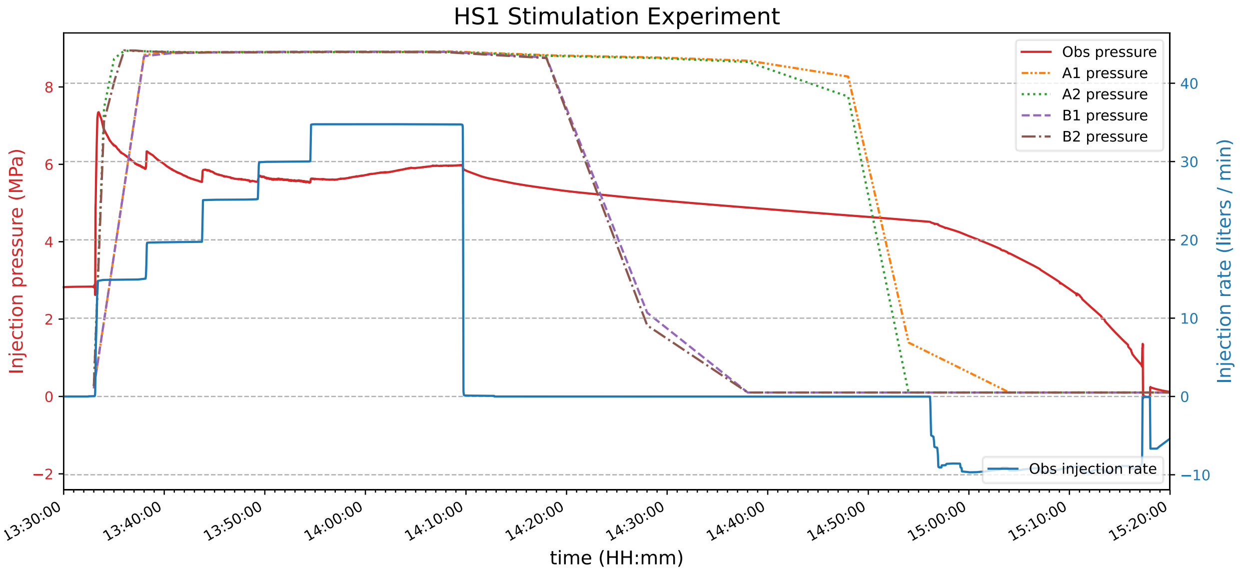

Figure 6.11 Transient pressure profile for the simulation cases. The orange, purple, grey, and brown lines are the average pressure in a radius of 9 meters near the injection point for cases A1, A2, B1, and B2, respectively. The red line is the observed pressure profile, and the blue line is the injection rate during the test. Note that the venting that occurs just before 15:00 is not included in the numerical simulation. The observational data is from Krietsch et al. (2019).

Cross-plots of the pressure and flow rates (Q-P) measured at the end of each constant-rate step during the main stimulation cycle (C3) are for each simulation case compared to the observed values from HS1 in Figure 6.12. The four simulation cases have virtually identical Q-P curves and are systematically higher than the observed pressure. The observed Q-P curve shows classic pressure-limiting behavior, with pressure declining before recovering towards the end of the stimulation experiment (Krietsch et al., 2020). The simulation cases also show pressure-limiting behavior, except that there are virtually no transient variations in pressure as the injection rate increases. The discrepancy in the initial pre-stimulation pressure between the simulations and observations can likely be explained by the two pre-stimulation phases (C1 and C2). These pressure-controlled phases added fluid to the system that was not completely removed during venting after C2 and may also have stimulated the system slightly. Certainly, Krietsch et al. (2020) suggested that breakage of cohesive bonds and shearing may have occurred during these phases.

In Table 6.9, we compare the pressures at the end of the first and fifth injection steps during the stimulation cycle. The similarities suggest that the numerical model can capture some of the same dynamics as the observations, whereby the pressure reaches a maximum limit. However, near-well pressure magnitudes do not match, which may reflect near-well model deficiencies. The injection pressure limit suggests that lift-off, i.e. separation of fracture walls, of the S1.3 shear zone has occurred. Lift-off can be associated with formation of new fractures, which is not accounted for in the present model, or shearing on pre-existing fractures (McClure & Horne, 2014).

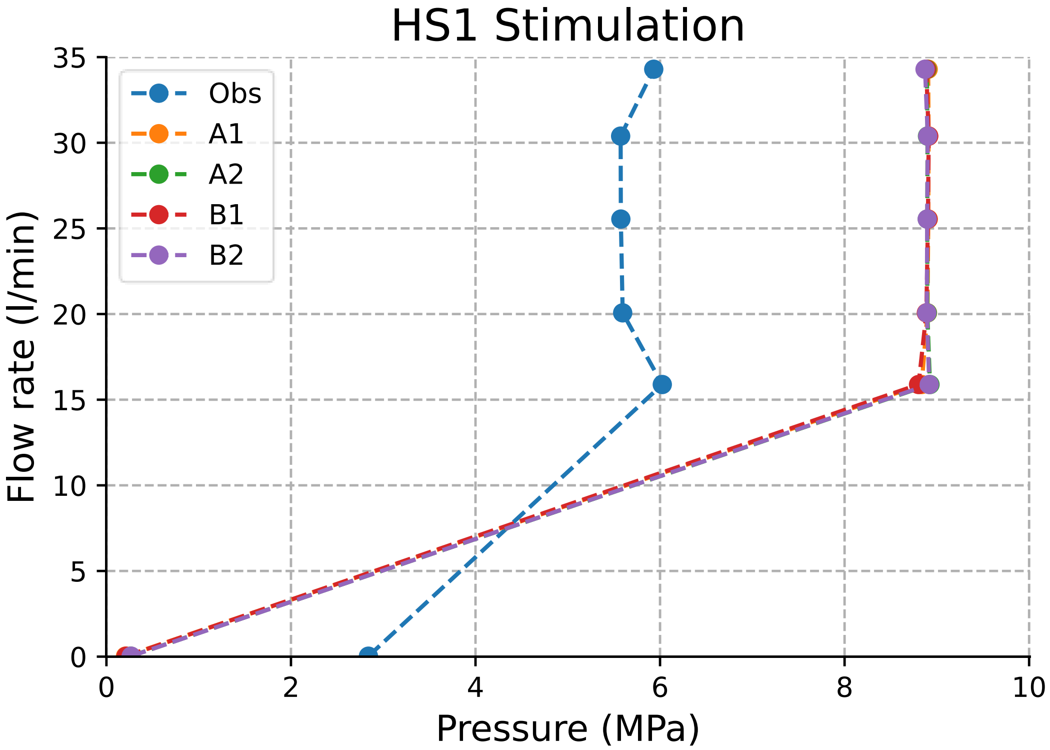

Figure 6.12 Cross plot of flow versus pressure data for the four simulation cases and the observed results from HS1, near the INJ2 injection borehole ($\mathrm{radius} < 9\ \mathrm{m}$)*. The curves are constructed by connecting the flow/pressure data at the end of each step during C3. The four simulation cases are virtually identical, and systematically higher than the observed flow/pressure data (blue). The initial pressure for the simulation cases are also significantly lower than the observed pressure. The observational data is from Krietsch et al. (2019).*

Table 6.9 Injection pressure measured at the end of the first and last step of the main stimulation cycle (C3). The pressure from the simulated cases (A1, A2, B1, B2) are computed as the average pressure within a radius of 9 m in S1.3. The difference between the pressure values is shown on the bottom row. The observational data is from Krietsch et al. (2019).

	HS1 (Obs.)	A1	A2	B1	B2
$\mathrm{P}_{\mathrm{Step1\text{-}C3}}$ (MPa)	5.91	8.83	8.93	8.80	8.92
$\mathrm{P}_{\mathrm{Step5\text{-}C3}}$ (MPa)	5.97	8.91	8.89	8.89	8.87
Difference (MPa)	+0.06	+0.08	−0.03	+0.09	−0.05

6.5.5 Hydraulic response in S1

Transient fluid pressure perturbations were recorded for the HS1 experiment in intervals along the PRP boreholes (Krietsch et al., 2020). We investigated three borehole – shear zone intersections at locations corresponding to two pressure monitoring intervals from the Grimsel experiment, see Table 6.10. To simplify computation of pressures in the intervals, we considered the average pressure in a small region surrounding the intersection between a monitoring interval and a shear zone. Also, we are primarily interested in shear zones away from S1.3, meaning that we disregarded the PRP1-1 intersection with S1.3 in the following. An overview of the monitoring intervals for the simulations is provided in Table 6.11, including direct distance from the INJ2 injection borehole in S1.3 to the intervals.

Table 6.10 Overview of a subset of pressure monitoring intervals used during HS1. Data retrieved from Table 2 of Krietsch et al. (2020).

Interval name	Interval width (m)	Number of fractures	Shear zones
PRP1-1	6.1	14	S1.2 & S1.3
PRP3-1	7.5	4	S1.1 & S1.2

Table 6.11 Overview of pressure monitoring intervals for simulations of the HS1 experiment. The data is from Krietsch et al. (2020).

Interval name (borehole – shear zone)	Depth in borehole (m)	Coordinates (x, y, z) (local Grimsel coordinates)	Distance to INJ2 injection borehole in S1.3 (m)
PRP1 – S1.2	38.7	(48.6, 111, 5.8)	8.0
PRP3 – S1.2	31.7	(56.3, 118.7, 19.7)	17.5
PRP3 – S1.1	26.1	(58.4, 114, 22.0)	20.9

In each simulation case, the pressure perturbations in the monitoring intervals never exceeded $2 \mathrm{~MPa}$ even though peak injection pressures were nearly $9 \mathrm{~MPa}$ (Figure 6.13). The peak pressure observed in PRP1-1 was less than $0.25 \mathrm{~MPa}$ throughout the C3 cycle, and in PRP3-1, less than $0.5 \mathrm{~MPa}$ (Figure A4f from Krietsch et al. (2020)). However, these intervals covered multiple shear zones and stretches of intact rock, so the pressure is not expected to match exactly. The perturbations for the simulations were significantly higher than observations for all four cases. However, there are discernible differences between the four cases. Pressure build-up between $T = 10\ \mathrm{min}$ and $T = 35\ \mathrm{min}$ is similar in all cases, with some notable variations.

For case B1, with large shear zones and low rock permeability, a large pressure perturbation occurred between $T = 30\ \mathrm{min}$ and $T = 35\ \mathrm{min}$. This perturbation was caused by an instantaneous increase in pressure in the corner of the S1.2 shear zone. In fact, the perturbation was large enough locally to cause a small amount of slip in the region. While the reasons for this behavior are not fully understood, we hypothesize that effects due to the coupled nature of the dynamics are at play. We observed opening of parts of S1.3 adjacent to this region immediately before the pressure spike, which may have caused local stress transfer between the shear zones. Another plausible explanation is that the model is unable to represent the physics accurately near the shear zone edge if the edge is open or gliding, in which case fracture propagation would normally be expected.

Besides this anomaly, the cases with large shear zones have qualitatively similar pressure profiles, with a rapid decline following shut-in. This is correlated with the decline occurring at the injection point 15 minutes after shut-in (see Figure 6.11). For the cases with small shear zones, there is a slower pressure decline until a rapid drop occurs at $T = 75\ \mathrm{min}$, i.e. 40 minutes after shut-in, which is the same time at which a rapid decline occurs at the injection point. We remark that long time steps were used after shut-in, which means that delayed responses in the monitoring boreholes may not have been resolved in the solution. This also implies that we are not able to properly categorize responses as immediate or delayed, which was suggested by Krietsch et al. (2020) as a way to understand whether pressure signals are diffusive (delayed), or poroelastic (immediate) in nature. The latter type represents the fluid pressure changes due to stress changes and concomitant volumetric deformation.

The pressure in several monitoring intervals remained perturbed at a level slightly lower than atmospheric pressure by the end of the simulations. The largest measured difference was a decline of $0.05\ \mathrm{MPa}$ for case B2 at the PRP1 – S1.2 interval. The intervals further away from the injection point were closer to (or exactly) atmospheric pressure at $T = 110\ \mathrm{min}$. The negative perturbations may be caused by poroelastic effects from the stimulated shear zone, which resulted in negative pressure values in the intact rock due to slip in the S1.3 shear zone.

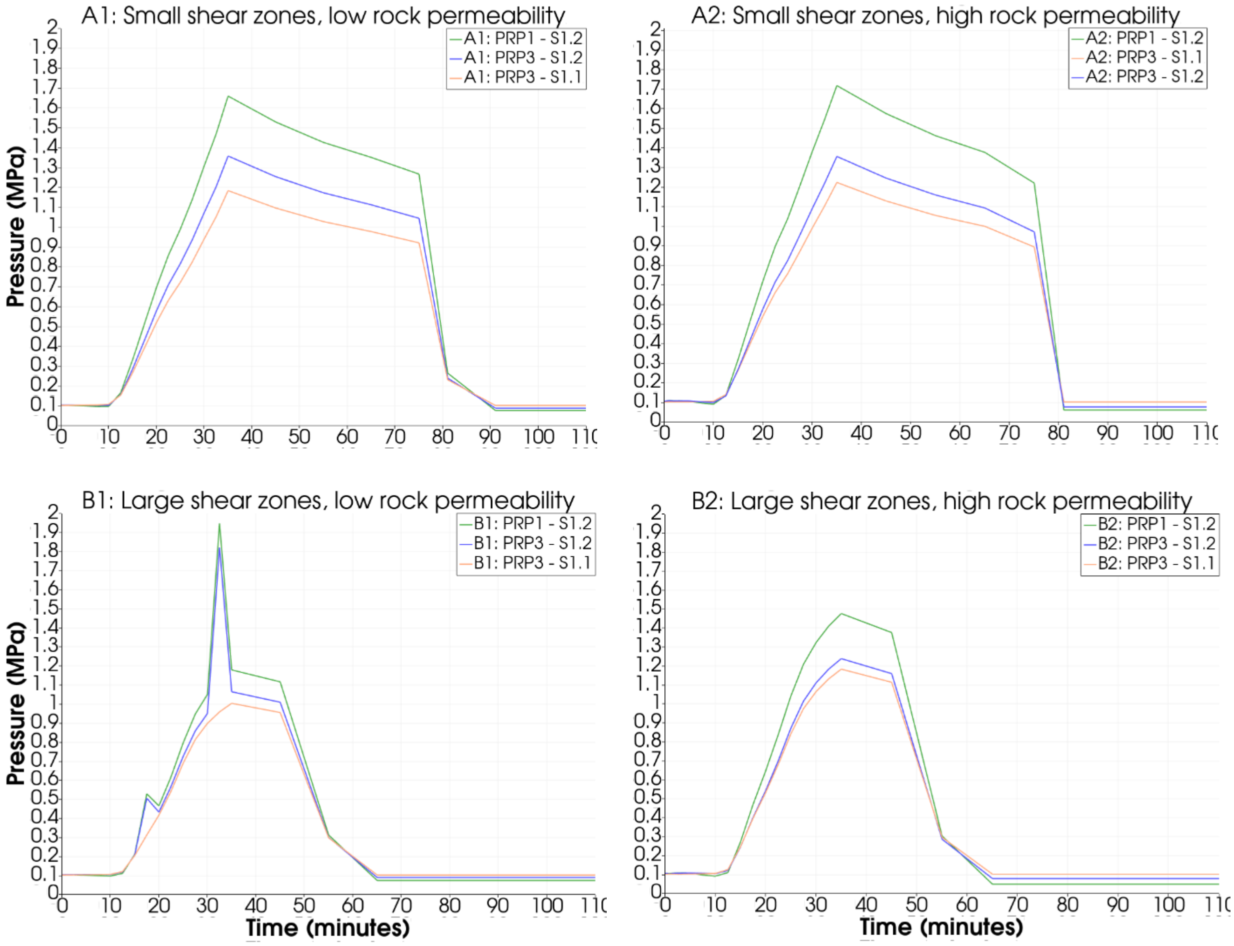

Figure 6.13 Pressure perturbation time series for PRP monitoring intervals. Rate-change steps were at 0, 5, 10, 15, 20 minutes. Shut-in occurred at 35 minutes.

The pressure at shut-in at the monitoring intervals is displayed in Figure 6.14. Cases with small shear zones (A1, A2) tend to have a slightly higher shut-in pressure in the monitoring intervals than the cases with large shear zones (B1, B2). Additionally, there is virtually no spread in pressure for A-cases, while B1 and B2 have noticeable pressure differences at the same monitoring intervals. The lower overall pressures in B1 are likely explained by the larger shear zones more effectively distributing pressure within the target shear zone (S1.3), and the lower rock permeability less efficiently diffusing pressure between the shear zones. However, given the pressure spike observed in Figure 6.13 which occurs at $T = 32.5$ min, the overall trend of the pressure profile may be harder to interpret. Either way, the simulated pressure distribution at shut-in is 5 to 10 times higher than the observed pressure distribution at similar distances (ref figure A5 e. of Krietsch et al. (2020)).

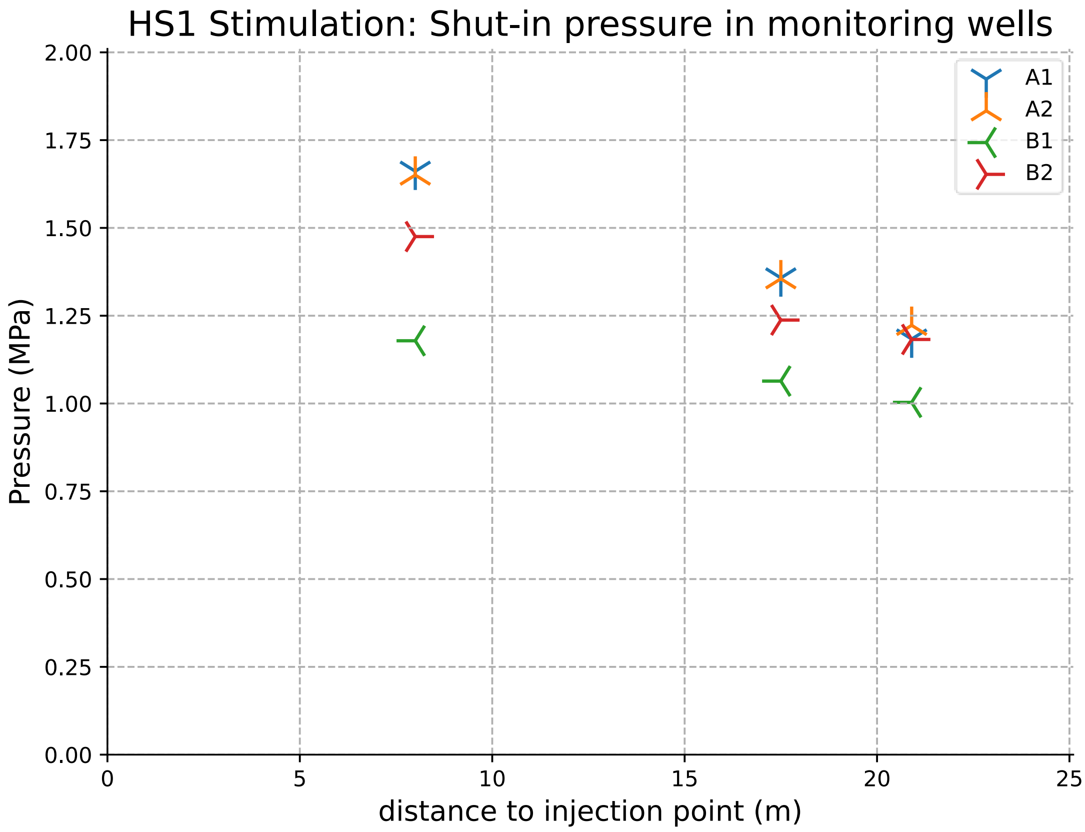

Figure 6.14 Shut-in pressure ($T = 35$ min) *in monitoring intervals with respect to radial distance to the INJ2 injection point. The measurement points correspond to the intervals listed in Table 6.11.*

6.5.6 Cumulative slip and transmissivity enhancement

The transient near-well slip evolution for all simulation cases are characterized by approximately ~ 1.2 mm slip during the first five minutes of injection, then ~ 0.5 mm additional slip during the next five minutes. The slip dislocation stabilized after approximately 20 minutes for all simulation cases. The estimates for cumulative injection-induced slip and transmissivity enhancement for each simulation case are shown in Table 6.12. For direct comparison with results, we computed slip and induced transmissivity near the injection well. In addition, we also computed the average transmissivity throughout the interior of the S1.3 shear zone. We see that the interval transmissivity is lower than the average transmissivity throughout S1.3. The largest slip values were observed toward the center of S1.3, which cause a higher transmissivity enhancement. The injection point on the other hand, is located towards the bottom of the shear zone.

The direction of the slip vector is visualized in Figure 6.10, which is towards 250/43 (dip direction/dip). The simulated slip was remarkably similar across variations of the background permeability. Compared to the observed slip dislocation, the simulations overestimate slip by a factor of three. The difference in transmissivity enhancement between simulations and observations is at most one order of magnitude.

Table 6.12 Cumulative slip dislocation and transmissivity enhancement for each simulation case, and HS1 observations. Results are provided near the injection borehole, and across the S1.3 shear zone. The observed values were reported by Krietsch et al. (2020).

	A1	A2	B1	B2	Observed
Average Interval transmissivity (m2/s)	8.5e-7	8.5e-7	1.3e-6	1.3e-6	1.5e-7
S1.3 average transmissivity (m2/s)	1.2e-6	1.2e-6	1.9e-6	2.0e-6	--
Average interval cumulative slip dislocation (mm)	1.95	1.94	2.29	2.28	0.7 – 0.81

7 Discussion and conclusion

In this thesis, we modeled a hydraulic shearing experiment conducted as part of the In-Situ Stimulation and Circulation experiment at the Grimsel Test Site. We applied a fully coupled hydro-mechanical model for deformable fractured porous media. A discrete fracture matrix model was employed that explicitly represents shear zones as two-dimensional planar fractures embedded in the intact rock. The poroelastic equations in the intact rock is a coupled system of consisting mass and momentum balance, and constitutive relations for the fluid flux and total stress. Mass balance in the intact rock is coupled to mass balance in the shear zones and shear zone intersections by interface fluxes and source terms. Similarly, momentum balance in the intact rock is coupled to a Coulomb friction law and non-penetration condition in the planar two-dimensional shear zones. The shear zone aperture is modeled with an empirical shear dilation relationship, and shear zone transmissivity is modeled using the cubic law. The equations are discretized using multi-point finite volume methods, implicit time stepping, and a semi-smooth Newton method for fracture contact mechanics and fracture deformation.

Using the model described above, we have performed the first simulation of one of the hydroshearing experiments at the Grimsel Test Site where poroelasticity in the intact rock is coupled to flow and deformation of the shear zones. To a substantial extent, we were able to capture key features of the stimulation test. Simulated transmissivity enhancement at the borehole was within one order of magnitude of the observations. We found pressure-limiting behavior consistent with observations. Our model captured slip-induced poroelastic effects that produced extensional and compressional regions in the intact rock, on both sides of the target shear zone. These slip-induced effects were also described by Krietsch et al. (2020) as a fundamental deformation mechanism.

A result of the slip-induced poroelastic effects were negative pressure values in the extensional regions. We interpret these values to be a result of the assumption that the pores are saturated by a single-phase fluid that is only slightly compressible. Therefore, as the cells next to the target shear zone expand, the pressure drops since the fluid cannot sufficiently expand. In reality, the system is partially drained, which means that the pores are saturated by a two-phase fluid consisting of air and water. Air can easily expand and fill the additional volume due to the rock expansion. This illustrates an inherent limitation of our modeling approach.

Another aspect that may influence the deformation of the intact rock near the shear zones is the assumption that the crystalline rock is linearly elastic near the shear zones, with homogeneous and isotropic elastic parameters. The S1 and S3 shear zones are ductile and brittle-ductile structures, respectively. The S3 shear zone particularly, has an extraordinarily complex mechanical structure. The mylonitic cores bound a highly fractured zone, and are each bounded by a transition zone, so that the full damage zone width is $\sim 5\ \mathrm{m}$ (Wenning et al., 2018). The host rock adjacent to the shear zone is characterized by decreased mechanical strength due to microfracturing and anisotropic elastic properties due to the foliations. In contrast, we modeled all shear zones as two-dimensional planar, open fractures, therefore disregarding structural thickness. Additionally, we only included S3.1 in the simulation due to issues with convergence for closely spaced fractures relative to the characteristic mesh size. With these aspects in mind, it is unlikely that a linearly elastic model accurately captures the interactions between rock and fault deformation. The additional complications arising from the presence of the foliations, inducing anisotropic elastic properties, make the accurate mechanical modeling of the shear zones a delicate issue.

The HS1 experiment targeted the S1 shear zone which is farthest away from the S3 shear zone, therefore limiting the direct hydraulic interaction between the target shear zone and the S3 shear zone. To assess the impact of our assumptions on the shear zones and parameter values, we evaluated different scenarios by varying the permeability of the intact rock and the size of the shear zones. In all cases, the simulated near-well pressure perturbations significantly exceeded the observed pressure. We hypothesize that this discrepancy is due to the lack of a well model to account for the singularity introduced by our approach to borehole injection, and the lack of sufficient storage in the shear zones. The study is nonetheless showing the significant impact of shear zone extent on the transient pressure profile, especially following shut-in. We also observed clear differences in the transient propagation of the pressure front with variations of the permeability of the intact rock. These observations emphasize the critical importance of knowledge of the spatial distribution of hydraulic properties, and of the geological characteristics of the rock mass.

Another limitation is related to the lack of gravitational effects, see Section 4.7. Gravity acts as an external force on the momentum and mass balance equations. Since the vertical height of the shear zones is roughly $50\ \mathrm{m}$ in the model, we would expect a noticeable impact on the solution. In particular, we anticipate that the direction of fluid flow and slip be modified, which would impact the interpretation of the results.

There is also uncertainty related to the sparsity of in-situ data. Although many parameter-related deficiencies can be mitigated by heterogeneously or anisotropically modifying the parameter field, care must be taken in order to avoid over-parameterization of the model in cases where the data is insufficient to identify additional parameters. For example, there is great uncertainty with respect to initialization of the model with respect to stress conditions, effect of tunnels, and permeability distribution.

Despite model limitations, this study has demonstrated the promise of using fully coupled discrete fracture matrix models to enhance our understanding of coupled hydro-mechanical processes for hydraulic stimulation of fractures. The modular design principles underlying the DFM approach and our implementation specifically, means that extensions that more accurately depict specific aspects the dynamics are within reach.

7.1 Outlook

Numerous extensions of the model would improve our confidence in the results presented in this thesis. In the following, we will briefly discuss some potential extensions to the current model that relate to elastic properties, dilation, permeability distribution, two-phase flow, and gravitational effects.

Elastic properties of the rock are commonly assumed homogeneous and isotropic in hydromechanical simulations of subsurface rock. Krietsch et al. (2018b) estimated the elastic anisotropy of the rock mass due to the presence of foliations. By extending the model to allow for transversely isotropic elastic parameters combined with a heterogeneous parameter distribution near the shear zones, we could potentially gain a better understanding of the stress and deformation effects near the shear zones. Importantly, these stresses influence the tendency for slip, which is critical in terms of modeling slip-induced dilation and transmissivity enhancement in the target shear zone.

The pressure propagation in the target shear zone is influenced by the permeability distribution and gravitational effects. Introducing gravitational effects induces a natural pressure gradient to the system. Additionally, Following Villiger et al. (2020b) a heterogeneous permeability distribution could be applied in the target shear zone, then compute the average tendency of pressure propagation and cumulative slip dislocation following multiple simulations with varying initial conditions.

To better understand the slip-induced effects which results in abnormally low pressure near the shear zones, and in acknowledgement that the system is partially drained, we could model the fluid as two-phase. This would better reflect the in-situ conditions and hopefully improve our understanding of the pressure distribution due to expansion of the rock.

8 Appendix

8.1 Hydraulic parameter relations

Permeability ($\mathcal{k}$) is an intrinsic property of a porous medium and appears as a second-order tensor in Darcy's law. The quantity has dimensions $\left[\mathrm{L}^2\right]$. In literature, two other relatable quantities are often reported, namely hydraulic conductivity and transmissivity.

Hydraulic conductivity (K) is defined as the specific discharge per unit hydraulic gradient (Bear, 1988), with dimensions $\left[\mathrm{LT}^{-1}\right]$. It is a quantity dependent on both fluid and matrix properties and may intuitively be understood as the ease of which a fluid flows through a porous medium. Specifically, it combines the intrinsic permeability ($\mathcal{k}$) with fluid density (ρ_f) and dynamic viscosity (μ),

$$K = \frac{\mathcal{k}\rho_f g}{\mu}.$$

Note that the product of density and gravity ($\rho_f g$) is referred to as the specific weight of a fluid, i.e. the weight of fluid per unit volume (dimensions $[\mathrm{ML}^{-2}\mathrm{T}^{-2}]$). The transmissivity takes into account the interval thickness, b $[\mathrm{L}]$, so that

$$T = K \cdot b.$$

At the Grimsel Test Site, the in-situ water during characterization and stimulation experiments is kept at 11 °C (Keusen et al., 1989). At this temperature, the dynamic viscosity $\mu = 1.26 \times 10^{-3}$ Pa·s, and specific weight $\rho g = 9.80 \times 10^3\ kg/(m^2 s^2)$. Conversion between hydraulic conductivity and permeability can therefore be achieved by

$$K = 7.75 \times 10^6 \cdot k.$$

8.2 Stress tensor rotations

In practical applications, the stress tensor is often reported in the principal coordinate system; the system where all shear stresses vanish. On the other hand, the geometry of a physical rock volume is often reported in terms of easting, northing and elevation. For the purposes of solving practical applications, it is therefore necessary to transform the reported stress tensor to the coordinate system used by the physical domain. To illustrate this process, we consider the reported unperturbed stresses from the ISC project (Krietsch et al., 2018a), reproduced in Table 8.1.

Table 8.1 Principal stress components of the domain in terms of dip direction (γ) and dip (θ). Data from (Krietsch et al., 2018a).

Stress component	σ_1	σ_2	σ_3
Value [MPa]	13.1	9.2	8.7
Dip direction, γ [°]	104.48	259.05	003.72
Dip, θ [°]	39.21	47.90	12.89

The dip direction (γ) is the angle from northing in clockwise direction, and the dip (θ) is the angle below the horizontal. We may write the direction of each stress components in Euclidean coordinates using the following transformation,

$$r_i = \begin{bmatrix} \cos\theta \sin\gamma \\ \cos\theta \cos\gamma \\ -\sin\theta \end{bmatrix}. \tag{8.1}$$

Combining the three principal directions to a matrix, we get the rotation operator

$$R = \begin{bmatrix} 0.750 & -0.658 & 0.063 \\ -0.193 & -0.127 & 0.973 \\ -0.632 & -0.742 & -0.223 \end{bmatrix}. \tag{8.2}$$

In the principal coordinate system, the stress tensor reads,

$$\sigma = \begin{bmatrix} 13.1 & 0 & 0 \\ 0 & 9.2 & 0 \\ 0 & 0 & 8.7 \end{bmatrix} \text{ MPa}. \tag{8.3}$$

Thus, the stress tensor in Euclidean coordinates is computed as

$$\sigma' = R\sigma R^T = \begin{bmatrix} 11.39 & -0.60 & -1.84 \\ -0.60 & 8.87 & 0.59 \\ -1.84 & 0.59 & 10.73 \end{bmatrix} \text{ MPa}. \tag{8.4}$$

8.3 Code contributions

The computer code that facilitates the numerical simulation is implemented in the open-source software PorePy[2]. A thorough introduction to the conceptual models and implemented discretizations can be found in Keilegavlen et al. (2020). Implementations done in PorePy related to this thesis are:

- Development of code to implement generic filters for the mixed-dimensional assembler. The assembler a class that discovers and discretizes all terms in a model. This contribution improves modeling of non-linear problems, where re-discretization of individual terms is needed before every Newton iteration. The code has subsequently been expanded by other authors.
- Development of code to facilitate nested grid convergence for three-dimensional unstructured grids. Grid convergence studies improve our confidence in the model where analytical reference solutions does not exist. This contribution implements an algorithm to track the overlap

---

[2] https://github.com/pmgbergen/porepy

between cells in nested refinements of a domain, so that grid convergence studies can be performed. The code has subsequently been expanded by other authors.

- Support for PorePy on Windows operating systems. PorePy is mainly developed on Linux, which can be a barrier for students and researchers who have Windows computers. This contribution examined and restructured dependencies for PorePy to add unofficial support for Windows OS.
- General code maintenance, including bug fixes to discretization methods, improvements to documentation, and efficient re-implementation of algorithms.

Separately, the code that connects all the features of PorePy to model the hydroshearing experiment the Grimsel Test Site is found at https://github.com/haakon-e/mastersproject. There, run scripts for the simulation cases in this thesis are available. The code is implemented with modular design principles, and can be categorized as follows (see also Figure 8.1):

- Code to extract and manipulate geometric data of boreholes, shear zones, and tunnels for the ISC experiment at the Grimsel Test Site. The code is a Python re-implementation of the Matlab code that is associated with Krietsch et al. (2018a).
- Models that implement flow, mechanics, and Biot model for poroelasticity
- Abstract and flexible protocols for time stepping and injection phases
- TimeMachine: A framework that manages execution of time-dependent models. The code includes useful procedures related to non-linear models, including retrying time steps on failure of the Newton method.

In total, the implementation exceeds 7000 lines of code.

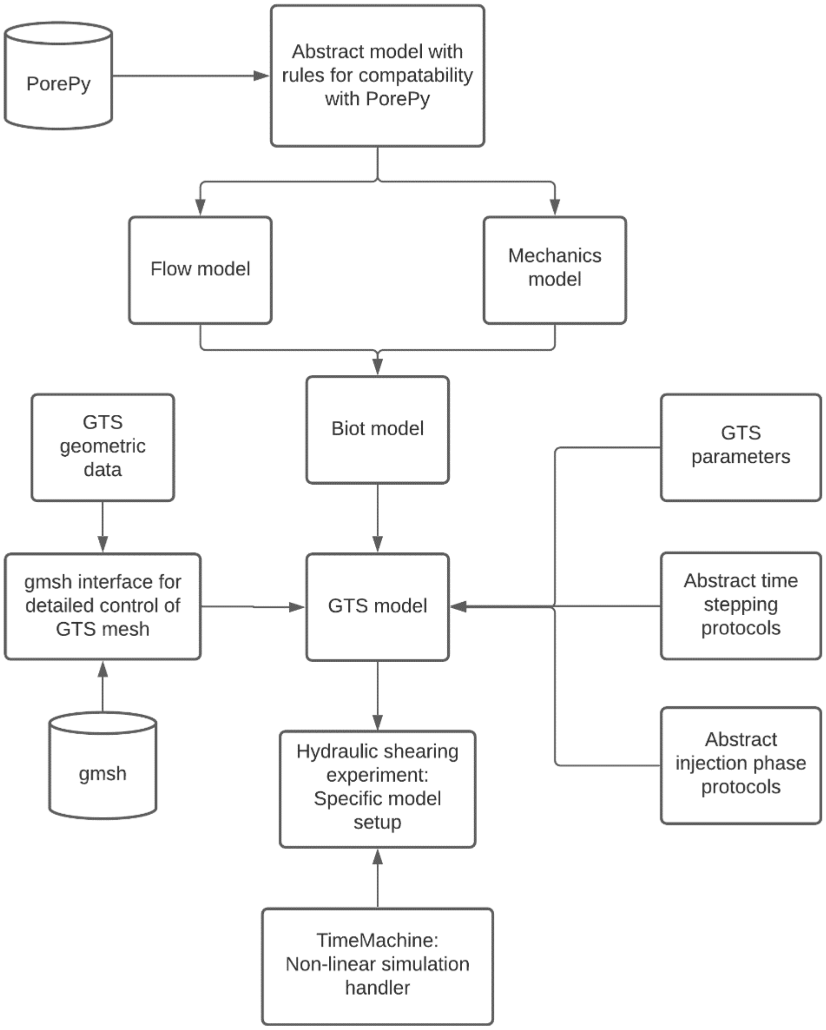

Figure 8.1 Overview of the code structure for the implementation of the GTS hydraulic shearing experiment in the PorePy framework. The rectangles signify components of the code and arrows indicate dependencies between components. The main external packages, PorePy and gmsh, are displayed as cylinders. The figure illustrates the modular approach to implementation, which means that extensions can more easily be implemented.

References

Abell, B. C., Choi, M.-K., & Pyrak-Nolte, L. J. (2012). *Shear Specific Stiffness of Fractures And Fracture Intersections* 46th U.S. Rock Mechanics/Geomechanics Symposium, Chicago, Illinois.

Ahrens, J., Geveci, B., & Law, C. (2005). 36 - ParaView: An End-User Tool for Large-Data Visualization. In C. D. Hansen & C. R. Johnson (Eds.), *Visualization Handbook* (pp. 717-731). Butterworth-Heinemann. https://doi.org/https://doi.org/10.1016/B978-012387582-2/50038-1

Amann, F., Gischig, V., Evans, K., Doetsch, J., Jalali, R., Valley, B., Krietsch, H., Dutler, N., Villiger, L., Brixel, B., Klepikova, M., Kittilä, A., Madonna, C., Wiemer, S., Saar, M. O., Loew, S., Driesner, T., Maurer, H., & Giardini, D. (2018). The seismo-hydromechanical behavior during deep geothermal reservoir stimulations: open questions tackled in a decameter-scale in situ stimulation experiment. *Solid Earth, 9*(1), 115-137. https://doi.org/10.5194/se-9-115-2018

Angot, P., Boyer, F., & Hubert, F. (2009). Asymptotic and numerical modelling of flows in fractured porous media. *ESAIM: M2AN, 43*(2), 239-275. https://doi.org/10.1051/m2an/2008052

Ayling, B., & Moore, J. (2013). Fluid geochemistry at the Raft River geothermal field, Idaho, USA: New data and hydrogeological implications. *Geothermics, 47*, 116-126. https://doi.org/10.1016/j.geothermics.2013.02.004

Ballas, G., Fossen, H., & Soliva, R. (2015). Factors controlling permeability of cataclastic deformation bands and faults in porous sandstone reservoirs. *Journal of Structural Geology, 76*, 1-21. https://doi.org/10.1016/j.jsg.2015.03.013

Bandis, S. C., Lumsden, A. C., & Barton, N. R. (1983). Fundamentals of rock joint deformation. *International Journal of Rock Mechanics and Mining Sciences & Geomechanics Abstracts, 20*(6), 249-268. https://doi.org/10.1016/0148-9062(83)90595-8

Barton, N., Bandis, S., & Bakhtar, K. (1985). Strength, deformation and conductivity coupling of rock joints. *International Journal of Rock Mechanics and Mining Sciences & Geomechanics Abstracts, 22*(3), 121-140. https://doi.org/10.1016/0148-9062(85)93227-9

Bear, J. (1988). *Dynamics of Fluids in Porous Media*. Dover. https://books.google.no/books?id=picSrNsgY8oC

Berge, R. L., Berre, I., Keilegavlen, E., Nordbotten, J. M., & Wohlmuth, B. (2019). Finite volume discretization for poroelastic media with fractures modeled by contact mechanics. *International Journal for Numerical Methods in Engineering*. https://doi.org/10.1002/nme.6238

Berkowitz, B. (1995). Analysis of fracture network connectivity using percolation theory. *Mathematical Geology, 27*(4), 467-483. https://doi.org/10.1007/BF02084422

Berre, I., Berge, R., Keilegavlen, E., & Ucar, E. (2018a). *Three-Dimensional Numerical Modelling of Fracture Reactivation in Hydraulic Stimulation of Geothermal Reservoirs* 2nd International Discrete Fracture Network Engineering Conference, Seattle, Washington, USA.

Berre, I., Boon, W., Flemisch, B., Fumagalli, A., Gläser, D., Keilegavlen, E., Scotti, A., Stefansson, I., & Tatomir, A. (2018b). Call for participation: Verification benchmarks for single-phase flow in three-dimensional fractured porous media. arXiv:1809.06926. Retrieved September 01, 2018, from https://ui.adsabs.harvard.edu/abs/2018arXiv180906926B

Berre, I., Doster, F., & Keilegavlen, E. (2019). Flow in Fractured Porous Media: A Review of Conceptual Models and Discretization Approaches. *Transport in Porous Media, 130*(1), 215-236. https://doi.org/10.1007/s11242-018-1171-6

Berre, I., Stefansson, I., & Keilegavlen, E. (2020). Fault slip in hydraulic stimulation of geothermal reservoirs: governing mechanisms and process-structure interaction. arXiv:2008.11190. Retrieved August 01, 2020, from https://ui.adsabs.harvard.edu/abs/2020arXiv200811190B

Berryman, J. G., & Wang, H. F. (1995). The elastic coefficients of double-porosity models for fluid transport in jointed rock. *Journal of Geophysical Research: Solid Earth, 100*(B12), 24611-24627. https://doi.org/10.1029/95jb02161

Biot, M. A. (1941). General Theory of Three-Dimensional Consolidation. *Journal of Applied Physics, 12*(2), 155-164. https://doi.org/10.1063/1.1712886

Biot, M. A., & Willis, D. (1957). The Elastic Coeffients of the Theory of Consolidation. *J. appl. Mech, 24*, 594-601.

Blanco, M. L., Rutqvist, J., & Birkholzer, J. T. (2014). *Long-Term Analysis of Thermal-Hydraulic-Mechanical Processes in a Generic Salt Repository for High-Level Nuclear Waste* 48th U.S. Rock Mechanics/Geomechanics Symposium, Minneapolis, Minnesota.

Blanton, T. L. (1982). *An Experimental Study of Interaction Between Hydraulically Induced and Pre-Existing Fractures* SPE Unconventional Gas Recovery Symposium, Pittsburgh, Pennsylvania. https://doi.org/10.2118/10847-MS

Bonnet, E., Bour, O., Odling, N. E., Davy, P., Main, I., Cowie, P., & Berkowitz, B. (2001). Scaling of fracture systems in geological media. *Reviews of Geophysics, 39*(3), 347-383. https://doi.org/10.1029/1999rg000074

Botti, M., Di Pietro, D. A., Le Maître, O., & Sochala, P. (2020). Numerical approximation of poroelasticity with random coefficients using Polynomial Chaos and Hybrid High-Order methods. *Computer Methods in Applied Mechanics and Engineering, 361*, 112736. https://doi.org/10.1016/j.cma.2019.112736

Bouffier, C. (2015). *Stress measurements by overcoring at the Grimsel site. Results from the campaign of August-September 2015. Study Report*. http://hdl.handle.net/20.500.11850/256660

Boutin, C., & Royer, P. (2015). On models of double porosity poroelastic media. *Geophysical Journal International, 203*(3), 1694-1725. https://doi.org/10.1093/gji/ggv378

Brixel, B., Klepikova, M., Jalali, M. R., Lei, Q., Roques, C., Kriestch, H., & Loew, S. (2020). Tracking Fluid Flow in Shallow Crustal Fault Zones: 1. Insights From Single-Hole Permeability Estimates. *Journal of Geophysical Research: Solid Earth, 125*(4). https://doi.org/10.1029/2019jb018200

Brown, S. R. (1987). Fluid flow through rock joints: The effect of surface roughness. *Journal of Geophysical Research: Solid Earth, 92*(B2), 1337-1347. https://doi.org/10.1029/JB092iB02p01337

Bruckner, T., Bashmakov, I. A., Mulugetta, Y., Chum, H., de la Vega Navarro, A., Edmonds, J., Faaij, A., Fungtammasan, B., Garg, A., Hertwich, E., Honnery, D., Infield, D., Kainuma, M., Khennas, S., Kim, S., Nimir, H. B., Riahi, K., Strachan, N., Wiser, R., & Zhang, X. (2015). Energy Systems. In C. Intergovernmental Panel on Climate (Ed.), *Climate Change 2014: Mitigation of Climate Change: Working Group III Contribution to the IPCC Fifth Assessment Report* (pp. 511-598). Cambridge University Press. https://doi.org/10.1017/CBO9781107415416.013

Caine, J. S., Evans, J. P., & Forster, C. B. (1996). Fault zone architecture and permeability structure. *Geology, 24*(11), 1025-1028. https://doi.org/10.1130/0091-7613(1996)024<1025:FZAAPS>2.3.CO;2

Castelletto, N., Ferronato, M., Franceschini, A., Settgast, R. R., & White, J. (2018). *Fully-Implicit Solvers For Coupled Poromechanics Of Fractured Reservoirs*. https://doi.org/10.3997/2214-4609.201802132

Cladouhos, T. T., Petty, S., Swyer, M. W., Uddenberg, M. E., Grasso, K., & Nordin, Y. (2016). Results from Newberry Volcano EGS Demonstration, 2010–2014. *Geothermics, 63*, 44-61. https://doi.org/10.1016/j.geothermics.2015.08.009

Coussy, O. (2003). Problems of Poroelasticity. In *Poromechanics* (pp. 113-150). https://doi.org/10.1002/0470092718.ch5

Dambly, M. L. T., Nejati, M., Vogler, D., & Saar, M. O. (2019). On the direct measurement of shear moduli in transversely isotropic rocks using the uniaxial compression test. *International Journal of Rock Mechanics and Mining Sciences, 113*, 220-240. https://doi.org/10.1016/j.ijrmms.2018.10.025

de Pater, C. J., & Beugelsdijk, L. J. L. (2005). *Experiments and numerical simulation of hydraulic fracturing in naturally fractured rock* Alaska Rocks 2005, The 40th U.S. Symposium on Rock Mechanics (USRMS), Anchorage, Alaska.

Doetsch, J., Gischig, V., Krietsch, H., Villiger, L., Amann, F., Dutler, N., Jalali, R., Brixel, B., Klepikova, M., Roques, C., Giertzuch, P., Kittilä, A., & Hochreutener, R. (2018). Grimsel ISC Experiment Description. https://doi.org/10.3929/ethz-b-000310581

Esaki, A., Du, S., Jiang, Y., Wada, Y., & Mitani, Y. (1998). Relation between mechanical and hydraulic apertures during shear-flow coupling test. Proc., 10th Japan Symp. Rock Mech.,

Fabrie, P., & Gallouët, T. (2000). Modeling wells in porous media flows. *Mathematical Models and Methods in Applied Sciences, volume 10, numero 5*, 673-709. https://hal.archives-ouvertes.fr/hal-00003333

Faulkner, D. R., Jackson, C. A. L., Lunn, R. J., Schlische, R. W., Shipton, Z. K., Wibberley, C. A. J., & Withjack, M. O. (2010). A review of recent developments concerning the structure, mechanics and fluid flow properties of fault zones. *Journal of Structural Geology, 32*(11), 1557-1575. https://doi.org/10.1016/j.jsg.2010.06.009

Faulkner, D. R., Lewis, A. C., & Rutter, E. H. (2003). On the internal structure and mechanics of large strike-slip fault zones: field observations of the Carboneras fault in southeastern Spain. *Tectonophysics, 367*(3), 235-251. https://doi.org/10.1016/S0040-1951(03)00134-3

Finnie, I., Cooper, G. A., & Berlie, J. (1979). Fracture propagation in rock by transient cooling. *International Journal of Rock Mechanics and Mining Sciences & Geomechanics Abstracts, 16*(1), 11-21. https://doi.org/10.1016/0148-9062(79)90771-X

Gan, Q., & Elsworth, D. (2016). A continuum model for coupled stress and fluid flow in discrete fracture networks. *Geomechanics and Geophysics for Geo-Energy and Geo-Resources, 2*(1), 43-61. https://doi.org/10.1007/s40948-015-0020-0

Gao, Y., Pang, H., Jin, Y., & Chen, M. (2019). Evaluation of Shear Dilation Capability/Potential and Permeability Changes in Karamay Oil Sands under Water Injection. *Geofluids, 2019*, 7245081. https://doi.org/10.1155/2019/7245081

Garcia, J., Hartline, C., Walters, M., Wright, M., Rutqvist, J., Dobson, P. F., & Jeanne, P. (2016). The Northwest Geysers EGS Demonstration Project, California: Part 1: Characterization and reservoir response to injection. *Geothermics, 63*, 97-119. https://doi.org/10.1016/j.geothermics.2015.08.003

Garipov, T. T., Karimi-Fard, M., & Tchelepi, H. A. (2016). Discrete fracture model for coupled flow and geomechanics. *Computational Geosciences, 20*(1), 149-160. https://doi.org/10.1007/s10596-015-9554-z

Gebauer, S., Neunhäuserer, L., Kornhuber, R., Ochs, S., Hinkelmann, R., & Helmig, R. (2002). Equidimensional modelling of flow and transport processes in fractured porous systems I. In S. M. Hassanizadeh, R. J. Schotting, W. G. Gray, & G. F. Pinder (Eds.), *Developments in Water Science* (Vol. 47, pp. 335-342). Elsevier. https://doi.org/10.1016/S0167-5648(02)80080-6

Gérard, A., Genter, A., Kohl, T., Lutz, P., Rose, P., & Rummel, F. (2006). The deep EGS (Enhanced Geothermal System) project at Soultz-sous-Forêts (Alsace, France). *Geothermics, 35*(5), 473-483. https://doi.org/10.1016/j.geothermics.2006.12.001

Geuzaine, C., & Remacle, J.-F. (2009). Gmsh: A 3-D finite element mesh generator with built-in pre- and post-processing facilities. *International Journal for Numerical Methods in Engineering, 79*(11), 1309-1331. https://doi.org/10.1002/nme.2579

Ghassemi, A. (2012). A Review of Some Rock Mechanics Issues in Geothermal Reservoir Development. *Geotechnical and Geological Engineering, 30*(3), 647-664. https://doi.org/10.1007/s10706-012-9508-3

Gischig, V., Jalali, R., Amann, F., Krietsch, H., Klepikova, M., Esposito, S., Broccardo, M., Obermann, A., Mignan, A., Doetsch, J., & Madonna, C. (2016). *Impact of the ISC Experiment at the Grimsel Test Site - Assessment of Potential Seismic Hazard and Disturbances to Nearby Experiments and KWO Infrastructure*. http://hdl.handle.net/20.500.11850/189973

Gischig, V. S., Doetsch, J., Maurer, H., Krietsch, H., Amann, F., Evans, K. F., Nejati, M., Jalali, M., Valley, B., Obermann, A. C., Wiemer, S., & Giardini, D. (2018). On the link between stress field and small-scale hydraulic fracture growth in anisotropic rock derived from microseismicity. *Solid Earth, 9*(1), 39-61. https://doi.org/10.5194/se-9-39-2018

Goldstein, B., Hiriart, G., Bertani, R., Bromley, C., Gutiérrez-Negrín, L., Huenges, E., Muraoka, H., Ragnarsson, A., Tester, J., & Zui, V. (2011). Geothermal Energy. In *IPCC Special Report on Renewable Energy Sources and Climate Change Mitigation*. Cambridge University Press.

Grabowski, J. W., Vinsome, P. K., Lin, R. C., Behie, G. A., & Rubin, B. (1979). *A Fully Implicit General Purpose Finite-Difference Thermal Model For In Situ Combustion And Steam* SPE Annual Technical Conference and Exhibition, Las Vegas, Nevada. https://doi.org/10.2118/8396-MS

Guglielmi, Y., Cappa, F., Avouac, J. P., Henry, P., & Elsworth, D. (2015). INDUCED SEISMICITY. Seismicity triggered by fluid injection-induced aseismic slip. *Science, 348*(6240), 1224-1226. https://doi.org/10.1126/science.aab0476

Guglielmi, Y. G., Henry, P., Nussbaum, C., Dick, P., Gout, C., & Amann, F. (2015). *Underground Research Laboratories for Conducting Fault Activation Experiments In Shales* 49th U.S. Rock Mechanics/Geomechanics Symposium, San Francisco, California.

Gupta, H., & Roy, S. (2007). Chapter 5 - EXPLORATION TECHNIQUES. In H. Gupta & S. Roy (Eds.), *Geothermal Energy* (pp. 61-119). Elsevier. https://doi.org/10.1016/B978-044452875-9/50005-8

Hou, B., Diao, C., & Li, D. (2017). An experimental investigation of geomechanical properties of deep tight gas reservoirs. *Journal of Natural Gas Science and Engineering, 47*, 22-33. https://doi.org/10.1016/j.jngse.2017.09.004

Houwers, M. E., Heijnen, L. J., Becker, A., & Rijkers, R. (2015). A Workflow for the Estimation of Fault Zone Permeability for Geothermal Production A General Model Applied on the Roer Valley Graben in the Netherlands. World Geothermal Congress, Melbourne, Australia.

Hüeber, S. (2008). *Discretization techniques and efficient algorithms for contact problems* University of Stuttgart].

Hüeber, S., Stadler, G., & Wohlmuth, B. I. (2008). A Primal-Dual Active Set Algorithm for Three-Dimensional Contact Problems with Coulomb Friction. *SIAM Journal on Scientific Computing, 30*(2), 572-596. https://doi.org/10.1137/060671061

Jaeger, J. C. (2007). *Fundamentals of rock mechanics* (4th ed. ed.). Blackwell.

Jalali, R., Klepikova, M., Doetsch, J., Krietsch, H., Brixel, B., Dutler, N., Gischig, V., & Amann, F. (2018). A Multi-Scale Approach to Identify and Characterize Preferential Flow Paths in a Fractured Crystalline Rock.

Jones, R. R., Pearce, M. A., Jacquemyn, C., & Watson, F. E. (2016). Robust best-fit planes from geospatial data. *Geosphere, 12*(1), 196-202. https://doi.org/10.1130/ges01247.1

Kamali, A., & Pournik, M. (2015). *Rough Surface Closure – A Closer Look at Fracture Closure and Conductivity Decline* ISRM Regional Symposium - EUROCK 2015, Salzburg, Austria.

Karimi-Fard, M., Durlofsky, L. J., & Aziz, K. (2004). An Efficient Discrete-Fracture Model Applicable for General-Purpose Reservoir Simulators. *SPE Journal, 9*(02), 227-236. https://doi.org/10.2118/88812-PA

Keilegavlen, E., Berge, R., Fumagalli, A., Starnoni, M., Stefansson, I., Varela, J., & Berre, I. (2020, 2020/10/14). PorePy: an open-source software for simulation of multiphysics processes in fractured porous media. *Computational Geosciences*. https://doi.org/10.1007/s10596-020-10002-5

Keilegavlen, E., & Nordbotten, J. M. (2017). Finite volume methods for elasticity with weak symmetry. *International Journal for Numerical Methods in Engineering, 112*(8), 939-962. https://doi.org/10.1002/nme.5538

Keusen, H. R., Ganguin, J., Schuler, P., & Buletti, M. (1989). *Technical Report 87-14 E*.

Koh, J., Roshan, H., & Rahman, S. S. (2011). A numerical study on the long term thermo-poroelastic effects of cold water injection into naturally fractured geothermal reservoirs. *Computers and Geotechnics, 38*(5), 669-682. https://doi.org/10.1016/j.compgeo.2011.03.007

Kranz, R. L. (1983). Microcracks in rocks: A review. *Tectonophysics, 100*(1), 449-480. https://doi.org/10.1016/0040-1951(83)90198-1

Krietsch, H., Doetsch, J., Dutler, N., Jalali, M., Gischig, V., Loew, S., & Amann, F. (2018a). Comprehensive geological dataset describing a crystalline rock mass for hydraulic stimulation experiments. *Sci Data, 5*, 180269. https://doi.org/10.1038/sdata.2018.269

Krietsch, H., Gischig, V., Doetsch, J., Jalali, R., & Amann, F. (2019). *Hydro mechanical data set from the six Grimsel ISC hydraulic shearing experiments* ETH Zurich. https://doi.org/10.3929/ethz-b-000328266

Krietsch, H., Gischig, V., Evans, K., Doetsch, J., Dutler, N. O., Valley, B., & Amann, F. (2018b). Stress Measurements for an In Situ Stimulation Experiment in Crystalline Rock: Integration of Induced Seismicity, Stress Relief and Hydraulic Methods. *Rock Mechanics and Rock Engineering, 52*(2), 517-542. https://doi.org/10.1007/s00603-018-1597-8

Krietsch, H., Gischig, V. S., Doetsch, J., Evans, K. F., Villiger, L., Jalali, M., Valley, B., Loew, S., & Amann, F. (2020). Hydro-mechanical processes and their influence on the stimulation effected volume: Observations from a decameter-scale hydraulic stimulation project. https://doi.org/10.5194/se-2019-204

Lall, U., Johnson, T., Colohan, P., Aghakouchak, A., Brown, C., McCabe, G. J., Pulwarty, R. S., & Sankarasubramanian, A. (2018). Water. In *Impacts, Risks, and Adaptation in the United States: Fourth National Climate Assessment* (Vol. II, pp. 145-173). U.S. Global Change Research Program. https://doi.org/10.7930/nca4.2018.Ch3

Lamont, N., & Jessen, F. W. (1963). The Effects of Existing Fractures in Rocks on the Extension of Hydraulic Fractures. *Journal of Petroleum Technology, 15*(02), 203-209. https://doi.org/10.2118/419-PA

Lavrov, A. (2017). 3 - Coupling in hydraulic fracturing simulation. In A. K. Shojaei & J. Shao (Eds.), *Porous Rock Fracture Mechanics* (pp. 47-62). Woodhead Publishing. https://doi.org/10.1016/B978-0-08-100781-5.00003-8

Lee, H. S., & Cho, T. F. (2002). Hydraulic Characteristics of Rough Fractures in Linear Flow under Normal and Shear Load. *Rock Mechanics and Rock Engineering, 35*(4), 299-318. https://doi.org/10.1007/s00603-002-0028-y

Lei, Q., Latham, J.-P., & Tsang, C.-F. (2017). The use of discrete fracture networks for modelling coupled geomechanical and hydrological behaviour of fractured rocks. *Computers and Geotechnics, 85*, 151-176. https://doi.org/10.1016/j.compgeo.2016.12.024

Lu, S.-M. (2018). A global review of enhanced geothermal system (EGS). *Renewable and Sustainable Energy Reviews, 81*, 2902-2921. https://doi.org/10.1016/j.rser.2017.06.097

Lutz, S., Hickman, S., Davatzes, N., Zemach, E., Drakos, P., & Tait, A. (2010). Rock mechanical testing and petrological analysis in support of well stimulation activities at the desert peak geothermal field, Nevada. *Proceedings, 37th Workshop on Geothermal Reservoir Engineering*, 1-3.

Mainprice, D. (2007). Seismic Anisotropy of the Deep Earth from a Mineral and Rock Physics Perspective. In *Treatese of Geophysics, vol.2* (pp. 437-491). Elsevier. https://doi.org/10.1016/b978-044452748-6.00045-6

Martin, V., Jaffré, J., & Roberts, J. E. (2005). Modeling Fractures and Barriers as Interfaces for Flow in Porous Media. *SIAM Journal on Scientific Computing, 26*(5), 1667-1691. https://doi.org/10.1137/S1064827503429363

McClure, M. W. (2012). *Modeling and characterization of hydraulic stimulation and induced seismicity in geothermal and shale gas reservoirs* http://purl.stanford.edu/dw028kp1342

McClure, M. W., & Horne, R. N. (2014). An investigation of stimulation mechanisms in Enhanced Geothermal Systems. *International Journal of Rock Mechanics and Mining Sciences, 72*, 242-260. https://doi.org/10.1016/j.ijrmms.2014.07.011

McLennan, J. D., & Roegiers, J. C. (1982). *How Instantaneous are Instantaneous Shut-In Pressures?* SPE Annual Technical Conference and Exhibition, New Orleans, Louisiana. https://doi.org/10.2118/11064-MS

Meinshausen, M., Meinshausen, N., Hare, W., Raper, S. C. B., Frieler, K., Knutti, R., Frame, D. J., & Allen, M. R. (2009). Greenhouse-gas emission targets for limiting global warming to 2 °C. *Nature, 458*(7242), 1158-1162. https://doi.org/10.1038/nature08017

Murphy, H. D., & Fehler, M. C. (1986). *Hydraulic fracturing of jointed formations*. ; Los Alamos National Lab., NM (USA). https://www.osti.gov/servlets/purl/6002163

Nejati, M. (2018). *On the anisotropy of mechanical properties in Grimsel granodiorite*. http://hdl.handle.net/20.500.11850/289969

Nejati, M., Dambly, M. L. T., & Saar, M. O. (2019). A methodology to determine the elastic properties of anisotropic rocks from a single uniaxial compression test. *Journal of Rock Mechanics and Geotechnical Engineering, 11*(6), 1166-1183. https://doi.org/10.1016/j.jrmge.2019.04.004

Neunhäuserer, L., Gebauer, S., Ochs, S., Hinkelmann, R., Kornhuber, R., & Helmig, R. (2002). Equidimensional modelling of flow and transport processes in fractured porous systems II. In S. M. Hassanizadeh, R. J. Schotting, W. G. Gray, & G. F. Pinder (Eds.), *Developments in Water Science* (Vol. 47, pp. 343-350). Elsevier. https://doi.org/10.1016/S0167-5648(02)80081-8

Nolte, C. G., Dolwick, P., Fann, N., Horowitz, L. W., Naik, V., Pinder, R. W., Spero, T. L., Winner, D. A., & Ziska, L. H. (2018). Air Quality. In *Impacts, Risks, and Adaptation in the United States: Fourth National Climate Assessment* (Vol. II, pp. 512-538). U.S. Global Change Research Program. https://doi.org/10.7930/NCA4.2018.CH13

Nordbotten, J. M. (2015). Finite Volume Methods. In B. Engquist (Ed.), *Encyclopedia of Applied and Computational Mathematics* (pp. 545-550). Springer Berlin Heidelberg. https://doi.org/10.1007/978-3-540-70529-1_433

Nordbotten, J. M., & Keilegavlen, E. (2020). An Introduction to Multi-Point Flux (MPFA) and Stress (MPSA) Finite Volume Methods for Thermo-Poroelasticity. https://arxiv.org/abs/2001.01990

Oda, M. (1986). An equivalent continuum model for coupled stress and fluid flow analysis in jointed rock masses. *Water Resources Research, 22*, 1845-1856. https://doi.org/10.1029/WR022i013p01845

Oron, A. P., & Berkowitz, B. (1998). Flow in rock fractures: The local cubic law assumption reexamined. *Water Resources Research, 34*(11), 2811-2825. https://doi.org/10.1029/98WR02285

Pahl, A., Heusermann, S., Bräuer, V., & Göggler, W. (1989). *Grimsel Test Site. Rock Stress Investigations* (NAGRA Technical Report, Issue.

Paterson, M. S., & Wong, T.-F. (2005). *Experimental Rock Deformation — The Brittle Field* (Second, Completely Revised and Updated Edition ed., Vol. 13). Berlin, Heidelberg: Springer Berlin Heidelberg. https://doi.org/10.1007/b137431

Pfister, E., & Nold, A. L. (1984). *The Grimsel rock laboratory In-situ experiments in crystalline rock*. IAEA. http://inis.iaea.org/search/search.aspx?orig_q=RN:15042256

Pine, R. J., & Batchelor, A. S. (1984). Downward migration of shearing in jointed rock during hydraulic injections. *International Journal of Rock Mechanics and Mining Sciences & Geomechanics Abstracts, 21*(5), 249-263. https://doi.org/10.1016/0148-9062(84)92681-0

Reichenberger, V., Jakobs, H., Bastian, P., & Helmig, R. (2006). A mixed-dimensional finite volume method for two-phase flow in fractured porous media. *Advances in Water Resources, 29*(7), 1020-1036. https://doi.org/10.1016/j.advwatres.2005.09.001

Ren, F., Ma, G., Fan, L., Wang, Y., & Zhu, H. (2017). Equivalent discrete fracture networks for modelling fluid flow in highly fractured rock mass. *Engineering Geology, 229*, 21-30. https://doi.org/10.1016/j.enggeo.2017.09.013

Ritchie, H. (2014). Energy. *Our World in Data*.

Rutqvist, J., & Oldenburg, C. M. (2008). *Analysis of Injection-Induced Micro-Earthquakes in a Geothermal Steam Reservoir, The Geysers Geothermal Field, California* The 42nd U.S. Rock Mechanics Symposium (USRMS), San Francisco, California.

Salimzadeh, S., Paluszny, A., Nick, H. M., & Zimmerman, R. W. (2018). A three-dimensional coupled thermo-hydro-mechanical model for deformable fractured geothermal systems. *Geothermics, 71*, 212-224. https://doi.org/10.1016/j.geothermics.2017.09.012

Sandve, T. H. (2013). Multiscale simulation of flow and heat transport in fractured geothermal reservoirs.

Schöberl, J. (1997). NETGEN An advancing front 2D/3D-mesh generator based on abstract rules. *Computing and Visualization in Science, 1*(1), 41-52. https://doi.org/10.1007/s007910050004

Selvadurai, P., Selvadurai, P. A., & Nejati, M. (2019). A multi-phasic approach for estimating the Biot coefficient for Grimsel granite. *Solid Earth, 10*, 2014. https://doi.org/10.5194/se-10-2001-2019

Shapiro, A. M., Evans, C. E., & Hayes, E. C. (2017). Porosity and pore size distribution in a sedimentary rock: Implications for the distribution of chlorinated solvents. *Journal of Contaminant Hydrology, 203*, 70-84. https://doi.org/10.1016/j.jconhyd.2017.06.006

Sibson, R. H. (1977). Fault rocks and fault mechanisms. *Journal of the Geological Society, 133*(3), 191-213. https://doi.org/10.1144/gsjgs.133.3.0191

Stefansson, I. (2016). *A Comparison of Two Numerical Models for Flow in Fractured Porous Media and the Impact of Fracture Intersection Cell Removal* The University of Bergen].

Stefansson, I., Berre, I., & Keilegavlen, E. (2020a). Finite volume discretisation of fracture deformation in thermo-poroelastic media. https://arxiv.org/abs/2002.05935

Stefansson, I., Berre, I., & Keilegavlen, E. (2020b). A fully coupled numerical model of thermo-hydro-mechanical processes and fracture contact mechanics in porous media. arXiv:2008.06289. Retrieved August 01, 2020, from https://ui.adsabs.harvard.edu/abs/2020arXiv200806289S

Teza, D., Baumgärtner, J., Lerch, C., Gandy, T., Hettkamp, T., Penzkofer, P., Schindler, M., & Wahl, G. (2011). Developing and circulating a fault system in the crystalline rock for geothermal power generation in Insheim, Germany.

Tiab, D., & Donaldson, E. C. (2012). Chapter 2 - Introduction to Petroleum Geology. In D. Tiab & E. C. Donaldson (Eds.), *Petrophysics (Third Edition)* (pp. 27-83). Gulf Professional Publishing. https://doi.org/10.1016/B978-0-12-383848-3.00002-5

Toro, E. F. (1999). Notions on Hyperbolic Partial Differential Equations. In *Riemann Solvers and Numerical Methods for Fluid Dynamics: A Practical Introduction* (pp. 41-85). Springer Berlin Heidelberg. https://doi.org/10.1007/978-3-662-03915-1_2

Urpi, L., Rinaldi, A. P., & Rutqvist, J. (2017). *Fault Reactivation Induced by Temperature and Pressure Changes in the Life of a Deep Geological repository* 51st U.S. Rock Mechanics/Geomechanics Symposium, San Francisco, California, USA.

Valley, B., & Evans, K. F. (2010). *Stress heterogeneity in the granite of the soultz EGS reservoir inferred from analysis of wellbore failure* World Geothermal Congress 2010, Bali, Indonesia, April 25-29, 2010, http://hdl.handle.net/20.500.11850/159329

Vallier, B., Magnenet, V., Schmittbuhl, J., & Fond, C. (2020). THM modeling of gravity anomalies related to deep hydrothermal circulation at Soultz-sous-Forêts (France). *Geothermal Energy, 8*(1), 13. https://doi.org/10.1186/s40517-020-00167-8 van den Ende, M. P. A., Chen, J., Ampuero, J. P., & Niemeijer, A. R. (2018). A comparison between rate-and-state friction and microphysical models, based on numerical simulations of fault slip. *Tectonophysics, 733*, 273-295. https://doi.org/10.1016/j.tecto.2017.11.040

Villiger, L., Gischig, V. S., Doetsch, J., Krietsch, H., Dutler, N. O., Jalali, M., Valley, B., Selvadurai, P. A., Mignan, A., Plenkers, K., Giardini, D., Amann, F., & Wiemer, S. (2020a). Influence of reservoir geology on seismic response during decameter-scale hydraulic stimulations in crystalline rock. *Solid Earth, 11*(2), 627-655. https://doi.org/10.5194/se-11-627-2020

Villiger, L., Zbinden, D., Rinaldi, A. P., Selvadurai, P. A., Krietsch, H., Gischig, V., Doetsch, J., Jalali, M., Amann, F., & Wiemer, S. (2020b, 4–8 May 2020). The influence of the heterogeneous asperity distribution on induced seismicity and permeability evolution during hydraulic fault zone stimulation. EGU General Assembly 2020, Online.

Wang, H. F. (2000). *Theory of Linear Poroelasticity with Applications to Geomechanics and Hydrogeology*. Princeton University Press. https://doi.org/10.2307/j.ctt1jktrr4

Wang, P., Jiang, Z., Ji, W., Zhang, C., Yuan, Y., Chen, L., & Yin, L. (2016). Heterogeneity of intergranular, intraparticle and organic pores in Longmaxi shale in Sichuan Basin, South China: Evidence from SEM digital images and fractal and multifractal geometries. *Marine and Petroleum Geology, 72*, 122-138. https://doi.org/10.1016/j.marpetgeo.2016.01.020

Wang, W., Bauer, S., Nagel, T., Shao, H., Kolditz, O., & Görke, U.-J. (2018). *Thermo-Hydro-Mechanical-Chemical Processes in Fractured Porous Media: Modelling and Benchmarking: From Benchmarking to Tutoring*. Cham: Springer International Publishing. https://doi.org/10.1007/978-3-319-68225-9

Wehrens, P., Baumberger, R., Berger, A., & Herwegh, M. (2017). How is strain localized in a meta-granitoid, mid-crustal basement section? Spatial distribution of deformation in the central Aar massif (Switzerland). *Journal of Structural Geology, 94*, 47-67. https://doi.org/10.1016/j.jsg.2016.11.004

Wenning, Q. C., Madonna, C., de Haller, A., & Burg, J.-P. (2018). Permeability and seismic velocity anisotropy across a ductile–brittle fault zone in crystalline rock. *Solid Earth, 9*(3), 683-698. https://doi.org/10.5194/se-9-683-2018

Wibberley, C. A. J., Yielding, G., & Di Toro, G. (2008). Recent advances in the understanding of fault zone internal structure: a review. *Geological Society, London, Special Publications, 299*(1), 5-33. https://doi.org/10.1144/sp299.2

Wintsch, R. P., Christoffersen, R., & Kronenberg, A. K. (1995). Fluid-rock reaction weakening of fault zones. *Journal of Geophysical Research: Solid Earth, 100*(B7), 13021-13032. https://doi.org/10.1029/94jb02622

Witherspoon, P. A., Wang, J. S. Y., Iwai, K., & Gale, J. E. (1980). Validity of Cubic Law for fluid flow in a deformable rock fracture. *Water Resources Research, 16*(6), 1016-1024. https://doi.org/10.1029/WR016i006p01016

Wohlmuth, B. (2011). Variationally consistent discretization schemes and numerical algorithms for contact problems. *Acta Numerica, 20*, 569-734. https://doi.org/10.1017/S0962492911000079

Zhang, N., He, M., Zhang, B., Qiao, F., Sheng, H., & Hu, Q. (2016). Pore structure characteristics and permeability of deep sedimentary rocks determined by mercury intrusion porosimetry. *Journal of Earth Science, 27*(4), 670-676. https://doi.org/10.1007/s12583-016-0662-z

Zhou, H., Abdelaziz, A., & Grasselli, G. (2018). *Rock Dilation and Its Effect on Fracture Transmissivity* SPE/AAPG/SEG Unconventional Resources Technology Conference, Houston, Texas, USA. https://doi.org/10.15530/URTEC-2018-2903018

Zhou, J., & Xue, C. (2011). *Experimental Investigation of Fracture Interaction between Natural Fractures and Hydraulic Fracture in Naturally Fractured Reservoirs* SPE EUROPEC/EAGE Annual Conference and Exhibition, Vienna, Austria. https://doi.org/10.2118/142890-MS

Ziegler, M., Loew, S., & Moore, J. R. (2013). Distribution and inferred age of exfoliation joints in the Aar Granite of the central Swiss Alps and relationship to Quaternary landscape evolution. *Geomorphology, 201*, 344-362. https://doi.org/10.1016/j.geomorph.2013.07.010

Zimmerman, R. W., Chen, D.-W., & Cook, N. G. W. (1992). The effect of contact area on the permeability of fractures. *Journal of Hydrology, 139*(1), 79-96. https://doi.org/10.1016/0022-1694(92)90196-3

Zimmerman, R. W., Kumar, S., & Bodvarsson, G. S. (1991). Lubrication theory analysis of the permeability of rough-walled fractures. *International Journal of Rock Mechanics and Mining Sciences & Geomechanics Abstracts, 28*(4), 325-331. https://doi.org/10.1016/0148-9062(91)90597-F

Zoback, M. D., Rummel, F., Jung, R., & Raleigh, C. B. (1977). Laboratory hydraulic fracturing experiments in intact and pre-fractured rock. *International Journal of Rock Mechanics and Mining Sciences & Geomechanics Abstracts, 14*(2), 49-58. https://doi.org/10.1016/0148-9062(77)90196-6